Predicting Noise-Power-Distance Tables for the REBEL-C Blended Wing Body Aircraft

N.M. van Dam

Delft University of Technology

TU Delft

Master thesis

Predicting Noise-Power-Distance Tables for the REBEL-C Blended Wing Body Aircraft

Master thesis

by

N.M. van Dam

Monday 4th May, 2026

Daily supervisor:	prof.dr.ir. M. Snellen
Supervisor:	ir. A.S. Jayanthi
Supervisor:	ir. N. van Oosten
Chairman:	dr.ir. R. Vos
Independent member:	dr. A. Amiri-Simkooei
Project Duration:	May, 2025 - May, 2026
Faculty:	Faculty of Aerospace Engineering, Delft

Cover: render of REBEL-C blended wing body aircraft, taken from `https://www.dlr.de/en/at/research-transfer/projects/artem` on 28-04-2026

TU Delft

Preface

This thesis concludes a year of research. Although my background on aircraft noise was small to start with, I am happy I got the opportunity to work on this project and broaden my horizon. During this year I not only learned a lot about noise modeling but also on how to do research itself, something I feel like was missing a bit in the many years of courses during my study. I was pleasantly surprised by how much I enjoyed doing this research.

I would like to express my thanks to my supervisors both at TU Delft and Anotec Engineering. To my daily supervisor Mirjam Snellen for her guidance and encouragement. To Furkat Yunus and Anandini Jayanthi, who offered advice along the way whenever I was stuck. I have enjoyed our meetings and always felt inspired afterwards. A thank you to Daamanjyot Barara for this feedback on my report and a thank you to all current and former faculty members that took their time to answer my questions.

I would like to thank Nico van Oosten from Anotec Engineering on his supervision and practical advice. A special thank you to Luis from Anotec Engineering, who programmed and updated the new noise modules in SOPRANO so I could work with the latest version.

Finally, I would like to thank my family and friends for their support during this year. Having you around me definitely helped me this last year.

Nienke van Dam
Delft, Monday 4th May, 2026

Summary

This thesis aims to predict noise-power-distance (NPD) tables for the REBEL-C, a blended wing body (BWB) aircraft designed during the ARTEM project using the semi-empirical noise modeling program SOPRANO from Anotec. A comparison is made with its reference aircraft, the Airbus A320. SOPRANO has been evaluated for a case study of two flyovers for the A320. Comparison with a suite of semi-empirical noise models implemented in-house at TU Delft showed similar results. The engine performance of the CFM56-5B4 turbofan engine was obtained using the Gasturbine Simulation Program.

Engine placement on top of the fuselage causes engine noise shielding for observers below the aircraft. Three noise sources and their location were identified: the fan inlet, fan exit and the jet exit, with the latter representing the jet and combustor noise source. All were modeled as a point source. The noise shielding method used was developed in an earlier project. It is based on Kirchhoff's theory of diffraction and uses the Modified Theory of Physical Optics. Both edge-diffraction and diffraction due to creep was analyzed. The inclusion of creeping rays, representing waves following curved surfaces, in the analysis had limited effect on the attenuation due to shielding. It was found that the source location matters greatly for the shielding attenuation, with the more aft jet source being shielded less even at the front of the aircraft. It is hypothesized that this is due to stronger edge-diffraction around the fuselage trailing edge. The number of observers projected on a hemisphere encompassing the aircraft greatly influenced the results, especially at high frequencies. Due to the computational power required for the detailed shielding analysis, this was done separately from SOPRANO. Tables including ΔSPL showing the noise reduction per noise source were generated for all polar and azimuthal angles and implemented into SOPRANO.

Next the methodology to obtain NPD tables was described. Noise for flyovers at 1000 ft altitude, 160 kt and various power settings was computed with SOPRANO for an Airbus A320-214, Boeing 777-200LR and Airbus A330-301. The results were extrapolated to the other slant distances and processed into NPD tables. A good agreement was found between the computations and the NPD tables from the Aircraft Noise and Performance (ANP) database. The average root mean square error for $L_{A_{max}}$ for the A320, Boeing 777 and A330 were 0.9 dBA, 2.8 dBA and 2.2 dBA, respectively.

Due to limited data on the REBEL-C, the flight path of the BWB was assumed to be similar to that of the A320, although the REBEL-C is expected to have a higher climb angle and larger angle of attack. The maximum takeoff weight and maximum landing weight of the BWB were estimated based on preliminary design principles and used to obtain the flight profile assuming an equal thrust-to-weight (T/W) ratio. Thrust settings were chosen from the flight profile for both departure and approach for the NPD tables. Since the high bypass ratio engines for the REBEL-C have not yet been designed, the same turbofan engine as for the A320 was used.

The results show overall lower noise for the REBEL-C. Engine shielding lowers $L_{A_{max}}$ by up to 12.4 dBA for maximum thrust of the CFM56-5B4 engine during departure at 1000 ft distance. Using equal T/W ratios this number increases to 18.7 dBA for 1000 ft. For power settings that can be expected to be used during departure, the slat noise starts to dominate over the shielded engine noise. Airframe noise is dominant during approach. The noise reduction compared to the A320 smaller for arrival although still present. The reduction in $L_{A_{max}}$ is 3.8 dBA at 1000 ft. A sensitivity study was done on airframe components that had to be estimated. The deviations were limited to within 1.0 dBA for $L_{A_{max}}$ and 1.3 dBA for SEL.

Low noise technology implementation has not been included in this study, however it is recommended for both the engine and the airframe. Furthermore, an airframe noise model fitted for BWB aircraft and using a turbofan designed for the lighter REBEL-C would decrease uncertainties. Before the NPD tables can be used, the lateral installation correction used in ECAC Doc. 29 is to be calculated.

Nomenclature

Abbreviations

Abbreviation	Definition
ANP	Aircraft noise and performance
ANS	Aircraft Noise Studio
AoA	Angle of attack
BPF	Blade passage frequency
BPR	Bypass ratio
BWB	Blended wing body
CDA	Continuous descent approach
CFD	Computational fluid dynamics
GSP	Gasturbine Simulation Program
HP	High pressure
ICAO	International Civil Aviation Organization
ISA	International standard atmosphere
KTD	Kirchhoff's theory of diffraction
L/D	Lift-to-drag
LP	Low pressure compressor
MLW	Maximum landing weight
MTOW	Maximum takeoff weight
MTPO	Modified theory of physical optics
NPD	Noise-power-distance
NSP	Noise shielding program
TAW	Tube-and-wing
TOW	Takeoff weight
T/W	Thrust-to-weight

Symbols

Symbol	Definition	Unit
A	Cross-sectional area	[m^2]
A_w	Wing area	[m^2]
b_v	Vertical stabilizer span	[m]
b_w	Wing span	[m]
c	Speed of sound	[m/s]
d	Diameter	[m]
D	Directivity	[-]
EPNL	Effective perceived noise level	[EPNdB]
f	Frequency	[Hz]
f_b, f_n	1/3 octave band center frequency	[Hz]
F_N	Thrust per engine	[N]
F_N/δ	Net-corrected thrust per engine	[N]
h, z, H	Height	[m]
k	Wavenumber	[-]
L_A, OASPL	Overall A-Weighted Sound Pressure Level	[dBA]
L_{PN}, PNL	Perceived noise level	[PNdB]
$\dot{m}$	Mass flow	[kg/s]

Symbol	Definition	Unit
M	Mach number, Weight fraction	[-]
M_c	Convective Mach number	[-]
N	Fresnel number	[-]
N_B	Number of blades	[-]
N_V	Number of vanes	[-]
N_w	Number of wheels	[-]
$N1$	RPM fan	[-]
$N1\%$	Percentage of maximum RPM fan	[%]
OSPL	Overall Sound Pressure Level	[dB]
p, $\langle p \rangle$	Acoustic pressure	[Pa]
p_d	Boundary diffracted pressure field	[Pa]
p_i	Incident pressure field	[Pa]
p_s	Scattered pressure field	[Pa]
P	Static pressure	[Pa]
PNLT	Tone corrected perceived noise level	[TPNdB]
P_t	Total pressure	[Pa]
r	Distance between observer and noise source or aperture	[m]
r, a_c	Radius	[m]
R	Distance between observer and noise source	[m]
RPM	Rotations per Minute	[-]
s	Minimum required arc length	[m]
SEL	Sound exposure level	[dBA]
SPL	Sound pressure level	[dB]
S_{ref}	Reference surface area	[m^2]
S_{wet}	Wetted surface area	[m^2]
St	Strouhal number	[-]
t_{curve}	Arc length	[m]
T	Static temperature	[K]
T_{period}	Period	[s]
T_t	Total temperature	[K]
V	Velocity	[m/s]
W	Weight	[N]
α,$\bar{\alpha}$	(Average) absorption coefficient	[dB/m]
Γ	Segment length along contour aperture	[m]
η	Efficiency	[-]
θ	Polar directivity angle	[°]
Θ	Flap deflection angle	[°]
λ	Wavelength	[m]
Π	Acoustic power	[m]
ρ	Density	[kg/m^3]
ϱ	Distance between source and aperture	[m]
σ	Width of Fock's region	[m]
ϕ	Azimuthal angle	[°]

Indices

Symbol	Definition
0, a, amb	freestream condition
2	fan inlet
21	fan outlet
13	bypass inlet
19	bypass jet
3	combustor inlet

Symbol	Definition
4	combustor outlet
5	turbine outlet
9	core jet
des	design point
e	effective
f	fuel
ISA	International Standard Atmospheric condition
ref	reference
t, tip	blade tip
$turb$	turbine

Constants

Symbol	Value	Unit
c_{ISA}	340.3	[m/s]
g_0	9.80665	[m/s^2]
I_{ref}	$10 \cdot 10^{-12}$	[W/m^2]
p_{ref}	$2.0 \cdot 10^{-5}$	[Pa]
P_{ISA}	101325	[Pa]
R	287.05	[J/(kg·K)]
T_{ISA}	288.15	[K]
γ	1.4	[-]
λ_T	-0.0065	[K/m]
Π_{ref}	$1.0 \cdot 10^{-12}$	[W]
ρ_{ISA}	1.225	[kg/m^3]

Contents

1. Introduction

With the world getting more connected each day and airports expanding in urban areas, more people get exposed to aircraft noise. Research on people living in these urban areas within Europe with continuous exposure to noise has shown negative effects on not only a psychological level, but rather for physiological, metabolic and immune systems as well [1, 2]. Therefore, the European Environmental Agency has set a 2030 Zero Pollution Noise Target [3], aiming to reduce the number of people chronically disturbed by all transport noise [4]. To understand which areas are most prone to aircraft noise and the noise levels that are reached there, noise models are used for legislation. Best practice models such as ECAC Doc. 29 [5] describe how noise can be modeled over a period of time using noise-power-distance (NPD) tables. These NPD tables describe the noise metrics of an aircraft flying over for multiple thrust settings and distances [6].

The International Civil Aviation Organization (ICAO) has proposed multiple methods to reduce long-term noise exposure, one of which is noise reduction at the source [7]. Developments in more efficient (ultra-)high bypass ratio (BPR) turbofan engines have reduced aircraft noise over the years [8], however noise reduction on conventional tube-and-wing (TAW) aircraft configurations is reaching its limits [9]. Therefore, radically different aircraft designs are required to reduce noise exposure further. One such design is the blended wing body (BWB) aircraft. It has been designed for improved aerodynamic performance and has its engines mounted on top of the fuselage [10]. This makes the airframe act as an engine noise barrier for observers on the ground. The REBEL-C is an example of a BWB aircraft, designed during the ARTEM project at the University of Roma Tre by Centracchio et al. [11].

Noise studies on BWB aircraft have been limited to predictions for noise certification purposes [12, 13]. Noise analysis of conceptual aircraft give insight to the expected noise levels. Although certification predictions show noise reductions for BWB aircraft [14] compared to TAW aircraft, these predictions cannot be used in best practice models.

1.1. Research objective

In order to predict the noise contribution of novel aircraft designs to the total noise exposure, NPD tables have to be generated. This has not been done for BWB aircraft yet. The noise metrics in these tables are normally obtained through measurements [15], however this is not an option for a conceptual design such as the REBEL-C. Therefore, the main objective of this research is to develop a methodology to predict the NPD tables for the REBEL-C BWB aircraft and assess its characteristics.

The main research question is defined as:

What are the noise-power-distance tables for the REBEL-C?

To analyze this structurally, four subquestions have been formulated:

1. How can the NPD tables of a conceptually designed aircraft be generated?
2. What is the effect of the engine placement on the noise produced by the REBEL-C?
3. What is the airframe noise produced by the REBEL-C?
4. How do the NPD tables for the REBEL-C compare to its reference aircraft?

In order to determine the NPD tables, the predictions are done through noise modeling. Engine noise shielding is evaluated using a detailed shielding model based on Kirchhoff's theory of diffraction. The results are implemented in the semi-empirical noise modeling program SOPRANO. Since the flight profile of the REBEL-C is unknown, the flight profile of a reference aircraft is used where the thrust settings are determined by assuming an equal thrust-to-weight ratio (T/W). The reference aircraft used in this study is the Airbus A320-214 with CFM56-5B4 turbofan engines. The creation of an engine installation correction was deemed outside of the scope of this research.

1.2. Report outline

This reported is structured as follows: first, a literature study on blended wing body aircraft in general and the REBEL-C in particular is done in chapter 2. This chapter includes details on aircraft noise modeling and the use of noise-power-distance tables as well. Afterwards, the semi-empirical noise prediction methods that have been used are described in detail in chapter 3. Furthermore, SOPRANO, the model that has been used, is verified in this chapter. chapter 4 describes the method that has been used to analyze the noise attenuation due to the engine placement. The framework for the noise-power-distance tables is set up in chapter 5 and verified for three conventional transport aircraft. The power inputs for the NPD tables are obtained using the flight profile given in chapter 6. These are then used to obtain the results shown and discussed in chapter 7. Finally, in chapter 8 the conclusions are drawn and recommendations are given.

2. Literature Study

The concept of BWB aircraft is introduced in this chapter before describing the REBEL-C, the aircraft that is analyzed. Furthermore, an overview of how aircraft noise is described and ways to model it are given. Earlier research on BWB aircraft noise is shown as well. Finally, the use of NPD tables is described.

2.1. Blended Wing Body Aircraft

A BWB aircraft represents a unique geometry which blends the wings into the fuselage. While the designs have already been proposed in the 1980s, design challenges held the production back [16]. New demands for more sustainable aircraft have brought the design back to the forefront.

2.1.1. Characteristics

The main characteristic of a BWB aircraft is that the whole aircraft body acts as a lifting surface, not just the wings [10]. This is why the fuselage is wider than conventional TAW aircraft. Although many variations of blended wing body aircraft have been designed, a few key characteristics prevail. Many BWB aircraft have no horizontal tail surface and sometimes no vertical tail either. They are operated like a flying wing [17], however they differ from flying wings like the Flying V [18], which have no fuselage or tail. The engines are often found on top of the fuselage [10] and can vary in type of propulsor. An example of a BWB called N3-X from NASA is shown in Figure 2.1 [19]. The 300 passenger aircraft clearly shows the blending of fuselage and wings [20] with high-lift devices (HLD) integration to reduce noise [12]. Turboelectric propulsors with a high BPR are placed on top of the fuselage. Since no vertical tail or winglets are present, yaw control is achieved through the propulsors [21]. NASA has showed a reduction of 70% in fuel consumption [22].

Figure 2.1: N3-X design, obtained from NASA [19]

One of the main benefits of BWB designs is found in its aerodynamic performance. Torenbeek states that for TAW aircraft the wing generates almost all lift, while producing just 3-5% of the drag compared to the lift. The fuselage and tail create similar skin friction drag, however the lift contribution is very limited [17]. While the fuselage of a BWB contributes to the lifting capabilities, it has a lower lift coefficient than the wings to optimize for an elliptic lift distribution according to Liebeck [23]. An example of this lift distribution is shown in Figure 2.2. Increasing the lifting surface while maintaining the drag can increase the lift-to-drag (L/D) ratio up to 22% compared to a TAW aircraft [16]. The larger lifting area reduces the wing loading, which is defined as the aircraft weight over the surface area. The takeoff and landing speed is reduced due to this and the climb angle increased. A downside to this design is that

the maximum lift coefficient is reduced when HLD's are deployed since trimming from the horizontal tail is not possible. This is however partly mitigated by the lower wing loading. On the other hand, the lower wing loading requires a higher angle of attack (AoA) to achieve maximum lift. Lower speeds and a large wing surface increase the gust loads and stall sensitivity [24].

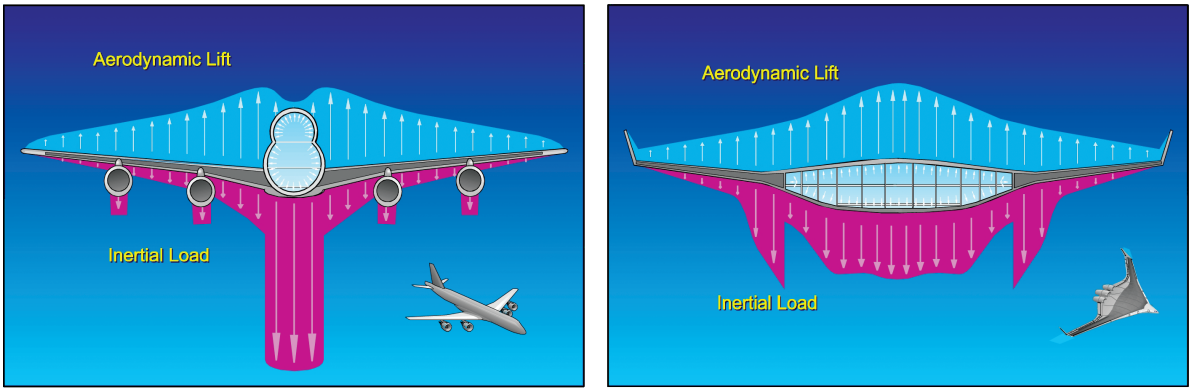

Figure 2.2: Spanwise loading distribution (blue) and inertial load distribution (pink) for a traditional TAW configuration (left) and a BWB aircraft (right), obtained from [23]

From a structural standpoint the unique fuselage design gives some challenges. The non-circulatory shape still needs to withstand pressurization, torque and bending. This requirement often increases the structural weight of the fuselage than its TAW counterpart [17]. A benefit of the fuselage lifting design is however that extreme wing bending is decreased due to lower wing loading [10].

One of the main challenges preventing the BWB to be used is in stability and control [16]. Tailless aircraft have to be stabilized by either combining sweep and wing twist such that the wing tip regions produce negative lift like the horizontal tail on a TAW aircraft, or by using active control systems. Controllability can be achieved through ailerons on the trailing edges [25]. Rudders on vertical stabilizers or wingtips enable directional stability, however the small moment arms make it hard to control [26].

Different types of propulsion are being tested on BWB aircraft, from (ultra-high BPR) turbofans to hydrogen fueled propulsors and fully electric versions. An important aspect is the integration, where a pylon can be used to position the engine above the surface or by integrating the engines into the surface. The latter can use boundary layer ingestion or divert the boundary layer. Integration of the engines lowers inlet drag and weight [23], however the risk of pressurization issues may cause lower thrust at high AoA when flow separation on the upper surface may occur [27]. The total weight of BWB aircraft is often lower than TAW aircraft, reducing its fuel consumption. Reductions of up to 27% per seat-mile have been proposed [23].

Newer BWB show the engines further forward, some distance before the trailing edge. This is done with noise reduction in mind, since the aircraft body will now shield a part of the noise generated by the engines [28]. Furthermore, the high climb angle and reduced takeoff thrust reduces the noise generated by BWB aircraft even more [29]. A lower approach velocity together with a steeper glide slope can help reduce the total noise produced during arrival [14].

2.1.2. REBEL-C

The conceptual BWB design used in this research is the regional aircraft REBEL-C developed in the ARTEM project at Roma Tre Univesity by Centracchio, Rossetti and Iemma [11]. The REBEL-C is the version of the REBEL that uses high BPR turbofan engines located on the top aft fuselage. The REBEL itself was designed as an electrically propelled aircraft [11]. In the same family is a larger turbofan powered aircraft called BOLT [30]. A render of the REBEL-C is shown in Figure 2.3 [31].

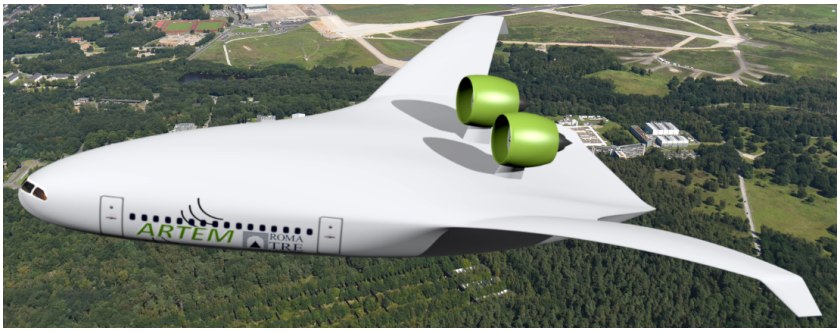

Figure 2.3: Render of the REBEL-C, obtained from the DLR ARTEM project website [31]

The wide fuselage is clearly shown, together with the two turbofan engines mounted on top. A characteristic of this design is the downwards pointing winglet. The REBEL-C is compared to the Airbus A320 during its design stage [11] and therefore a version of the A320, the A320-214, is used as a reference aircraft. A visual size comparison is given in Figure 2.4 [11].

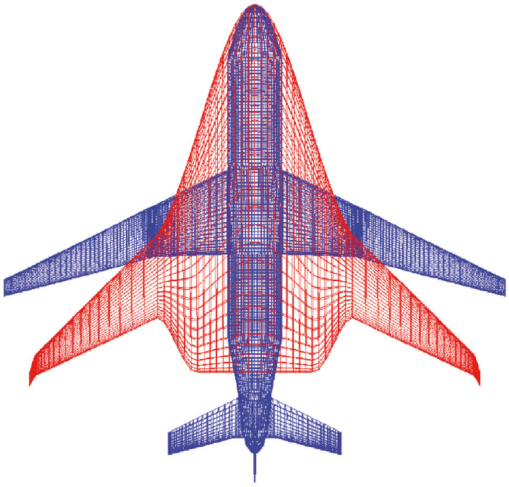

Figure 2.4: Size comparison of the REBEL-C in red and A320 in blue, obtained from [11]

The REBEL-C is clearly shorter than the A320 with a smaller span. The larger fuselage volume however makes up for the shorter cabin. It has been designed for a short range of just 900 nmi due to the electric nature of its family member REBEL [11]. Some design and performance parameters of both REBEL-C and A320 are given in Table 2.1 [11, 32–35]. The lower design range, passenger capacity and cruise speed make the REBEL-C much more of a regional aircraft than the larger A320. Although smaller in size, the wetted area of the BWB aircraft is 2.7 times larger and the L/D ratio is 17% higher.

Table 2.1: Design and performance parameters

Parameter	REBEL-C	A320-214
Design range [nmi]	900	3000
Number of passengers [-]	100	150-180
Cruise Mach number [-]	0.5	0.78
Cruise altitude [ft]	25,000	39,000
Surface area [m^2]	326.03	122.6
Span [m]	32.45	34.1
Length [m]	27.85	37.6
L/D ratio [-]	19.0	16.3

2.2. Aircraft Noise

Sound is a disturbance of air, where vibrations cause this matter to compress and expand. This causes small pressure changes. These pressure waves travel through a medium to a receiver or observer, which hears the sound. For aircraft, the sound waves that are generated are considered unwanted and are defined as noise. This noise can either be tonal, displaying sounds at certain frequencies, or broadband, like background noise from a busy street [36].

Aircraft noise consists of a combination of noise sources, distinguished between airframe and engine noise. Within these, the airframe noise consists of a combination of all the airframe components generating noise through turbulence, flow separation, flow interaction or other mechanisms. Each engine component has its own noise mechanism [37]. The sound intensity levels of the separate elements can be added to obtain the final noise level.

2.2.1. Noise modeling

There are multiple methods to determine aircraft noise. The first distinction is made between modeling and measuring. If no (scale-model) aircraft has been build, modeling is the only option. Bertsch et al. describe four types of models [38]:

- Fully numerical modeling using computational fluid dynamics (CFD) where both source and propagation are simulated simultaneously;
- CFD combined with acoustic analogy modeling where both source and propagation are simulated in separate steps;
- Fully and semi-analytical modeling where the flow and acoustic field are found using poles for a source and Green's function for the receiver sound. For a semi-analytical model this is combined with another approach;
- Empirical modeling using methods developed from acoustic experiments [38].

These types are shown in Figure 2.5. Although CFD based models are often accurate, they do require a large computational domain and highly detailed aircraft or airframe component design. Analytical models require low computational power, however they are not as flexible to input changes and are limited in accuracy. Semi-analytical models can be used for existing components and highly detailed designs, whereas fully-empirical models can only be used for existing aircraft. Semi-empirical models using empirical data and an analytical approach have a higher accuracy and flexibility while still requiring a relatively low computational domain [37]. It is the most common method used for novel aircraft designs where the full configuration is not available yet [39] as shown in Figure 2.5. This methodology will be used for the REBEL-C.

2.2.2. SOPRANO

SOPRANO is a noise modeling program developed by Anotec Engineering that has been used for this research. It is based on semi-empirical noise models. The workflow of SOPRANO is depicted in Figure 2.6. The Aircraft Noise Studio (ANS) is used as presolver and contains multiple different modules for each noise source component, each with their own method. To each source, flight effects (Δ components) such as a Doppler shift and delta's can be added. Delta's are additions or subtractions to a module due to for example installation effects, which can be defined per frequency, polar angle, azimuthal angle and for other parameters such as distance. Furthermore, propagation through the air, absorption, reflection and attenuation can be added. Flight effects and delta's can be incorporated for the system as a whole as well. The required airframe and engine input for each module can be entered in separate cases, enabling the user to run and compare multiple cases at a time. Some inputs can be parameterized to get data from multiple conditions (such as fan rotor speed) at once. The engine performance data is obtained separately using the Gasturbine Simulation Program (GSP). The flight path and observer location is defined in each case. When this is done, SOPRANO analyzes the cases and gives detailed results. Output options include sound pressure level results per component, frequency and point along the flight path, footprints and overall noise levels. This data can then be processed further.

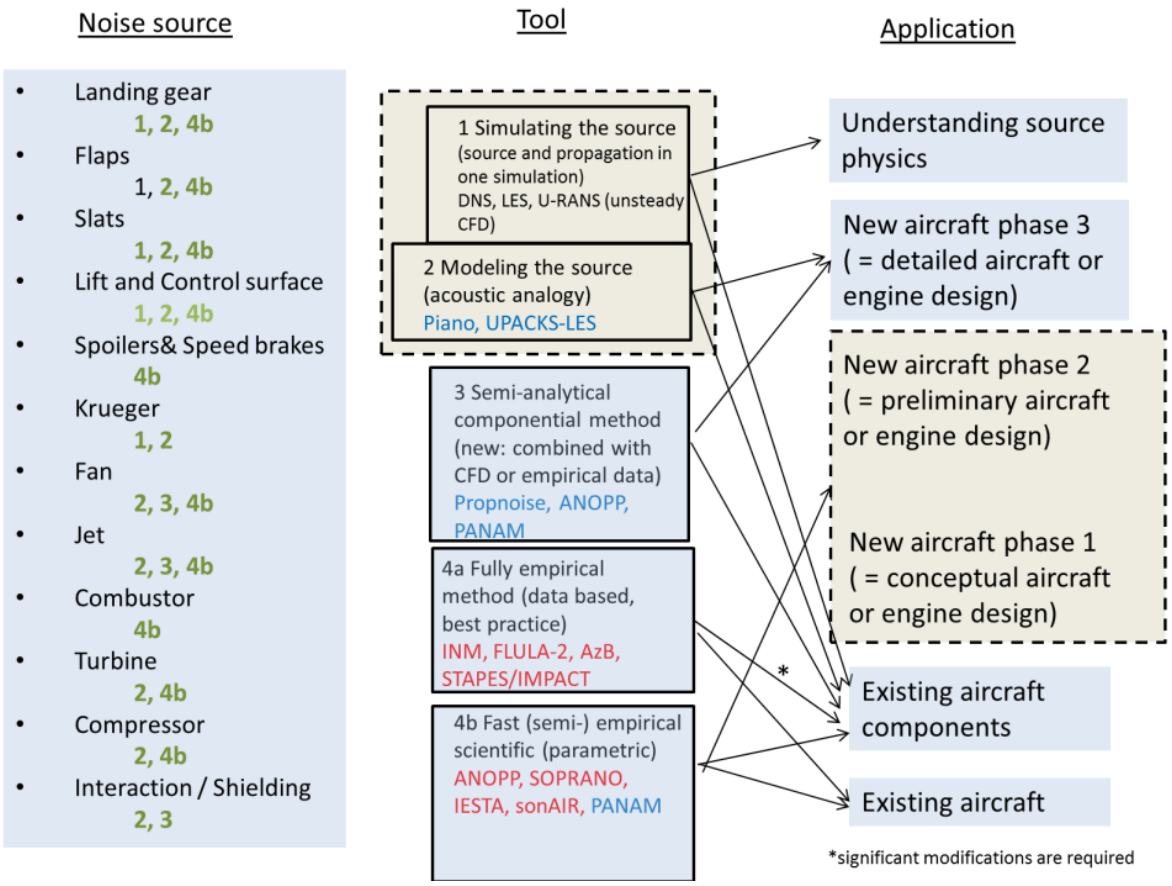

Figure 2.5: Noise modeling tools for different noise sources and their application, obtained from [38]

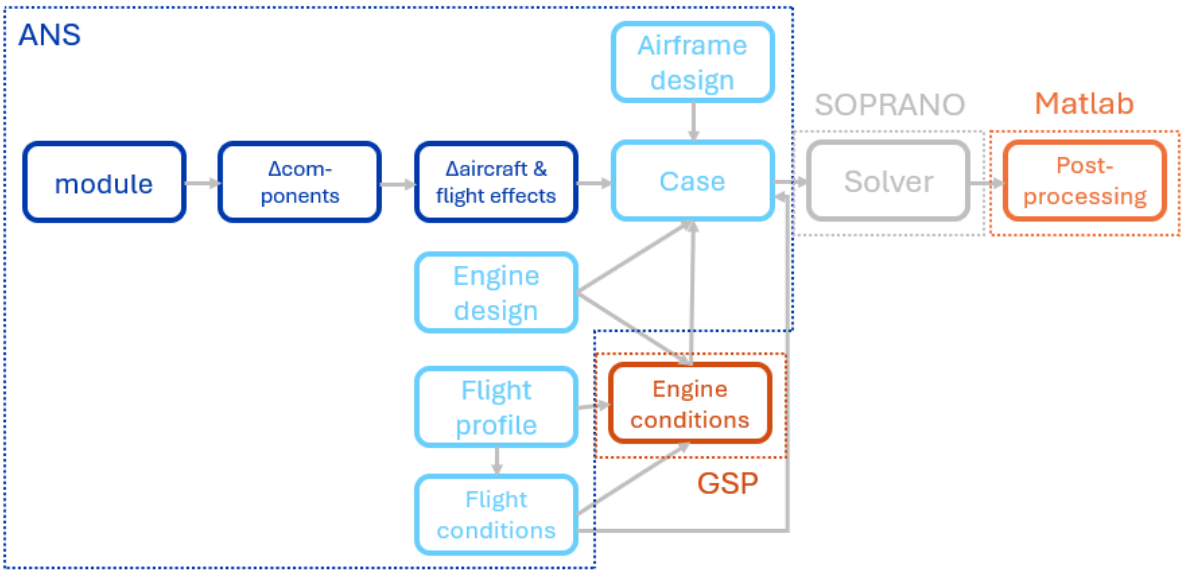

Figure 2.6: Flowchart depicting the workflow for SOPRANO

2.2.3. Single event noise metrics

An aircraft flying by is often referred to as an event. If only one aircraft movement is analyzed and its noise described, single event noise metrics are used [6]. For aircraft noise it is common that not all frequencies in the whole spectrum are analyzed, but rather set of bandwidths. The 1/3-octave frequency bands have a center, lower and upper frequency band for each bandwidth. Instead of repeatedly having to compute the center frequencies, a set of them is defined by the ICAO which regulates aircraft noise certification [40]. These are frequencies that most aircraft noise is generated in and the human ear can perceive [6]. The center frequencies are given in Table 2.2 [40].

Table 2.2: 1/3 octave center band frequencies used in aircraft noise analysis

Band number	Frequency [Hz]	Band number	Frequency [Hz]	Band number	Frequency [Hz]
1	50	9	315	17	2000
2	63	10	400	18	2500
3	80	11	500	19	3150
4	100	12	630	20	4000
5	125	13	800	21	5000
6	160	14	1000	22	6300
7	200	15	1250	23	8000
8	250	16	1600	24	10000

How loud a sound is perceived depends on the effective pressure p of a sound wave, given in Pa. Often it is defined as the sound pressure level (SPL) relative to reference pressure p_{ref} on a logarithmic scale as shown in Equation 2.1.

$$SPL = 10 \log \left(\frac{p^2}{p_{ref}^2} \right) \tag{2.1}$$

where p_{ref} is $2 \cdot 10^{-5}$ Pa and SPL is in dB. Multiple noise sources can be combined to find the overall sound pressure level (OSPL) in dB with

$$OSPL(\theta) = 10 \log \sum_{i=1}^{n} 10^{SPL(f,\theta)/10} \tag{2.2}$$

where θ included the sound directivity angle. This can be used to find the total aircraft noise at each frequency if it is measured or computed from separate aircraft noise sources.

Sound pressure levels received by an observer are not necessarily at the same level as the sound pressure levels emitted by a source. Spherical spreading, atmospheric attenuation, reflection, Doppler shifts and other effects affect the perceived noise. Two corrections that are commonly used in semi-empirical noise modeling to correct for the sound waves traveling over a distance result in the SPL at the observer being

$$SPL_{receiver} = SPL_{source} - 20 \log r - \alpha(f) r. \tag{2.3}$$

This includes the spherical spreading through the propagation distance r in m and the atmospheric attenuation through a frequency-dependent absorption coefficient α over the propagation distance [41]. Multiple methods to compute the absorption coefficient have been developed, from simplifying it to average attenuation per frequency [42] to including temperature, humidity and frequency [43]. Higher frequencies get absorbed more easily [42].

Noise generated by aircraft is often defined with A-weighted SPL, indicating a correction that reflects the sensitivity of the human ear. This is done through a correction ΔL_A in dBA, given as

$$\Delta L_A = -145.528 + 98.262 \log f - 19.509 (\log f)^2 + 0.975 (\log f)^3 \tag{2.4}$$

where f is the frequency in Hz. This correction is applied to compute the overall A-weighted SPL (OASPL) or L_A, which is obtained using

$$L_A = 10 \log \sum_{i} 10^{\frac{SPL_i + \Delta L_{A,i}}{10}} \tag{2.5}$$

where the results over all frequencies are summed.

Another metric that accounts for frequency related annoyance is the perceived noise level (PNL) [44]. This can be computed with

$$PNL = 40.0 + \frac{10}{\log 2} \log N \tag{2.6}$$

where the total perceived noisiness N is found using

$$N = 0.85 n_{max} + 0.15 \sum_{i=1}^{24} n(i). \tag{2.7}$$

Lookup-tables for SPL and frequency are used to obtain the noy values $n(i)$ for each band. The maximum of $n(i)$ across the bands for each instance is n_{max} [45]. A tone correction can be added to take spectral irregularities into account. This is done using Equation 2.8. Correction factor C is computed following a lengthy procedure described in Appendix A.

$$PNLT = PNL + C \tag{2.8}$$

Both L_A and PNLT are methods to indicate noise levels of an event at one instant in time. However, sometimes the duration of an event is relevant as well. Although a reduction by a factor 2 in the intensity of the sound results in around 3 dB loss in noise level, this is not perceived as such by observers. A 10 dB lowering of the maximum level is needed to perceive loudness as actually reduced by half [46]. Therefore, a 10 dB downtime around the maximum noise level is often used to determine the flyover duration [44]. The sound exposure level (SEL) in dBA can be used to describe the noise level over a 10 dBA downtime. This is done using

$$SEL = 10 \log \left(\frac{1}{T_0} \int_{t_1}^{t_2} 10^{L_A(t)/10} dt \right) \tag{2.9}$$

where T_0 is a reference time of 1 s while t_1 and t_2 are the start and end of the 10 dBA downtime enclosing $L_{A_{max}}$ [5]. For the effective perceived noise level (EPNL), the methodology is very similar, with T_0 now being 10 s [6].

$$EPNL = 10 \log \left(\frac{1}{T_0} \int_{t_1}^{t_2} 10^{PNLT(t)/10} dt \right) \tag{2.10}$$

2.2.4. Installation effects

Installation effects occur due to interaction between components [37]. A TAW aircraft such as the A320 might be affected by engine-wing interaction, such as reflection of the engine noise by the wing or engine noise scattering at the wing trailing edge [47].

For the REBEL-C, the major installation effect is the engine placement on top of the aft fuselage, since the engine noise is shielded from an observer underneath the aircraft by the fuselage [48]. This causes an attenuation in noise that can be subtracted from the engine component noise via

$$SPL_{shielded} = SPL_{notshielded} + \Delta \tag{2.11}$$

where Δ is negative if the noise is reduced. Although noise might not be the most important driving factor behind the BWB design, placing the engines on top of fuselage certainly is a benefit in terms of noise reduction [13].

Even with an absorbing barrier between the noise source and an observer, sound waves can still travel around or over the barrier if it has finite dimensions. Maekawa provided a simple method to obtain noise reduction from a barrier of infinite length [49] where an observer is in the shadow zone as shown in Figure 2.7. The shadow zone is defined as a region with observers that rays emitted at the source cannot reach directly due to an object blocking them. The reason that noise is still perceived in the shadow zone for finite barriers is due to diffraction at the edges. When a sound ray hits a sharp edge

such as the top of the barrier in Figure 2.7, the edge starts acting as a monopole noise source, scattering the noise in every direction [50]. The scattered rays reach observers in the shadow zone.

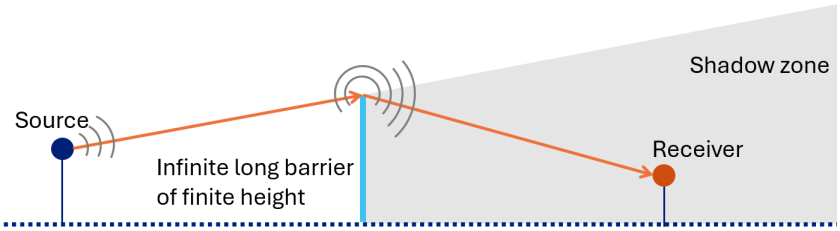

Figure 2.7: A source and barrier of infinite length and finite height. The receiver located in the shadow zone can still observe the noise due to diffraction around the edge of the barrier.

A distinction is made between the type of edge and its diffraction mechanism as illustrated by Figure 2.8. Sharp edges are found at the trailing edge of the wings and fuselage of a BWB and cause the edge-diffracted rays mentioned before. Creeping waves occur for convex surfaces where the rays are able to follow the curvature before leaving the surface [50]. These are more likely to be found at the leading edge of a BWB fuselage.

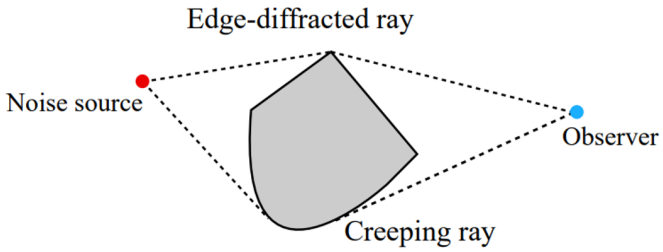

Figure 2.8: Schematic of ray diffraction on sharp and smooth edges, obtained from [51]

Earlier research on noise shielding has been performed for the Fokker 70 with fuselage-mounted engines [51]. Although the noise reduction due to engine placement was small, the shielding model itself was validated [51]. The same model has been used for a noise analysis of the Flying V, a flying wing with its engines placed on top of the airframe [18]. It shows a promising reduction in noise compared to its reference aircraft of up to 12.3 dBA during takeoff [52].

2.2.5. Blended wing body noise

Research on BWB noise has already been performed for the N3-X [12], N2A-EXTE [53], ERA-0009A [13], C11 [14] and Ascent 1000 [29]. Whereas most of these are designed with larger payload capacity in mind, the Ascent-1000 is most comparable to the REBEL-C in terms of passenger numbers although the range is much longer. All BWB given in Table 2.3 use (ultra)-high BPR turbofan engines located on top of the fuselage except for the N3-X design, which makes use of electric propulsors on the fuselage top and two turboshaft engines located at the wing tips [22]. Some overall design and performance parameters of these aircraft and four reference aircraft are given in Table 2.3 [35, 54–57].

Table 2.3: Design and performance parameters of five BWB aircraft and four TAW aircraft

Aircraft	N3-X	N2A-EXTE	ERA-0009A	C11	Ascent 1000	Airbus A320-214	Airbus A320-251neo	Boeing 777-200LR	Airbus A330-301
Number of passengers [-]	300	unknown	224	300	112	150-180	150-180	301-317	250-290
Range [nm]	7500	6000	8000	7500	3200	3000	3400	8700	6300
Cruise Mach number [-]	0.84	0.81	0.85	0.84	0.8	0.8	0.82	0.84	0.81
Bypass ratio [-]	29	10	18	7.0	9.0	5.7	12	9.1	5.3

The research performed by NASA, Boeing and DZYNE on BWB noise is limited to predicting noise for aircraft noise certification [12–14, 29, 53]. This certification is required to adhere to noise restraints for

takeoff, flyover and approach and is measured at specific locations underneath or besides the flight path [58]. The results show vast differences in which operation is the noisiest as shown in Figure 2.9 across the range of BWB aircraft. This is due to different assumptions made on the type of engines, methodology to obtain the engine noise shielding, airframe configuration and flight profiles. For all BWB, a version of the semi-empirical noise modeling program ANOPP has been used [12–14, 29, 53]. ANOPP has been developed by NASA as a fast semi-empirical noise modeling tool for aircraft noise predictions [59]. For the A320, A320neo, Boeing 777 and A330 data sheets from the noise certification have been used [60–63]. Overall, Figure 2.9 shows that all BWB designs are more quiet when compared to a TAW aircraft of similar capacity.

Comparing the A320 and A320neo shows the effect of using newer, ultra-high BPR turbofan engines. The A320neo is fitted with LEAP-1A engines with a BPR of 12:1 while the CFM56-5B4 engines of the A320 have a BPR of 5.7:1 [64]. The largest noise differences are found during takeoff and flyover for these two aircraft, where engine noise generally dominates [40]. The use of ultra-high BPR turbofans reduces the cumulative noise of the A320neo by 13.6 EPNdB compared to the A320.

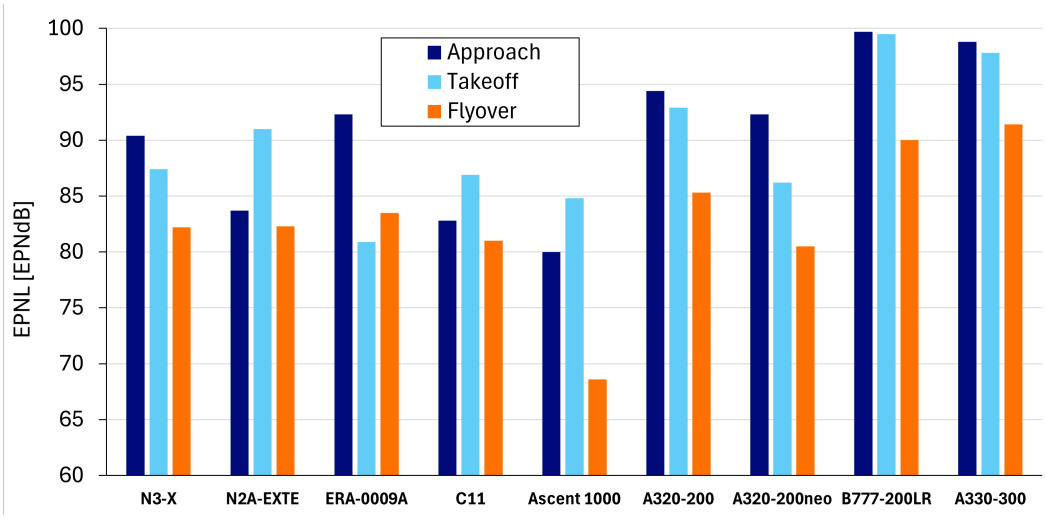

Figure 2.9: Approach, takeoff and flyover EPNL of BWB configurations and four reference aircraft for aircraft noise certification

2.3. Usage of Noise-Power-Distance Tables

NPD tables show the noise levels of a single event flyover for 10 set distances at certain thrust settings. These so called slant distances are 200, 400, 630, 1000, 2000, 4000, 6300, 10000, 16000 and 25000 ft [5]. A distinction is made between departure and approach due to differences in airframe configuration. Each NPD table shows results for a minimum of two power settings per flight phase. The NPD tables are obtained through noise measurements often performed during noise certification [15] for $L_{A_{max}}$, SEL, $PNLT_{max}$ and EPNL. This is done using standardized procedures defined in SAE AIR1845(A) [42].

These tables can be used in multiple ways. The first method is to compute the total noise of all noise events during a certain time interval at one location. When a full year is considered L_{DEN} is used, given in Equation 2.12. This can be computed using $L_{A_{max}}$ instead as well [36]. Different weights are applied for flights during the day, evening or night, where a 5 dBA penalty is applied for events during the evening and a 10 dBA penalty is added during the night [6]. In the equation below N_d stands for the number of events during day time, N_e is the number of evening events and N_n is the amount of events during the night [36]. L_{DEN} can be used to develop noise regulations [6].

$$L_{DEN} = 10 \log \left(\sum_{i=1}^{N_d} 10^{\frac{SEL_i}{10}} + \sum_{j=1}^{N_e} 10^{\frac{SEL_j+5}{10}} + \sum_{k=1}^{N_n} 10^{\frac{SEL_k+10}{10}} \right) - 75.0 \tag{2.12}$$

The second method is by generating noise contours, which show where on the ground a noise level is constant. It is generated using a grid and can be produced for a single event to show the footprint

or for multi-events using metrics such as L_{DEN}. These contours can be used for noise assessment around airports and to develop noise abatement procedures [6, 36]. An example of a noise contour is depicted in Figure 2.10 for an airport with two runways [6], where red indicates high noise levels and green indicates low levels. The lines indicate set boundaries.

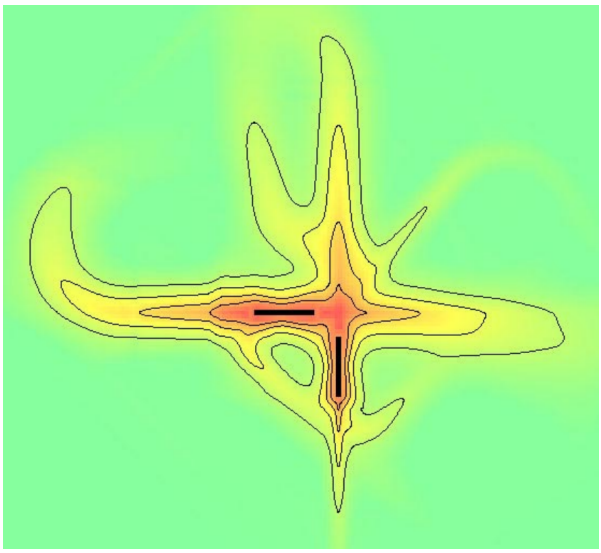

Figure 2.10: Noise contours for an airport with two runways, obtained from [6]

When a power setting and/or distance that is not in the NPD tables has to be used for calculations, ECAC Doc. 29 dictates how one can use inter- and extrapolation [5]. Furthermore, it describes how and which corrections for installation effects and lateral attenuation are to be done. These corrections are required to obtain the noise levels for any flight path of any aircraft in the ANP database [65].

3. Semi-Empirical Noise Modeling

Semi-empirical noise models have been created for the engine and airframe separately. These aircraft elements both consist of multiple components. Three major engine noise sources and all airframe noise sources that are used in SOPRANO are described in this chapter. All models predict the noise at 1 m distance from the source. Furthermore, the output from SOPRANO is compared with an in-house TU Delft semi-empirical modeling program which has been used in an earlier case study for the A320 [33].

3.1. Engine Noise

A turbofan consists of a number of stages with their own functions within the engine cycle. The turbofan stages and their numbering are given in Figure 3.1 for a twin spool turbofan [66] like the CFM56-5B4. The low pressure (LP)shaft connects the fan and LP compressor with the LP turbine, whereas the high pressure (HP) shaft connects the HP compressor and HP turbine.

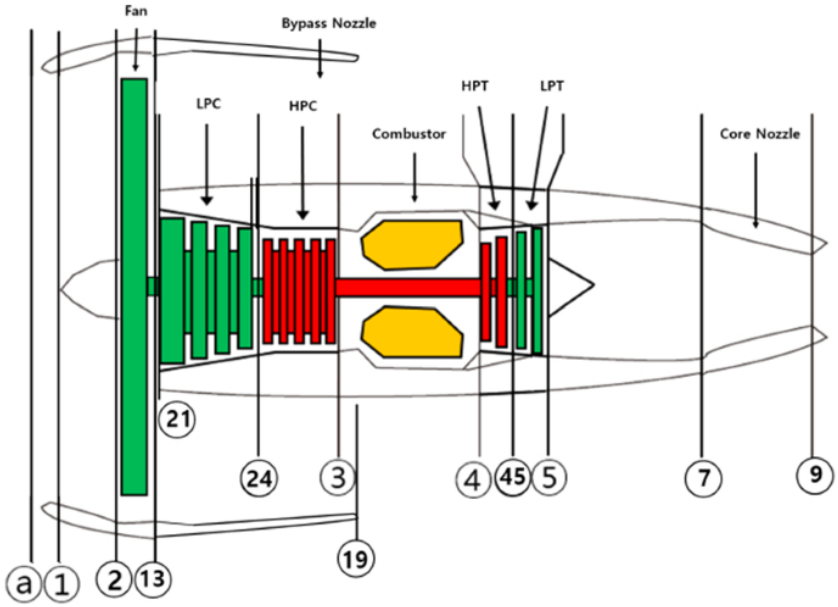

Figure 3.1: Schematic turbofan showing the numbering of each stage (obtained from Lee & Sung [66])

Engine noise consists of fan, combustion and jet noise, and to a smaller extend contains compressor and turbine noise as well. With the development of increasing BPR's in turbofans, the jet noise decreases [13]. Engine noise has lowered further due to improved fan design [67]. These reductions mean the core noise has become more pronounced. In this research fan, combustor and jet noise are considered.

3.1.1. Fan noise

Heidmann developed a method to predict fan and compressor noise by dividing the fan noise into five distinctive noise components [68]. The fan inlet noise consists of broadband noise, discrete tones and combined tones or buzz-saw noise. The fan exhaust noise contains broadband noise and discrete

tones. Broadband noise is generated by unsteady flow and turbulence passing the fan blades, while discrete tonal noise is caused by rotor-stator interaction [37]. The tonal noise is emitted at harmonic frequencies for which the blade passage frequency (BPF) is the fundamental frequency. The BPF is found through Equation 3.1 where N_1 indicates the fan rotational speed in rpm and N_B the number of blades.

$$\text{BPF} = \frac{N_1 N_B}{60} \tag{3.1}$$

Supersonic tips speeds of fan blades cause shock waves propagating upstream, which generate periodic noise called buzzsaw noise [37]. The blade tip Mach number M_{tip} is obtained with

$$M_{tip} = \frac{\pi d_{fan} N_1}{60 c_2} \tag{3.2}$$

where d_{fan} is the fan diameter in m and c_2 the speed of sound in m/s at the fan [69].

Heidmann's fan model has been revised by Kontos et al. to better fit the EPNL results of a flyover [70]. The governing equation for all five noise mechanisms is given by

$$SPL_{fan} = L_b + F_1(M_{tr}) + F_2(RSS) + F_3(\theta) + F_4(f) + F_5(f) \tag{3.3}$$

where function F_1 depends on the blade tip relative Mach number M_{tr}, F_2 includes the dependence on the rotor-stator spacing (RSS) and F_3 accounts for a directivity correction due to polar angle θ. F_4 and F_5 both depend on the frequency [51]. For all but the inlet discrete tonal noise, F_5 = 0. Each function is separately defined [70]. The blade tip relative Mach number M_{tr} is found through

$$M_{tr} = \frac{M_{tip}}{M_{tr_{des}}} \tag{3.4}$$

where $M_{tr_{des}}$ is the blade tip relative Mach number at the design point, for which maximum takeoff thrust is taken. For discrete tones, cutoff factor δ indicates the damping of certain tones in the fan duct. If δ, computed with Equation 3.5, is larger than 1.05 the tones are not considered. It is found using the ratio of number of stator vanes N_V to the number of rotor blades N_B. Sahai stated that generally fans are designed with $N_V/N_B > 1$ in mind to cut off specific tones [69].

$$\delta = \frac{M_{tip}}{\left|1 - \frac{N_V}{N_B}\right|} \tag{3.5}$$

Variable L_b in Equation 3.3 is expressed as

$$L_b = 20 \log\left(\frac{\Delta T_f}{\Delta T_{ref}}\right) + 10 \log\left(\frac{\dot{m}_2}{\dot{m}_{ref}}\right) \tag{3.6}$$

where ΔT_f indicates the temperature rise across the fan in K, ΔT_{ref} is a reference value of 0.555 K, $\dot{m}_2$ is the fan inlet mass flow rate in kg/s and $\dot{m}_{ref}$ is a reference value of 0.453 kg/s [68].

3.1.2. Combustion noise

Combustor noise is a low-frequency noise consisting of direct and indirect noise that gets generated by unsteady combustion [71]. General Electric developed a combustor noise model in the 1980's which is still in use today called SAE ARP876 [72]. It is based on the computation of the acoustic power that gets radiated from the combustor. The noise gets propagated through the turbines to the core nozzle, resulting a low frequency noise which is set to peak at 400 Hz [41].

Direct combustor noise can be computed using the overall power watt level ($OAPWL$) obtained through Equation 3.7 [73].

$$OAPWL = 10 \log\left(\frac{\dot{m}_3 c_{ISA}^2}{\Pi_{ref}}\right) + 10 \log\left[\left(\frac{T_{t,4} - T_{t,3}}{T_{t,3}}\right)^2 \left(\frac{P_{t,3}}{P_{ISA}}\right)^2 \left(\frac{\Delta T_{des,turb}}{T_{ISA}}\right)^{-4}\right] - 60.5 \tag{3.7}$$

Here, $\dot{m}_3$ is the combustor mass flow rate in kg/s, Π_{ref} is the reference acoustic power of 10^{-12} W and $T_{t,4} - T_{t,3}$ is the total temperature rise in the combustor in K. P_{ISA} and T_{ISA} are the standard sea

level pressure and temperature of 101325 Pa and 288.15 K, respectively [41]. The SPL is found using Equation 3.8 using spectral function F and directivity function D, which are obtained by using look-up tables [72].

$$SPL_{comb} = OAPWL + F_{f,comb} + D_{f,comb} + 10\log\left(\frac{\Pi_{ref}\rho_0 c_0}{4\pi p_{ref}^2}\right) \tag{3.8}$$

3.1.3. Jet noise

Multiple jet noise methods have been developed over the years by Stone et al. [74–76]. Continuing on their earlier work, Stone et al. further improved the coaxial jet noise prediction method for high BPR turbofans [77]. This was done by introducing three regions of jet mixing noise:

- Large scale mixing noise due to large scale turbulence from jet flow mixing with ambient air flow;
- Small scale mixing noise due to small scale turbulence from the bypass flow mixing with the ambient air flow in the outer shear layer;
- Transitional or intermediate scale mixing noise due to the mixing of core and bypass flow in the inner shear layer [77].

Each mixing region has its own source location and set of equations. Overall, the jet mixing noise is described by Equation 3.9. The uncorrected overall SPL ($UOSPL$) in the far field has not been corrected for directivity yet [77].

$$\begin{aligned} UOSPL = A_s + 10\log\left[\left(\frac{\rho_0}{\rho_{ISA}}\right)^2\left(\frac{c_0}{c_{ISA}}\right)^4\right] + 10\log\left(\frac{A_n}{r^2}\right) + 10\omega\log\left(\frac{\rho_e}{\rho_0}\right) \\ + 10C_1\log\left[\frac{\left(\frac{V_e}{c_0}\right)^{N_1}}{B_1 + B_2\left(\frac{V_e}{c_0}\right)^{N_1-N_2}}\right] - 20\log\left[(1+M_c\cos\theta)^2 + (0.3M_c)^2\right] \end{aligned} \tag{3.9}$$

In this equation A_s is a scaling parameter, A_n is the local nozzle exit area in m^2, r is the distance between the source and observer in m, ρ_e is the density depending on the jet region in kg/m^3, V_e is the effective jet velocity given by Equation 3.10 in m/s, M_c is the convective Mach number defined in Equation 3.11, θ is the polar angle from the inlet axis in degrees and ω is the density factor computed using Equation 3.12. Coefficients C_1, B_1, B_2, N_1 and N_2 are given in Table 3.1 [51]. Air density ρ_0 and speed of sound c_0 describe the ambient conditions in kg/m^3 and m/s, respectively.

Table 3.1: Coefficients for the general uncorrected OUSPL

Coefficient	Large	Small	Intermediate
C_1	1	7.5	7.5
B_1	1	0	0
B_2	0.02	1	1
N_1	8	2	2
N_2	3	1	1

The effective velocity V_e is found with

$$V_e = V_n\sqrt{1 - M_0\left(\frac{c_0}{V_n}\right)} \tag{3.10}$$

where V_n depends on the mixing scale and M_0 is the ambient flow Mach number. The convective Mach number M_c of the jet component is defined by

$$M_c = n_c\left[\left(\frac{V_e}{c_0}\right) - M_0\right] \tag{3.11}$$

where n_c is a scale-size dependent coefficient [77]. The density component ω is obtained through

$$\omega = \frac{3(V_e/c_0)^{3.5}}{0.6 + (V_e/c_0)^{3.5}} - 1 \tag{3.12}$$

for large and small scale mixing noise. Stone et al. mention getting good results with ω_T = 0 for the transitional scale [77].

The source location X_s for each scale is different. For a mixing region the location is given by

$$X_s = \frac{L + (X_C + \theta/\theta_F)d_j^{C_2}}{LSF} \tag{3.13}$$

where L is the displacement of the start of the mixing region from the fan nozzle exit place in m, while X_C and θ_F (in $^\circ$) are the empirical length and angle scaling factor. LSF is the linear scale factor (full-scale dimension over model-scale dimension), θ is the uncorrected directivity angle in $^\circ$ and C_2 is a constant. The parameters are given in Table 3.2 [77].

Table 3.2: Parameters used for the source locations

Parameter	Large	Small	Intermediate
L	L_{19}	0	L_{19}
X_C	4	0	0
θ_F	30	45	45
C_2	-0.25	1	1

The SPL is then obtained for all three scale mixing noises at a distant point by using tables for OUSPL and the Strouhal number per corrected directivity angle $\bar{\theta}$, where

$$SPL_{jet} = \text{[SPL - UOSPL]}_{table}(St) + UOSPL + \Delta SPL \tag{3.14}$$

with the data obtained from General Electric's turbofan engine data base [77].

The Strouhal number St required for these tables is found using

$$St = \frac{f d_j}{V_e} \left(\frac{T_j}{T_0}\right)^{0.4+(1+\cos\bar{\theta})} \tag{3.15}$$

where d_j is the characteristic diameter in m, T_J is the jet region stagnation total temperature in K and T_0 is the ambient total temperature in K. The effective directivity angle with respect to the inlet, $\bar{\theta}$ is defined as

$$\bar{\theta} = \theta_{cor} \left(\frac{V_n}{c_0}\right)^{0.1} \tag{3.16}$$

where the corrected angle θ_{cor} is found through

$$\theta_{cor} = \arccos\left[\frac{R}{R_{cor}}\cos\theta + \frac{X_s}{R_cor}\right]. \tag{3.17}$$

In this equation R is the distance from the nozzle exit to the observer in m, R_{cor} is the corrected distance in m due to the source location being some distance away from the nozzle face and X_s is the axial source location relative to the nozzle exit in m [77]. Both $\bar{\theta}$ and θ_{cor} are given in $^\circ$. The term ΔSPL in Equation 3.14 has been added to bring the far field results, measured at 100 m, back to 1 m distance. This correction is applied in SOPRANO using

$$\Delta SPL = 20\log\left(\frac{100}{1}\right). \tag{3.18}$$

3.1.4. Gas turbine Simulation Program

The conditions required as inputs for each model are computed using GSP. It computes the conditions in each stage by using the laws of conservation and isentropic relations. Look-up tables are used for losses and effectiveness ratings under the specified conditions. Due to compression, combustion and expansion the conditions in each stage are different. By modeling a turbofan in GSP, these conditions can be found for different thrust settings at varying altitudes and airspeeds [78].

3.2. Airframe Noise

Airframe noise can be modeled using Fink's method [79], which has been adopted into ANOPP following the method outlined by Zorumski [80]. It describes noise from the wing without any additional lifting surfaces, the tail surfaces noise, the HLD's noise and the landing gear noise. Turbulent flow around structures, side-edge vortices and gaps between airframe components all generate noise [37, 81]. Figure 3.2 shows some of these noise mechanisms.

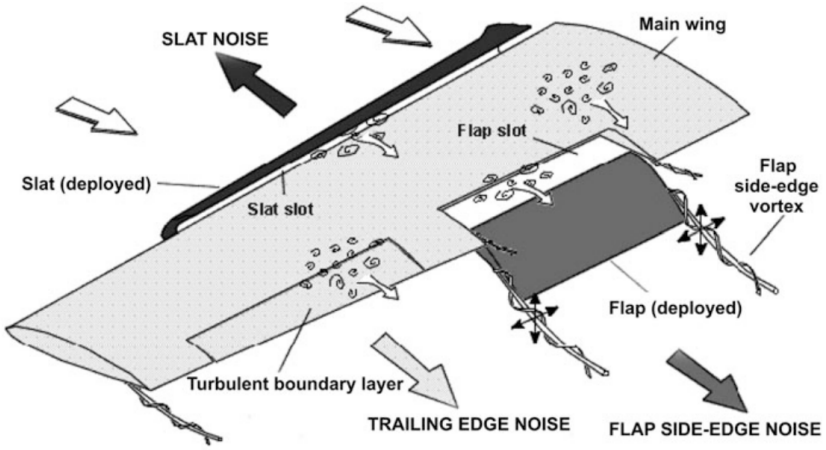

Figure 3.2: Mechanisms of possible sound sources on a wing with deployed high-lift devices, obtained from [81]

3.2.1. Clean wing and tail noise

Fink defined the trailing edge noise for the wing and tail surfaces [79]. The same basis is defined for all airframe components, with the acoustic pressure $\langle p_i \rangle$ in Pa computed using Equation 3.19, which is based on the acoustic power Π in W, the distance to the observer r in m, spectral function $F(St)$, directivity function $D(\theta)$ with θ the polar angle in $^\circ$ and ambient conditions M_0, ρ_0 in kg/m^3 and c_0 in m/s. Acoustic power Π is obtained through Equation 3.20 [69]. Whereas this method was developed for conventional aircraft with restricted sweep angles, the REBEL-C does have some high sweep angles. Furthermore, the higher angle of attack normally operated by BWB might effect the results [82]. Both have to be considered when applying at this methodology to BWB aircraft.

$$\langle p_i \rangle^2 = \frac{\Pi_i}{4\pi r^2} \frac{F_i(St) D_i(\theta)}{(1 - M_0 \cos\theta)^4} \rho_0^2 c_0^4 \tag{3.19}$$

$$\Pi_i = K_i M_0^{a_i} G_i b_w^2 \tag{3.20}$$

with K and a as constants depending on the airframe noise component and b_w the wing span in m [69]. For a clean wing, $K_w = 4.464 \cdot 10^{-5}$ and $a_w = 5$. Assuming a standard flat plate turbulent boundary layer the following relation can be used for G_w [80]:

$$G_w = \delta_w^* = 0.37 \frac{A_w}{b_w^2} \left(\frac{\rho_0 M_0 c_0 A_w}{\mu_0 b_w} \right)^{-0.2} \tag{3.21}$$

where A_w is the wing surface area in m^2 and μ_0 the ambient kinetic viscosity of air in m^2/s. For a horizontal and vertical tail surface, G_h and G_v are found by Equation 3.22 and Equation 3.23, respectively. K and a are the same for the wing and the tail surfaces.

$$G_h = 0.37 \frac{A_h}{b_h^2} \left(\frac{\rho_0 M_0 c_0 A_h}{\mu_0 b_h} \right)^{-0.2} \left(\frac{b_h}{b_w} \right)^2 = 0.37 \frac{A_h}{b_w^2} \left(\frac{\rho_0 M_0 c_0 A_h}{\mu_0 b_h} \right)^{-0.2} \tag{3.22}$$

$$G_v = 0.37 \frac{A_v}{b_v^2} \left(\frac{\rho_0 M_0 c_0 A_v}{\mu_0 b_v} \right)^{-0.2} \left(\frac{b_v}{b_w} \right)^2 = 0.37 \frac{A_v}{b_w^2} \left(\frac{\rho_0 M_0 c_0 A_v}{\mu_0 b_v} \right)^{-0.2} \tag{3.23}$$

The spectral function $F(St)$ and the Strouhal number $St(f)$ depend on the component as well. The latter is given by Equation 3.24, with $l = G_i b_i$, choosing the appropriate values of G_i and b_i depending on the component [80]. Depending on the type of BWB configuration, two wing designs for $F(St)$ as given in Equation 3.25 are;

- Rectangular wings: $e = 0.613$, $g = 1.50$;
- Delta wings: $e = 0.485$, $g = 1.35$

$$St(f) = \frac{fl(1 - M_0 \cos\theta)}{M_0 c_0} \tag{3.24}$$

$$F_{w,h,v}(St) = e(10St)^4 \left((10St)^g + 0.5\right)^{-4} \tag{3.25}$$

The directivity is found using D_w for the wing and horizontal tail with Equation 3.26 and D_v is used for a vertical tail with Equation 3.27.

$$D_w(\theta, \phi) = 4\cos^2(\theta/2)\cos^2\phi \tag{3.26}$$

$$D_v(\theta, \phi) = 4\cos^2(\theta/2)\sin^2\phi \tag{3.27}$$

In these equations, θ is the polar directivity angle and ϕ is the azimuthal directivity angle [69].

3.2.2. High-lift devices noise

Slat noise is computed by taking two noise generating mechanisms into account. A slat generates noise itself and the presence of a slat increases the wing trailing edge noise by impacting the wing boundary layer [80]. The acoustic power is found using Equation 3.20 with the values K_i, a_i and G_i as for the wing. The Strouhal number is computed with Equation 3.24. The spectral function for slat noise itself is computed using

$$F_s(St) = 0.613(2.19St)^4 \left((2.19St)^{1.5} + 0.5\right)^{-4} \tag{3.28}$$

and is added to the spectral function of the wing via

$$F_{s,total}(St) = F_s(St) + F_{w,h,v}(St) \tag{3.29}$$

with $F_{w,h,v}(St)$ as given in Equation 3.25. The directivity is found using the same equation, Equation 3.26, as for the wing. The deflection angle is not included in this method, the slat is either deployed or retracted.

The flap noise is produced through turbulence around the flaps and depends on the number of slots [69]. Starting from Equation 3.20, $a_f = 6$, $K_{f,12} = 2.787 \cdot 10^{-4}$ for single and double slotted flaps and $K_{f,3} = 3.509 \cdot 10^{-4}$ for triple slotted flaps. The function G_f is now

$$G_f = \frac{A_f}{b_w^2} \sin^2 \Theta_f \tag{3.30}$$

with A_f the flap surface area in m^2 Θ_f the flap deflection angle in $^\circ$. The Strouhal number $St(f)$ is found with

$$St_(f) = \frac{fA_f}{b_f M_0 c_0}[1 - (M_0 \cos\theta)]. \tag{3.31}$$

The Strouhal number is then used to compute the spectral function. For single and double slotted flaps this is given in Equation 3.32 and for triple slotted flaps this is given in Equation 3.33 [80].

$$F_{f_{12}}(St) = \begin{cases} 0.0480St_f, & St_f < 2 \\ 0.1406St_f^{-0.55}, & 2 \leq St_f \leq 20 \\ 216.49St_f^{-3}, & St_f > 20 \end{cases} \tag{3.32}$$

$$F_{f_3}(St) = \begin{cases} 0.0257St_f, & St_f < 2 \\ 0.0536St_f^{-0.0625}, & 2 \leq St_f \leq 75 \\ 17078St_f^{-3}, & St_f > 75 \end{cases} \tag{3.33}$$

The directivity function is defined in ANOPP [80] as

$$D_f(\theta, \phi) = 3(\sin\Theta_{flap}\cos\theta + \cos\Theta_{flap}\sin\theta\cos\phi)^2. \tag{3.34}$$

3.2.3. Landing gear noise

Fink simplified the noise generating mechanisms of landing gear by assuming two noise sources, the wheels and the struts [79]. For the wheels, two sets of acoustic power function parameters are given, one for landing gear with one or two wheels LG_{12}, and one for four or more wheels LG_{4+} [52]. For BWB, Guo et al. stated that the local velocity encountered by the landing gear underneath might be higher than for conventional aircraft configurations, increasing the noise [13].

Starting of from Equation 3.20, geometry parameter G_i is now

$$G_i = \begin{cases} N_w \left(\frac{d_w}{b_w}\right)^2, & LG_{12} \text{ and } LG_{4+} \\ \left(\frac{d_w}{b_w}\right)^2 \frac{l_s}{d_w}, & \text{strut} \end{cases} \tag{3.35}$$

where N_w is the number of wheels, d_w is the wheel diameter, b_w is the wing span and l_s is the strut length, all in m [69].

Parameter K_i is now $K_{LG,12} = 4.349 \cdot 10^{-4}$, $K_{LG,4+} = 3.414 \cdot 10^{-4}$, $K_{strut} = 2.453 \cdot 10^{-4}$ for both nose and main landing gear. For all components, $a = 6$ [80].

The Strouhal number is computed with

$$St(f) = \frac{fd_w}{M_0 c_0}(1 - M_0\cos\theta) \tag{3.36}$$

for both wheels and struts. The spectral function differs per component and is computed using

$$F_i(St) = \frac{A_i St_i^{\sigma_i}}{(B_i + C_i St_i^{\mu_i})_i^q} \tag{3.37}$$

where σ, μ, q, A, B and C are constants given in Table 3.3 [51, 80].

Table 3.3: Spectral density parameters for landing gear noise

Parameter	LG_{12}	LG_{4+}	$Strut_{12}$	$Strut_{4+}$
σ	2	2	2	3
μ	2	2	8	2
q	-2.25	-1.5	-1	-3
A	13.59	0.0577	5.325	1.28
B	12.5	1	30	1.06
C	1	0.25	1	1

Finally, Fink [80] modeled the directivity functions as

$$D_i(\theta, \phi) = \begin{cases} \frac{3}{2}\sin^2\theta, & LG_{12} \text{ and } LG_{4+} \\ 3\sin^2\theta\sin^2\phi, & \text{strut.} \end{cases} \tag{3.38}$$

3.3. Noise Model Comparison

The modules described above are not only implemented into SOPRANO, Arntzen created a program incorporating the same semi-empirical methods as well [83], predicting the noise for the various aircraft components. This model will be used to verify SOPRANO.

3.3.1. In-House Model TU Delft

The semi-empirical modeling program is based on ANOPP and shows results at 1 m distance [83]. It was later improved on by Vieira [51] and von den Hoff [37]. The implemented component modules are:

- Fan noise, modeled with [70]. It was updated using [84] from the Engineering Sciences Data Unit (ESDU);
- Core noise, obtained with SAE ARP876 [72]. The directivity function is taken from ESDU [85];
- Jet noise, modeled with Stone's method for coaxial jets [77];
- Airframe noise, calculated with Fink's model [80] and directivity functions from ESDU [86].

An analysis for a direct flyover of an Airbus A320 was performed in [33]. The BPF was obtained from measurements. The flight conditions were taken from experimental data at Schiphol Airport and the engine conditions were gathered from GSP for the CFM56-5B4 turbofan engine. It has a BPR of 5.7 [87] and a maximum thrust output of 120.1 kN [88]. A departure and arrival were analyzed and compared to measured noise. Both flyovers were measured directly overhead. The departing aircraft flew at 400 m altitude with with a velocity of 70 m/s. The resulting polar plot is shown in Figure 3.3a. While the high frequency range was predicted rather well with the model, an under prediction of noise in the low frequency range was observed for the spectrum at a polar angle of 90°. The engine noise is dominant for all polar angles, with the fan and combustor dominating the most except for high polar angles, where jet noise start dominating. The arriving aircraft were measured overhead at 50 m altitude with an airspeed of 65 m/s. The results are shown in Figure 3.3b. It was shown that fan and combustor noise dominate, with the airframe contributing for polar angles below 60° [33]. The jet contribution is negligible. The spectra for the 90° overhead angle including the measurements taken are shown in Appendix B.

3.3.2. SOPRANO

Using the same approach and departure conditions, SOPRANO is compared to Arntzen's program using the same modules. A jet noise module called Stone 2009 [77] has been added for this research by Anotec Engineering. The polar plots for departure and arrival are shown in Figure 3.3c and Figure 3.3d, respectively. The spectra can be found in Appendix B.

When comparing the departure in Figure 3.3a to Figure 3.3c some differences are noted. These differences are

- Jet noise is slightly larger with SOPRANO due to the ambient atmospheric density that is a function of the ambient conditions. This differs from the density used in [33];
- Combustor noise is larger using Arntzen's program due to different directivity values [85];
- Fan noise differs significantly. The first reason for this is the exclusion of $F1$ for inlet broadband noise in Arntzen's program. Secondly, the ESDU model is different in terms of directivity [84], making this comparison somewhat difficult;
- The airframe noise is larger in SOPRANO. The Doppler factor $1/(1-M_0 \cos\theta)$ is included whereas in Arntzen's program it was not used. Furthermore, the directivity equations from ESDU [86] change the output.

The same pattern can be seen when comparing the approach in Figure 3.3b and Figure 3.3d. Since this makes the comparison somewhat difficult, a revised version of Arntzen's program was made. The combustor module was modified to include the directivity input from SAE ARP876F [72]. The airframe noise model in the revised version was updated by Anotec Engineering. It includes the directivity equations from Fink's method and the Doppler term $1/(1 - M_0 \cos\theta)$. The fan noise now includes the term $F1$. Since however not only the directivity but rather the functions themselves are adapted [84], differences will persist. Due to time limitations the fan model was not reverted back to the original.

A better fit of the results was then found between Figure 3.3c and Figure 3.3e for departure. The combustor noise is similar, showing this module works well in SOPRANO. The fan noise still differs due to the different methods used, however it is much closer. It is therefore assumed this module works as intended in SOPRANO. The airframe noise now matches almost perfectly as well. It was found that the flap noise is slightly lower from SOPRANO, however the reason for this is not known. The results shown in Figure 3.3d and Figure 3.3f for approach show the same trends. The airframe component

spectra and polar plots are shown in Appendix B. Although only the combustor noise matches perfectly for both cases, the differences with the other noise modules can be explained. It is therefore assumed that SOPRANO works as intended.

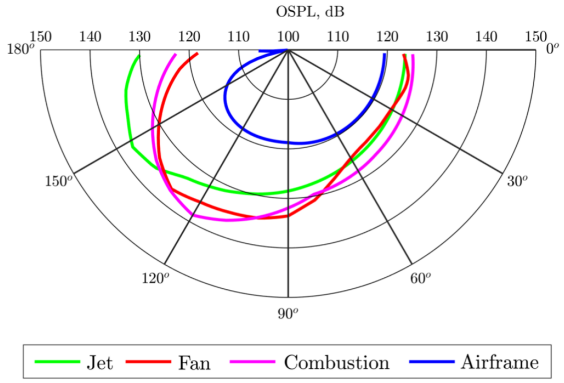

(a) Polar plot for a departing A320 using Arntzen's program, obtained from [33]

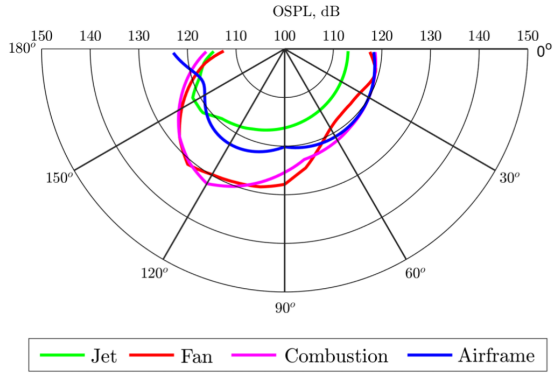

(b) Polar plot for an approaching A320 using Arntzen's program, obtained from [33]

Soprano

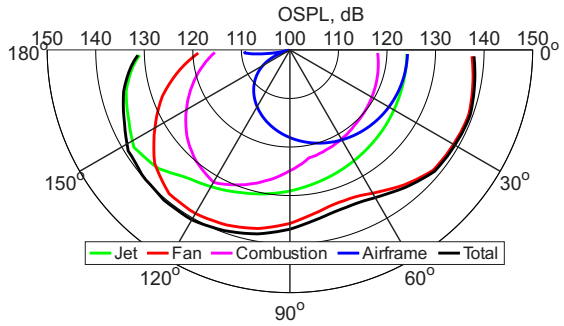

(c) Polar plot for a departing A320 using SOPRANO

Soprano

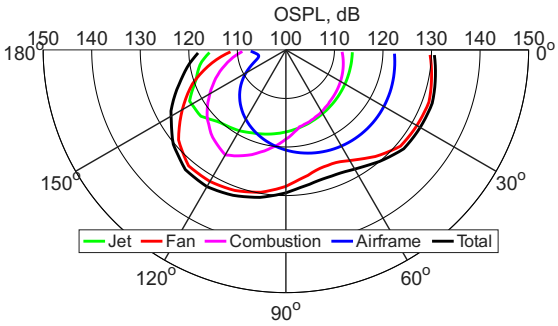

(d) Polar plot for an approaching A320 using SOPRANO

revised Arntzen

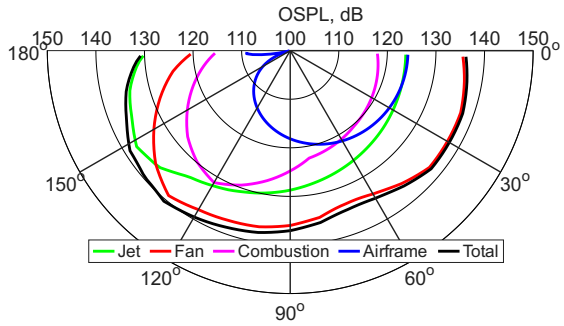

(e) Polar plot for a departing A320 using the revised program from Arntzen

revised Arntzen

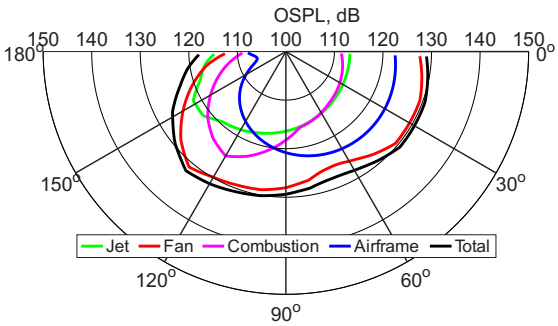

(f) Polar plot for an approaching A320 using the revised program from Arntzen

Figure 3.3: Polar plots for the A320 from [33], SOPRANO and the revised model

4. Noise Shielding

The design of the REBEL-C aims to reduce engine noise by placing the turbofan engines on top of the fuselage. The fuselage and wings then act as a sound barrier for observers on the ground. The amount of attenuation resulting from this needs careful analysis, since sound waves can get diffracted by edges of an object. The method to compute the reduction in noise due to shielding is described here, followed by the results from the noise shielding model.

4.1. Theory

There have been multiple methods developed to determine the attenuation due to a barrier, all with their own benefits and downsides [51]. SOPRANO contains a noise shielding model based on Maekawa [49], however is rather simplified and only applicable to specific geometry types [51]. According to Vieira [51], a model suitable for aircraft with high degrees of curvature ideally is

- Highly accurate;
- Able to implement complex geometries for a BWB aircraft shape;
- Capable of including both edge-diffracted and creeping rays;
- Capable of including noise directivity;
- Computationally simple;
- Capable to analyze all required frequencies.

The best suited method found was using Kirchhoff's theory of diffraction [51]. Since this method is much more computationally expensive than the one based on Maekawa [49], it was not deemed possible to implement it into SOPRANO. Therefore, the noise reduction due to shielding was computed separately and the results were assembled into tables. These ΔSPL tables were then implemented into SOPRANO.

4.1.1. Kirchhoff's theory of diffraction

Kirchhoff's theory of diffraction describes high frequency diffractions of a monopole noise source through an aperture in a rigid screen of infinite size, shown in Figure 4.1a and Figure 4.1b. Using Green's theorem, Kirchhoff found a method to describe the acoustic pressure over the surface of the aperture [89].

Consider aperture σ in a screen $\bar{\sigma}$, shown in Figure 4.1b. Point $\boldsymbol{y}$ is a point of the aperture. A monopole source is producing noise at location $\boldsymbol{x}_Q$. The incident field describing the wave propagating from source to observer without any obstacle is described with

$$p_i = e^{ikR}/R, \quad \boldsymbol{R} = \boldsymbol{x} - \boldsymbol{x}^Q, \quad R = |\boldsymbol{R}| \tag{4.1}$$

where k is the wavenumber and R is the distance from source to observer in m [91].

Assuming there is no acoustic pressure already present at the backside of the screen, the pressure field $p_s^{aperture}$ at this backside of the screen at observer position $\boldsymbol{x}$ can be obtained using the Kirchhoff integral over the aperture. This integral is defined as

$$p_s^{aperture} = \frac{1}{4\pi} \int_\sigma \left[p_i \mathbf{n} \cdot \nabla \frac{e^{ikr}}{r} - \frac{e^{ikr}}{r} \mathbf{n} \cdot \nabla p_i \right] dS \tag{4.2}$$

where $\boldsymbol{n}$ is is unit vector normal to the surface, $\boldsymbol{r} = \boldsymbol{y} - \boldsymbol{x}$ and $r = |\boldsymbol{r}|$ [51].

The scattered pressure field at the observer over the aperture is found with

$$p_s^{aperture} = p_i \chi + p_d \tag{4.3}$$

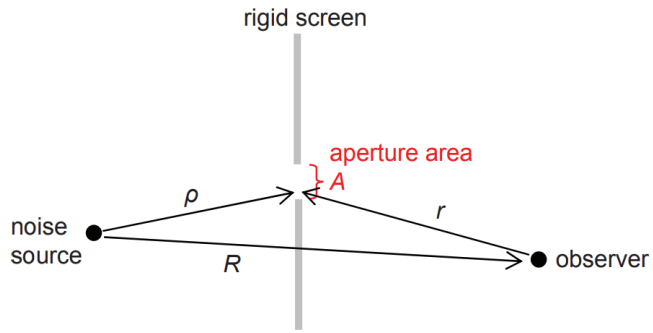

(a) Geometry used by Kirchhoff to obtain the Kirchhoff diffraction integral where the screen can have any shape, taken from [90]

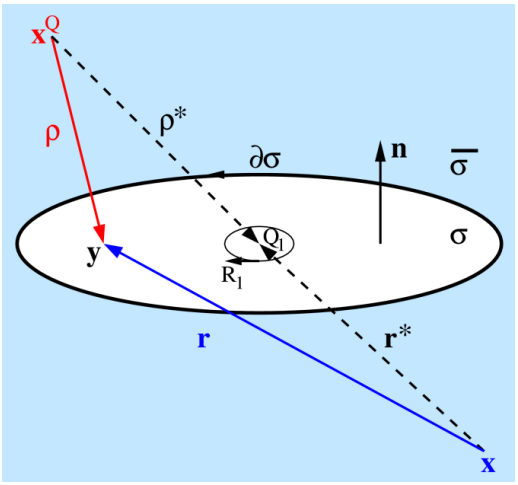

(b) 3-dimensional representation of the Kirchhoff integration area, where x^Q is the source position and x the observer position, taken from [91]

Figure 4.1: Aperture σ in a screen $\bar{\sigma}$ with source location $\boldsymbol{x}^{\boldsymbol{Q}}$ and observer position $\boldsymbol{x}$

where p_d is the boundary diffracted field pressure and χ is an unit function. It is one if the surface encloses the direct line between source and observer (R) and zero otherwise [92].

To reduce the computational costs Maggi and Rubinowicz transformed the surface integral into a contour line integral along contour $\partial\sigma$ [90, 93]. The boundary diffracted field is then given as

$$p_d = \frac{1}{4\pi}\int_{\partial\sigma} \frac{e^{ik\varrho}}{\varrho}\frac{e^{ikr}}{r}\frac{(\boldsymbol{\varrho}\times\mathbf{r})\cdot ds}{\varrho r + \boldsymbol{\varrho}\cdot\mathbf{r}} \tag{4.4}$$

where $\boldsymbol{\varrho} = \boldsymbol{y} - \boldsymbol{x}_Q$. When the ray between source and observer is at the edge of the departure ($\varrho r + \boldsymbol{\varrho}\cdot\boldsymbol{r} = 0$), a singularity is present. It is shown by Vieira et al. [92] that the best suited method to solve for this was using the Modified Theory of Physical Optics (MTPO) due to the relative short computational time compared to the Diffraction Integral Method as described by Lummer in [91].

To ensure more types of sources could be used, Miyamoto and Wolf found a method where the source directivity could be captured in the incident pressure $p_i(\varrho)$ [93], as given by Equation 4.5. The singularity from Equation 4.4 is still present here and will be addressed subsection 4.1.2.

$$p_d = \frac{1}{4\pi}\int_{\partial\sigma} p_i(\varrho)\frac{e^{ikr}}{r}\frac{(\boldsymbol{\varrho}\times\mathbf{r})\cdot ds}{\varrho r + \boldsymbol{\varrho}\cdot\mathbf{r}} \tag{4.5}$$

The scattered field due to the shielding object is found using the interchangeability of the screen and aperture as given in Babinet's principle, stating that the free source field p_i is the sum of the diffracted fields on both sides of the screen [90] as given in Equation 4.6.

$$p_s^{obstacle} = p_i - p_s^{aperture} \tag{4.6}$$

Finally, the reduction ΔSPL due to shielding can be found with

$$\Delta SPL = -20\log\left|\frac{p_s^{obstacle}}{p_i}\right|. \tag{4.7}$$

4.1.2. Modified Theory of Physical Optics

To solve for the singularity present when the ray is at the edge of the aperture in Equation 4.4 and Equation 4.5, the Modified Theory of Physical Optics (MTPO) is used. It can be used in the high frequency domain to find incident waves and incident diffracted waves [94].

Before explaining MTPO, the line integral over the aperture contour needs to be discretized first into straight sections of equal length $\boldsymbol{y}(s)$ by using Equation 4.8, where $\boldsymbol{y}_0$ is the first arbitrary point of the contour, $\boldsymbol{e}$ is the segment unit direction and s_a and s_b are the start and end points of the segment [51].

$$\boldsymbol{y}(s) = \boldsymbol{y}_0 + s\mathbf{e}, \quad s_a < s < s_b \tag{4.8}$$

Taking the straight segments Γ of contour $\partial\sigma$ resulting from this, Miyamoto and Wolf's diffraction line integral [93] can be rewritten to Equation 4.9, with I_Γ being the diffraction line integral over the aperture evaluated using segments Γ.

$$I_\Gamma = \frac{1}{4\pi}\int_\Gamma \frac{1}{\varrho}\frac{1}{r}\frac{(\boldsymbol{\varrho}\times\mathbf{r})\cdot ds}{\varrho r + \boldsymbol{\varrho}\cdot\mathbf{r}} e^{ik(\varrho+r)} \tag{4.9}$$

This can be transformed into a Fourier integral with as basis

$$I_\Gamma = \int_\Gamma A_f(s) e^{ikg(s)} ds \tag{4.10}$$

where $A_f(s)$ is the amplitude and $g(s)$ is the phase. The method of stationary phase is used to solve this equation, however it does introduce another singularity, this time in the contribution of the segments' end points [51]. This is then solved by using the method of uniform theory of diffraction [91]. This theory describes how the scattered field behaves like a Fresnel integral in the points connecting the segments together. Changing the variable gives the opportunity to introduce a detour. Combining this with the fundamental property of the Fresnel integral gives Equation 4.11, as can be found in appendix B of [51].

$$\begin{aligned} I_\Gamma = \sqrt{\pi} e^{i\frac{\pi}{4}} e^{ikg(s^*)} \{ & E(s^*)(U(-t_d(s_a)) - U(-t_d(s_b))) \\ & + E(s_a)\mathsf{sign}(t_d(s_a))F[|t_d(s_a)|] - E(s_b)\mathsf{sign}(t_d(s_b))F[|t_d(s_b)|]\} \end{aligned} \tag{4.11}$$

where s^* is the stationary phase point, t_d is the detour parameter and U is the unit step function, equal to 1 for $U(-x) \leq 0$ and 0 otherwise. $E(s)$ is given by Equation 4.12, while the Fresnel integral $F(x)$ is given by Equation 4.13.

$$E(s) = \frac{A_f(s)}{h(s)} \tag{4.12}$$

$$F[x] = \frac{e^{-(\pi/4)}}{\sqrt{\pi}} \int_x^\infty e^{it_d^2} dt = U(-x) + \mathsf{sign}(x)F(|x|) \tag{4.13}$$

The function $h(s)$ depends on $g(s)$ as described in appendix C of [51], and is given by Equation 4.14. The asymptotic expression of the Fresnel integral is described using Equation 4.15.

$$h(s) = \begin{cases} k\frac{g'(s)}{2t_d(s)}, & \text{if} s \neq s^* \\ \sqrt{\frac{kg"(s^*)}{2}}, & \text{if} s = s^* \end{cases} \tag{4.14}$$

$$\mathsf{sign}(x)F[|x|] \simeq \frac{e^{i(\pi/4)}}{2\sqrt{\pi}}\frac{e^{ix^2}}{x} \tag{4.15}$$

The first singularity, $\rho r + \boldsymbol{\rho}\cdot\mathbf{r} = 0$, is still present in Equation 4.11. To eliminate this, detour parameter ξ is used so that Equation 4.15 is replaced. This results in the diffraction line segment integral I_Γ becoming

$$\begin{aligned} I_\Gamma = 2\sqrt{\pi}\mathsf{sign}(\xi)F[|\xi|]\{ & E(s^*)(U(-\xi_a) - U(-t\xi_b)) \\ & + E(s_a)\mathsf{sign}\xi_a)F[|\xi_a|] - E(s_b)\mathsf{sign}(\xi_b)F[|\xi_b|]\} \end{aligned} \tag{4.16}$$

with detour parameter ξ defined as

$$\xi(s, \boldsymbol{P}) = \epsilon_\xi(\boldsymbol{P})\sqrt{k[g(s) - |\boldsymbol{R}|]} \tag{4.17}$$

where ϵ_ξ is equal to -1 if point $\boldsymbol{P}$ is in the shadow zone and 1 otherwise, $g(s) = |\boldsymbol{\rho}| + |\boldsymbol{r}|$ [51] and $|\boldsymbol{R}|$ is the direct path between source and observer [91].

All line segment contributions are then added up to find the total boundary diffracted field p_d, after which the scatter field at to the aperture $p_s^{aperture}$ can be found using Equation 4.3, the pressure field behind the obstacle $p_s^{obstacle}$ using Equation 4.6 and finally the reduction due to shielding by using Equation 4.7.

4.1.3. Creeping rays

So far only edge-diffracted rays have been taken into account. For a BWB with a high area of curvature, creeping rays need to be incorporated as well. Assume the rays follow the curvature for a distance t_{curve} before going to an observer, as shown in Figure 4.2.

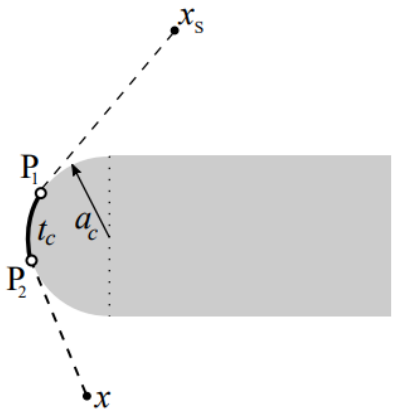

Figure 4.2: Schematic representation of an edge with curvature, taken from [51]

An important assumption is that creep only occurs for $kr \gg 1$, with r the radius of curvature in m. Thus, the curvature needs to be smooth and the frequency high enough for creep to occur [95]. This is the first condition for creep to be observed by a receiver.

The second condition is that t_{curve} should be large enough for creeping rays to form. When an incident ray gets close to the surface, there is a region where it transitions into a creeping ray called the Fock region, shown in Figure 4.3. The width of this region σ is in the order of $\mathcal{O}(k^{-1/3})$ and obtained through

$$\sigma = \left(\frac{kr}{2}\right)^{1/3} \frac{s}{r} \tag{4.18}$$

with s the arc length of the domain and r the radius, both in m [95, 96]. Equation 4.18 shows that a creeping wave only forms after traveling a minimum distance s along the surface. Thus for creep to be observed

$$t_{curve} \geq s. \tag{4.19}$$

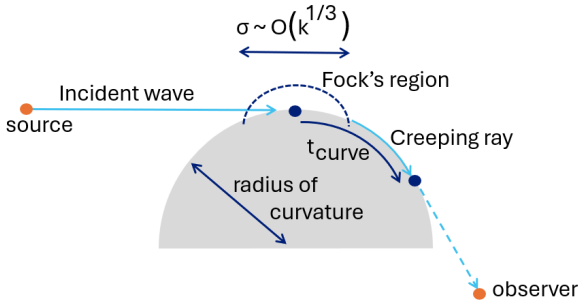

Figure 4.3: Schematic of formation of creeping waves going from source to observer including Fock's region

Equation 4.18 is rewritten to obtain the arc length s of the Fock region

$$s = \sigma r \left(\frac{kr}{2}\right)^{-1/3}. \tag{4.20}$$

Since σ can only be predicted through a series of wave equations requiring a large computational domain, it was assumed that

$$\sigma = k^{-1/3}.$$

resulting in the minimal distance for s of

$$s = 2^{1/3} \left(\frac{r}{k}\right)^{2/3}. \tag{4.21}$$

When both conditions are met, the diffracted pressure field can be calculated with

$$p_d = p_i e^{ikr} \sqrt{\frac{r_p}{r(r_p + r)}} \sum_m D_m^2(k, a_c) e^{-t_c \alpha_m} e^{ikt_c} \tag{4.22}$$

where a_c is the local radius of curvature. Diffraction coefficient D_m and decay coefficient α_m are given in Equation 4.23 and Equation 4.24, respectively [51].

$$D_m^2(k, a_c) = \frac{e^{i\pi/12} a_c^{1/2}}{2^{5/6} \pi^{1/2} (k a_c)^{1/6} Ai(-q_m)^2} \tag{4.23}$$

$$\alpha_m = \frac{1}{a_c} \left(\frac{k a_c}{2}\right)^{1/3} q_m e^{-i(\pi/6)} \tag{4.24}$$

Both depend on the Airy function Ai with solutions q_m. It predicts a fast decay in wave strength for creeping waves [97].

4.2. Model

A model implementing this theory has been created in an earlier project for observers on the ground [51]. This model has been adapted to reduce computational costs. Instead of ground observers, a lower hemisphere encompassing the aircraft - noise source(s) system was created with observers or vertices spaced along the hemisphere surface. A simple graphic of the set up is shown in Figure 4.4. The system is assumed to be stationary, the hemisphere itself moves along with the aircraft. The aircraft itself is laterally centered with the noise source, being the highest point of the aircraft for the REBEL-C, at the $z = 0$ plane. It is set up in such a way that only one engine needs to be analyzed, assuming the results for the other engine can be mirrored due to symmetrical geometry. No interference between the two engine noise sources is assumed. The basic set up includes one stationary monopole noise source representing the right engine.

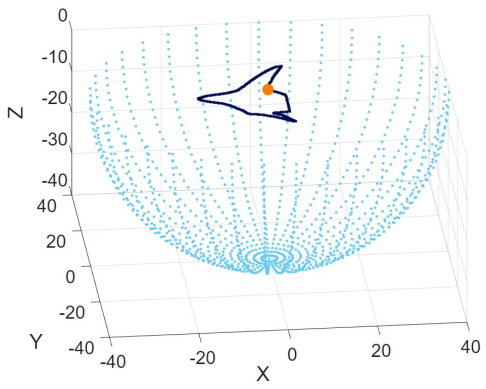

Figure 4.4: Set up of the shielding analysis with the noise source in orange, outline of the BWB in dark blue and observer locations on the hemisphere of radius r = 40 m in light blue. The number of vertices u along the radius is 36.

The hemisphere was created using the method described by Yunus et al. [98], consisting of $(u + 1)^2$ vertices or observers, with u indicating the number of segments along radius r. A radius of 40 m was chosen such that the observers are far enough away from the shielding body to get accurate data while being close enough to reduce computational expenses. Furthermore, [98] presented reasonable results for a distance between vertices of 2λ. This indicates that the minimum number of u for the highest 1/3-octave frequency band, 10 kHz, is close to 3700. Due to computational constraints of Matlab this is not feasible for the full hemisphere and therefore the maximum for the first analysis was set at u = 180. The received noise for observers on the ground is then found through propagation from the hemisphere using the same angles.

4.2.1. Validation

In [51] the model for edge-diffracted rays was compared to Boundary Element Method (BEM) and ray-tracing models from [91] and good agreement was found. To ensure proper working of the hemisphere model, its results were compared to those of Vieira [51]. Both set ups are shown in Figure 4.5a [51] and Figure 4.5b for a stationary monopole noise source above a disk. The results are displayed in Figure 4.6a and Figure 4.6b, showing very similar attenuation. The differences might be explained through sensitivity of the colorbar and its stepsize.

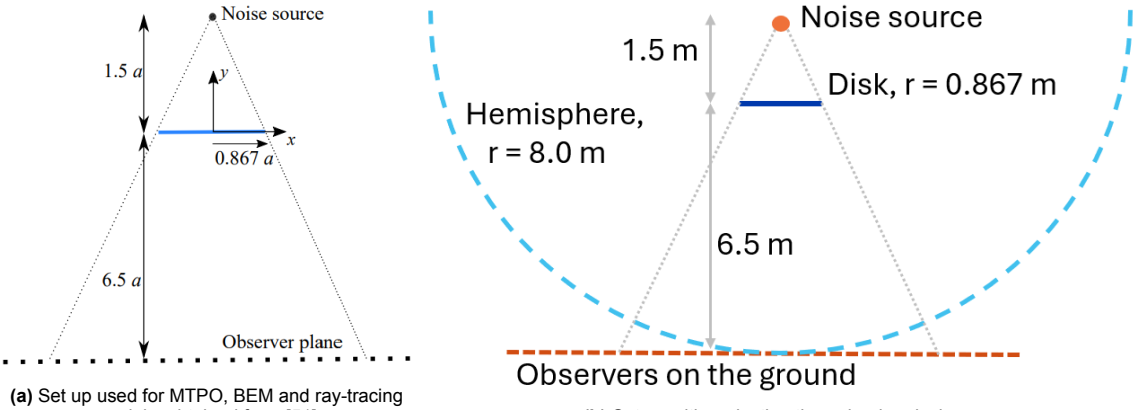

(a) Set up used for MTPO, BEM and ray-tracing models, obtained from [51]

(b) Set up with projection through a hemisphere

Figure 4.5: Set up of a monopole noise source above a stationary disk

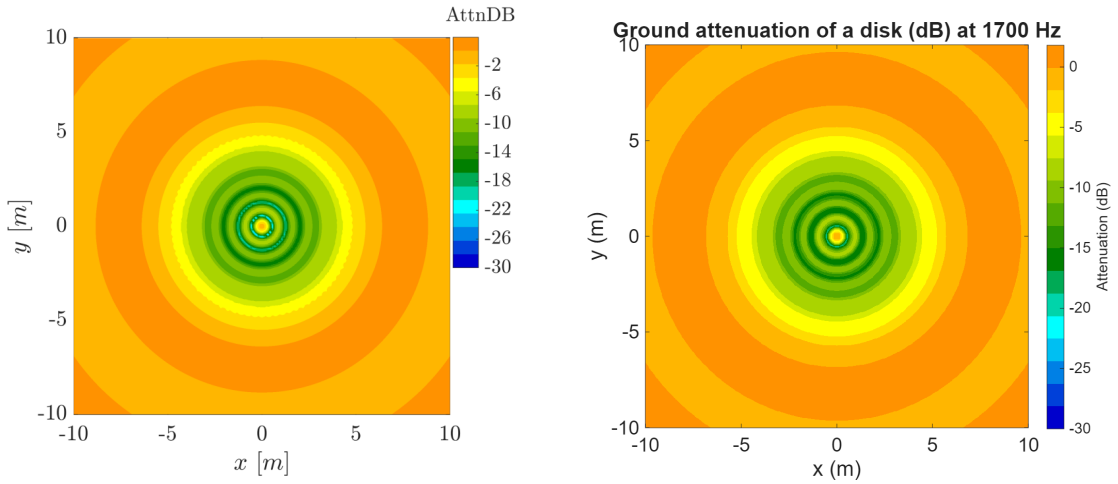

(a) Attenuation on the ground, obtained from Vieira [51]

(b) Attenuation on the ground through projection of a hemisphere

Figure 4.6: Comparison of attenuation for different geometrical modeling methods for a disk

Although the model developed by Vieira contained an option to include creeping rays, this part of the model was not yet verified. This was done by comparing the results with those of [91] for a sphere instead of a disk in the same type of set-up as before. All results are shown in Figure 4.7 [91]. Looking at these, there are some small differences, yet the plots look quite similar. This suggests the implementation of creep works.

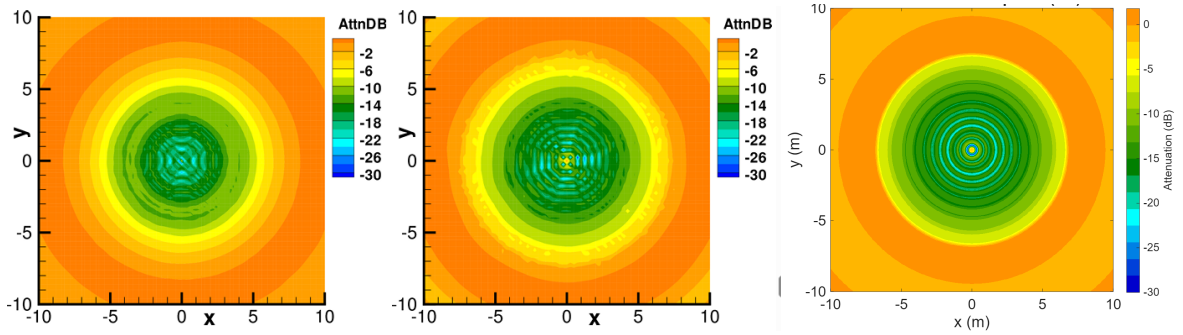

(a) Attenuation on the ground using BEM (left) and a ray-tracing approach (right), obtained from [91]

(b) Attenuation on the ground through projection of a hemisphere

Figure 4.7: Comparison of attenuation from different modeling methods for a sphere at 3400 Hz

4.2.2. Outline

With the program validated, the focus transitioned to the analysis of the REBEL-C and its shielding capabilities. An important factor in determining the attenuation is the geometry of the shielding object. The geometry input depends on the outline of the aircraft as seen from the noise source. The outline is defined as the location on the geometry where direct rays from a noise source just graze the surface or hit an edge, as shown in Figure 4.8. To include creep in the analysis at each point on the outline the type of edge must be specified as sharp of curved. If curved, the radius of curvature is required as well. To ensure the full shape is captured, a large number of data points needs to be taken. It was shown in [51] that segments of 0.2 m length suffice. In order to obtain this level of segmentation, the REBEL-C model provided by the University of Roma Tre [11] was dissected in SolidEdge for each 5° angle from the engine noise source point of view as schematically shown in Figure 4.8. Extra measurements were done at particular locations, such at the wing tips body-wing connection and fuselage trailing edge corners. More, smaller segments were then generated through interpolation. This was all done for the right-side engine only. It was assumed that the left engine would not shield the noise from the right engine due to diffraction around the left engine itself. To simplify the analysis only the airframe itself was considered.

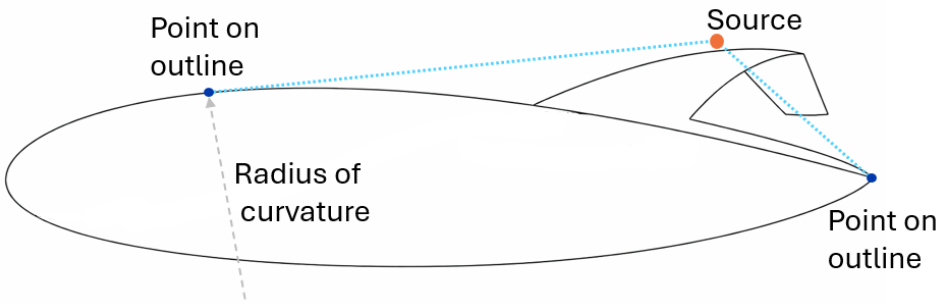

Figure 4.8: Schematic of determining points on the outline through a cut section of the BWB

After obtaining the source location and the corresponding outline, the attenuation can be computed for each frequency and the results processed following the flowchart shown in Figure 4.9.

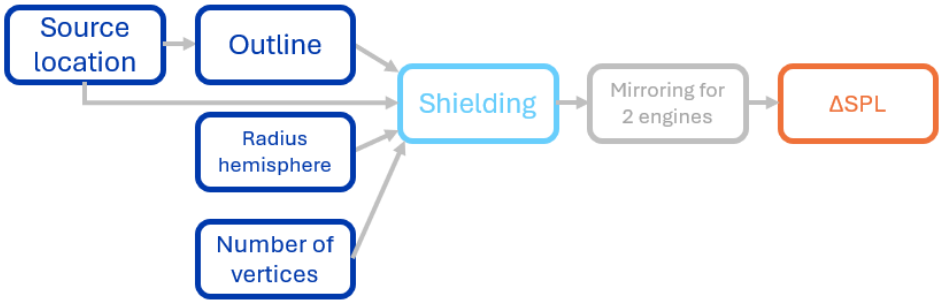

Figure 4.9: Flowchart showing the steps taken to obtain the attenuation due to shielding

Frequency

When analyzing the first results, it was found that more noise shielding occurs at higher frequencies due to the higher wavenumber. Each higher 1/3 octave center frequency band shows more attenuation than the one preceding it. To demonstrate the results, two center band frequency haven been chosen to represent the engine noise spectrum. Jet and combustor noise are represented for a low frequency of 400 Hz and fan noise is represented for a high frequency of 5 kHz. The results are displayed in Figure 4.10a and Figure 4.10b, and show more attenuation for the higher frequency.

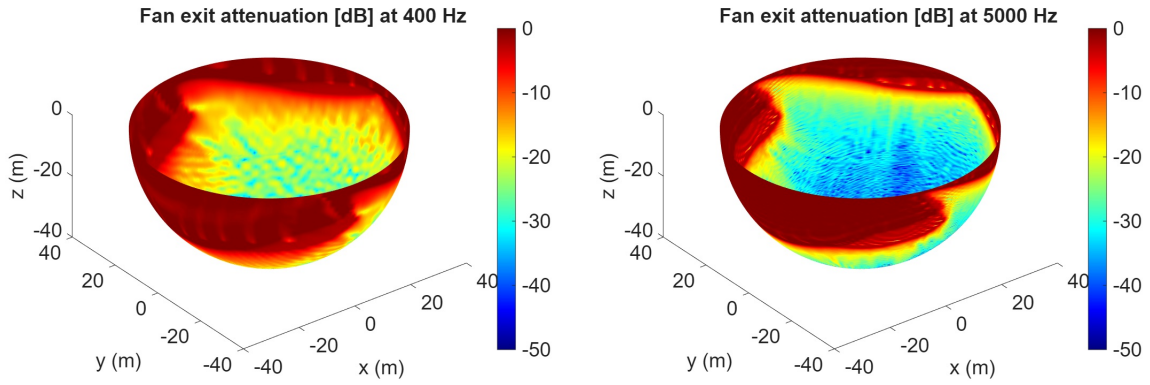

(a) Attenuation due to noise shielding at 400 Hz for u = 180

(b) Attenuation due to noise shielding at 5 kHz for u = 180

Figure 4.10: Fan exit noise reduction due to shielding on the hemisphere

Creep

To grasp the effect of including creeping rays in the computations for the high radius of curvatures expected for the BWB, a comparison was made between one outline including the radius of curvature and one outline where only sharp edges were considered. The results are shown for the same two frequencies, 400 Hz and 5 kHz. At low frequencies, the small wavenumbers result in less creep as shown in subsection 4.1.3. This is represented in Figure 4.11a, where the differences are mostly within 1.5 dB, most often even within 0.5 dB. The differences are more pronounced although still mostly within 2 dB for high frequencies, as shown in Figure 4.11b. Most differences can be observed towards the front of the aircraft, where the fuselage with the most curvature is located. Furthermore, the current number of vertices, u = 180, is not enough to show all the details for higher frequencies, which affects the results at 5 kHz as well. Due to the fast decaying behavior of the Airy functions as defined in subsection 4.1.3, the effect of creep is quite small. Only below the leading edges of the aircraft creep occurs, where $kr > 1$ and the arc length t_{curve} is large enough. It can therefore be argued that only including edge-diffracted rays in the analysis can give reasonable results if multiple cases have to be compared. Including creep was found to be much more computationally expensive and increases the run time by a factor 8-10. For u = 180, this increase was from 60 minutes for edge-diffraction only to 9.5 hours for an outline including curvature.

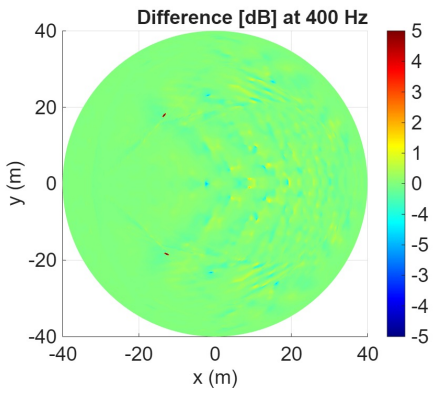

(a) Difference in attenuation due to noise shielding excluding and including creep at 400 Hz

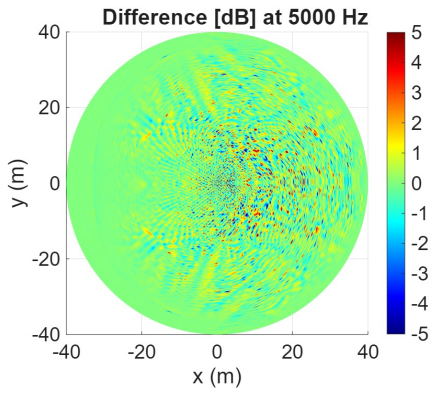

(b) Difference in attenuation due to noise shielding excluding and including creep at 5 kHz

Figure 4.11: Top view of hemisphere showing shielding difference for the two diffraction types. Negative results indicate more shielding when creep is included

4.2.3. Noise source location

Using multiple engine sources for each component was considered following the same methodology as done for BOLT [30]. Three major sources were researched:

- The inlet fan noise located at the front of the turbofan, measured at x = 20.8 m from the origin at the aircraft nose;
- The aft fan noise is set at the bypass exhaust exit, at 2/3 of the engine length for x = 22.8 m;
- The core and jet noise source is located at the core exhaust exit, x = 23.8 m.

The y and z location for all three sources was set to 2.4 m and 2.8 m from the center line, respectively. All these coordinates were obtained using a representative high BPR engine sized for the REBEL-C of 3 m in length used in [99]. Although directivity of these noise sources should be considered, all were modeled with monopole noise sources due to limited availability of source types. The model only contains options to model monopole, dipole and multi-sources. This likely affects the results and should be taking into consideration. A benefit of this methodology is however that the analysis can be done once per source location, instead of evaluating for each thrust setting separately.

After analyzing the outlines for all three engine components, it was found that the outline for each noise source is very similar. The attenuation results are however vastly different. For the jet, more shielding would be expected in front and less shielding in the back due to the more aft location. For the fan inlet the opposite would be expected due to the more forward location, however it turns out that this is not true, as shown in Figure 4.12. The jet noise is actually shielded less towards the front, possibly due to proximity to the trailing edge and the edge-diffraction around it. Similar results were obtained by DLR and ONERA for BOLT [30].

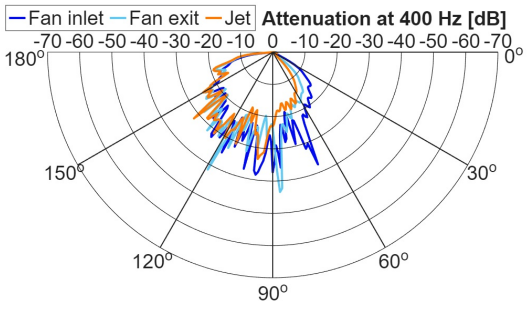

(a) Attenuation due to noise shielding at 400 Hz, u = 180

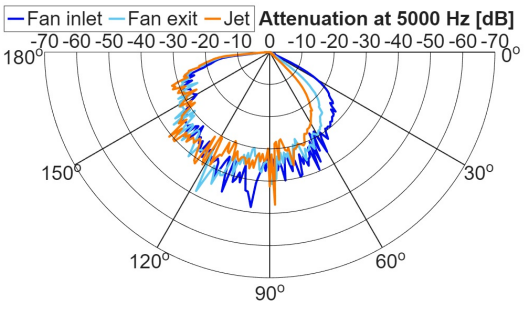

(b) Attenuation due to noise shielding at 5 kHz, u = 180

Figure 4.12: Polar plots showing a noise reduction due to noise source location for ϕ = 0°

4.2.4. Number of observers

The effect of the number of vertices was analyzed using three inputs, u = 180, u = 36 and u = 2880 as done in [98]. The latter is analyzed for ϕ = 0° only due to computational restraints. It can therefore only be used for overhead flight. It does however comply with being within the 2λ constraint set in [98] and will therefore be used in analysis where only straight flight going directly overhead is considered. The differences between u = 36 and u = 180 can be seen in Figure 4.13, here showing the noise reduction at 5 kHz for the fan exit. The details clearly get lost for the coarser grid, however the computational time does decrease by a factor 9 to around 1 hour. The same effect was viewed for all other frequencies.

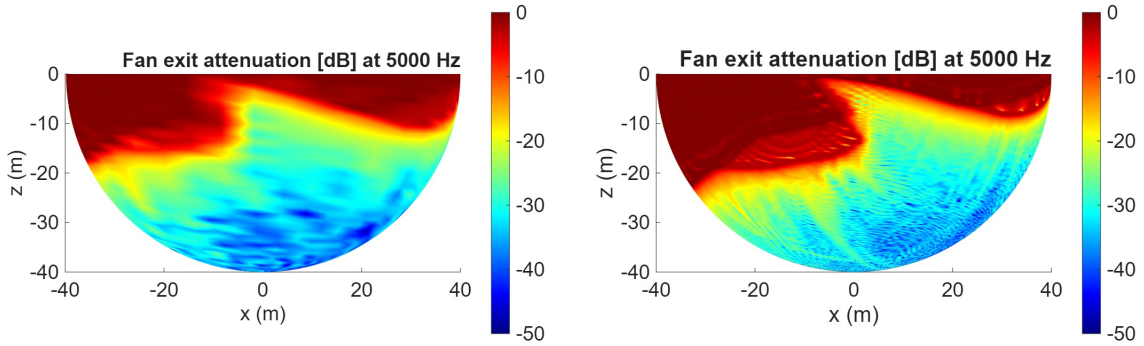

(a) Attenuation due to noise shielding at 5 kHz for u = 36

(b) Attenuation due to noise shielding at 5 kHz for u = 180

Figure 4.13: Side view of the hemisphere showing fan exit noise reduction due to shielding for different number of vertices

In Figure 4.14 the attenuation at ϕ = 0° is shown and compared. It shows that increasing the number of vertices shows even more fluctuations in noise reduction. The largest peaks show much higher attenuation. This might affect an analysis if instantaneous measurements are taken instead of continuous one. The same effect was found for all other frequencies.

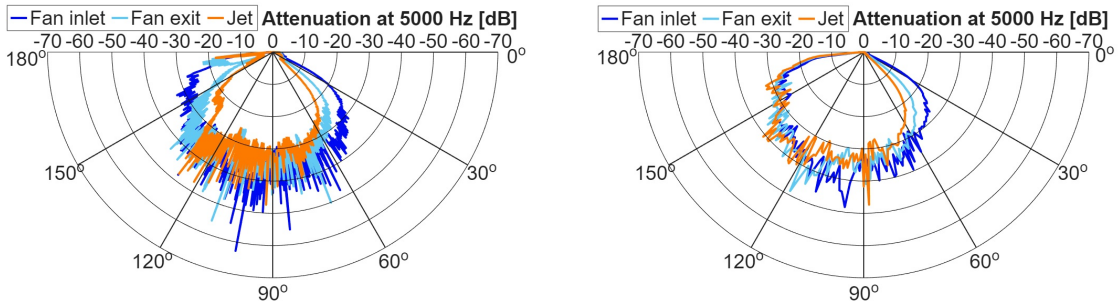

(a) Attenuation due to noise shielding at 5 kHz for u = 2880

(b) Attenuation due to noise shielding at 5 kHz for u = 180

Figure 4.14: Polar plot showing fan exit noise reduction due to shielding for different number of vertices for ϕ = 0°

4.2.5. $\triangle$SPL tables

Results of noise reduction were obtained for each of the three noise sources and each of the 24 1/3-octave frequency bands for u = 180 and u = 2880. These were then translated into $\triangle$SPL tables, with the noise reduction given for each polar and azimuthal angle per frequency. These tables have been implemented into SOPRANO.

5. Noise-Power-Distance Tables Methodology

Noise-Power-Distance (NPD) tables are generated using flyover measurements corrected to straight flight at 160 kt [42] with atmospheric conditions having to fall within specified constraints. These measurements are then used to compute the noise metrics at 10 slant distances: 200, 400, 630, 1000, 2000, 4000, 6300, 10,000, 16,000 and 25,000 ft [5]. This chapter describes the conditions under which these measurements are performed, the set-up used to compute the NPD tables using semi-empirical models and a comparison of the ANP database with results obtained using SOPRANO.

5.1. Framework

During noise certification flyover measurements are recorded. These data sets are often used to generate NPD tables [15]. In order to generate these tables, the preferred conditions according to SAE AIR1845A [42] are

- Straight flight between 100 and 800 m altitude;
- Reference ambient conditions inside the acceptable envelope;
- Wind speeds of less than 8 m/s;
- Constant aircraft configuration [42].

The measured data is corrected to an airspeed of 160 kt for a maximum takeoff weight (MTOW) of 85% and a maximum landing weight (MLW) of 90%. For the measurement set up, the requirements set in [42] are

- Measurements are done directly underneath the flight path on a flat terrain with no obstructions;
- Noise is recorded at 0.5 s intervals for 1/3-octave band center frequencies of 50 Hz to 10 kHz.

While some research into NPD tables for novel aircraft designs have used adaptions and delta's to known noise metrics of reference aircraft [100], a fully semi-empirical model based approach is used here where calculations are used instead of measurements. In the set-up that has been used, the flyover is done at 1,000 ft altitude as is recommended in SAE AIR1845A [42], with level flight at 160 kt. Engine parameters are obtained using GSP for the actual thrust at 1000 ft altitude. The engine and airframe modules as shown in chapter 3 are used. The flyover starts at -60 s before flying overhead and continues until +60 s after, with SPL data for each aircraft component calculated at 0.5 s intervals in SOPRANO for each of the 24 1/3-octave band center frequencies. The microphone height is set to 1.2 m and it is assumed there are no ground reflections. No wind is modeled and the ambient conditions at 1000 ft are obtained assuming ideal gas for a standard atmosphere. The set-up is shown in Figure 5.1.

For measurements, the data needs to be corrected to a reference flight path and then the attenuation needs to be corrected to an average attenuation. The latter is done using table B1 of [42]. For the flyovers produced with SOPRANO, the SPL data is predicted for reference conditions. Since it takes only spherical spreading and the average attenuation into account, the data does not need to be corrected. Furthermore, the component based results from SOPRANO simplify the analysis of dominant components. The SPL data SPL_{fo} is propagated to the other slant distances for each frequency ($SPL_{mic}(f, d)$ using Equation 5.1. Here, slant distance d is given in m, while d_{fo} describes the shortest

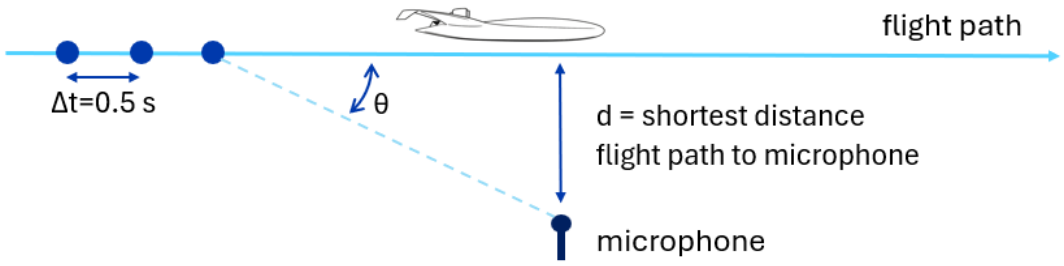

Figure 5.1: flyover set up for NPD calculations assuming level flight at 1000 ft altitude directly over the microphone

flyover to microphone distance of the calculations in SOPRANO. Polar angle θ and average attenuation per frequency α should be taken into account [42]. Note that the spherical spreading in Equation 5.1 uses the shortest flight path to microphone distance, while the atmospheric attenuation does include the actual flight path length using the polar angle. This is done in SAE AIR1845A under the assumption that $L_{A_{max}}$ is found at a constant polar angle $\theta_{L_{A_{max}}}$ [42]. Since level flight is assumed, the slant distances d correspond to the aircraft altitude.

$$SPL_{mic}(f,d) = SPL_{fo}(f) - 20\log\left(\frac{d}{d_{fo}}\right) - \alpha(f)\frac{d-d_{fo}}{\sin\theta} \tag{5.1}$$

The A-weighted sound level L_A is then found using Equation 2.5, summing the results over the whole 1/3-octave frequency range for each calculated point. For slant distances up to 800 m, the SEL is computed using a segmented version of Equation 2.9, given as

$$SEL_{d\leq 800} = 10\log\left[\frac{1}{T_0}\sum_{i=1}^{n}\left(10^{L_A(t_i)/10}\Delta t_i\right)\right] \tag{5.2}$$

where T_0 = 1 s and $L_A(t_i)$ includes all L_A within a 10 dBA downtime of $L_{A_{max}}$. Time interval Δt_i between two consecutive points is 0.5 s for 1000 ft and found for the other slant distances using

$$\Delta t_i = \frac{d}{d_{fo}}\Delta t_{i_{fo}}. \tag{5.3}$$

For slant distances greater than 800 m, a slightly simplified approach is used [42]. First, the SPL results at 800 m should be computed with Equation 5.1. These are used instead of SPL_{fo} to obtain the sound pressure levels at further distances using the same equation. After computing L_A and SEL for 800 m, the SEL is calculated with

$$SEL_{d>800} = SEL_{d=800} + \left(L_{A_{max}} - L_{A_{max,d=800}}\right) + \Delta D \tag{5.4}$$

where effective duration ΔD is found using

$$\Delta D = 7.5\log\left(\frac{d}{800}\right). \tag{5.5}$$

The PNLT is computed as shown in Equation 2.8. The computation of EPNL, given in Equation 5.6, uses the same methodology for slant distances up to 800 m and over as for SEL [101].

$$EPNL = \begin{cases} 10\log\left[\frac{1}{T_0}\sum_{i=1}^{n}\left(10^{PNLT(t_i)/10}\Delta t_i\right)\right], & \text{d } \leq \text{ 800 m} \\ EPNL_{d=800} + (PNLT_{max} - PNLT_{max,d=800}) + \Delta D, & \text{d > 800 m} \end{cases} \tag{5.6}$$

where T_0 is now 10 s and all values of PNLT are included that are within a 10 TPNdB downtime of $PNLT_{max}$. ΔD is computed using Equation 5.5. A flowchart of the whole process is shown in Figure 5.2.

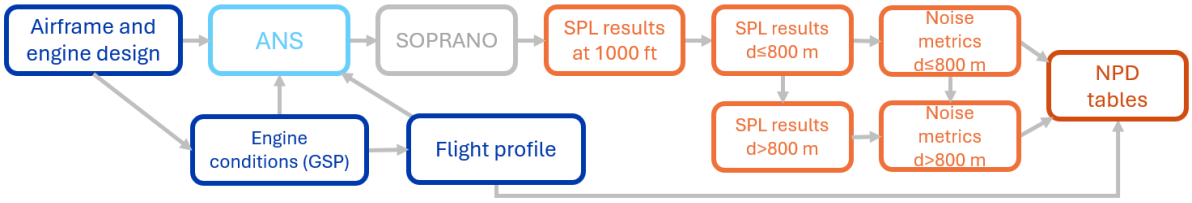

Figure 5.2: Flowchart for obtaining NPD tables

5.2. Method verification

To verify the set up as described above works, a verification is first done for the A320 using the ANP database [65]. The inputs for SOPRANO are taken from GSP, Table 2.1 and the flyover study from [33]. An overview of these inputs is given in Table 5.1a and Table 5.1b. Although noise reduction technologies like fan liners could be implemented into SOPRANO, this has to be analyzed first for each thrust setting separately before being generated into a ΔSPL table and imported into SOPRANO. It is therefore omitted here. Likewise, engine noise reflection by the wing and other installation effects are neglected. The net-corrected power settings given in the NPD tables from the ANP database [65] are used to obtain noise data. These power settings are given as thrust corrected for the ambient pressure (F_N/δ in lbf) where pressure ratio δ is

$$\delta = \frac{P_0}{P_{ISA}} \tag{5.7}$$

with P_0 the ambient air pressure and P_{ISA} the ISA pressure of 101325 Pa. This pressure ratio can be obtained through the ideal gas assumption for a standard atmosphere given in Equation 5.8 [102].

$$\frac{P_0}{P_{ISA}} = \left[1 + \frac{\lambda_T(H_0 - H_{ISA})}{T_{ISA}}\right]^{-\frac{g_0}{R\gamma_T}} \tag{5.8}$$

where λ_T is the temperature gradient of -0.0065 K/m, H_0 is 304.8 m (1000 ft), H_{ISA} is the sea level altitude of 0 m, T_{ISA} is 288.15 K, g_0 is the gravitational acceleration of 9.08665 m/s^2 and R is the gas constant of air at 287.05 J/(kg K).

Table 5.1: Inputs used in ANS

(a) A320 airframe inputs

Parameter	Value
Wing span [m]	34.1
Wing surface area [m^2]	122.6
Flap span [m]	26.59
Flap surface area [m^2]	21.1
Main wheel diameter [m]	1.143
Nose wheel diameter [m]	0.762
Main strut length [m]	3.45
Nose strut length [m]	1.957
Number of wheels per strut [-]	2
Number of main struts [-]	2
Number of nose struts [-]	1

(b) CFM56-5B4 engine inputs

Parameter	Value
Fan diameter [m]	1.735
Number of blades [-]	36
Number of vanes [-]	106
RSS [-]	300
$M_{tr_{des}}$ [-]	1.43
$\Delta T_{des_{turb}}$ [K]	660.3
A_{core} [m^2]	0.251
A_{bypass} [m^2]	0.852
L_{core} [m]	1.0

5.2.1. Flyover

The resulting L_A for a full flyover is shown for two cases in Figure 5.3. The first one is for 22500 lbf net-corrected thrust for departure. The slats and single-slotted flaps are both deployed, with the flap deflection angle at 10° following the default departure procedure in the ANP database [65]. When the aircraft is approaching the observer position, both engine and airframe noise components are present. $L_{A_{max}}$ is dominated by engine noise components, which continue to dominate after passing overhead.

A different picture is seen during approach, shown for 2700 lbf net-corrected thrust. In this case, the landing gear, slats and flaps are deployed. The flap deflection angle is set to 35°. Looking at Figure 5.3,

the airframe noise is dominant when the aircraft is approaching the observer. The airframe noise is raised compared to departure due to the presence of the landing gear and a higher flap deflection angle. Engine noise does become present close to the overhead position and decays quickly after the aircraft flies further. The lower engine power settings causes a lower $L_{A_{max}}$. All noise sources are shown separately in Figure D.1 in Appendix D.

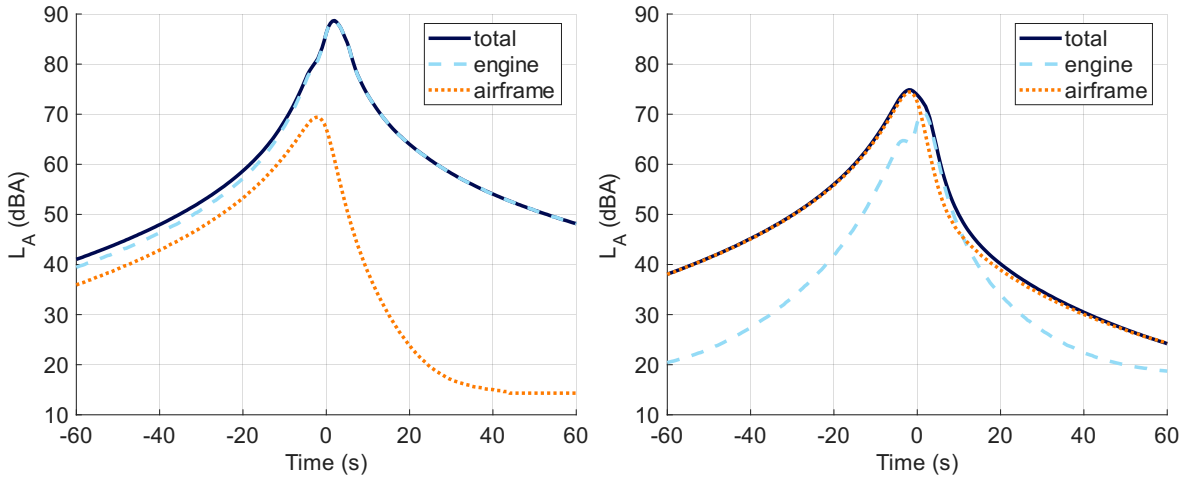

(a) Departure, F_N/δ = 22500 lbf

(b) Approach, F_N/δ = 2700 lbf

Figure 5.3: Flyover results for an A320 using power settings from the ANP database

5.2.2. Comparison A320

Figure 5.4 and Figure 5.5 show the $L_{A_{max}}$ results from all the power settings given in the ANP database. Overall the results are quite close for both analyzed aircraft flight phases. The SEL plots, which are created using L_A with Equation 5.2 and Equation 5.4, follow a similar shape. They can be found in Appendix C.

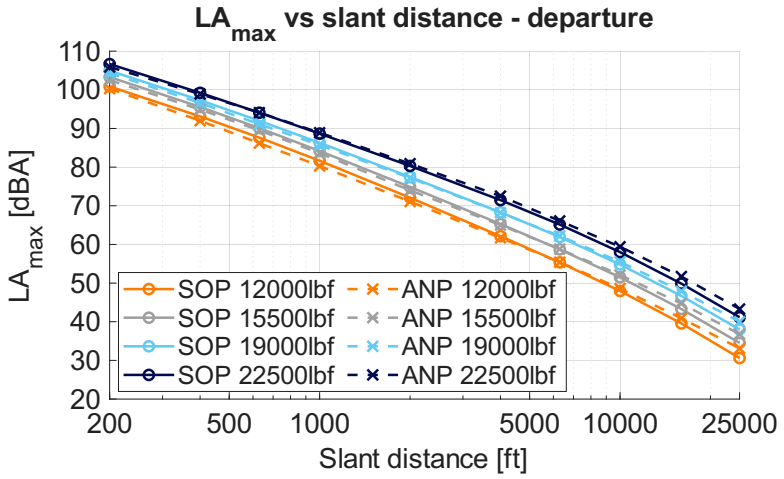

Figure 5.4: NPD LA_{max} for a departing A320 at various power settings for SOPRANO (SOP) and the ANP database

For the $PNLT_{max}$, the differences are slightly larger during departure, as shown in Figure 5.6. The $PNLT_{max}$ is consistently underpredicted for slant distances up to 6300 ft, after which the noise gets overpredicted for 10,000 and 16,000 ft. This is probably due to the tone corrections applied. Figure B.1 and Figure B.4 indicate that measurements likely will show more tonal noise in general [33]. Furthermore, although the noise metrics are shown for a constant polar angles of $\theta_{L_{A_{max}}}$ and $\theta_{PNLT_{max}}$ according to the assumptions made [42], it was found that these angles are actually not constant. This presumably affects the results as well since the metrics calculated at 1000 ft dictate all the other metrics. Interestingly, the PNLT from the ANP database at 15500 lbf is lower than the 12000 lbf thrust setting

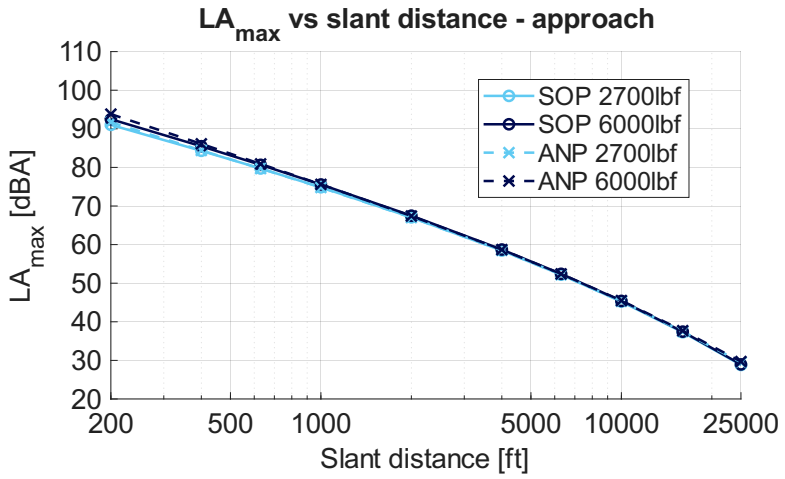

Figure 5.5: NPD LA$_{max}$ for an approaching A320 at various power settings for SOPRANO (SOP) and the ANP database

for the first two slant distances. The PNLT$_{max}$ figure for approach can be found in Appendix C. The EPNL plots follow a similar shape as the PNLT$_{max}$ plots and are shown in Appendix C as well.

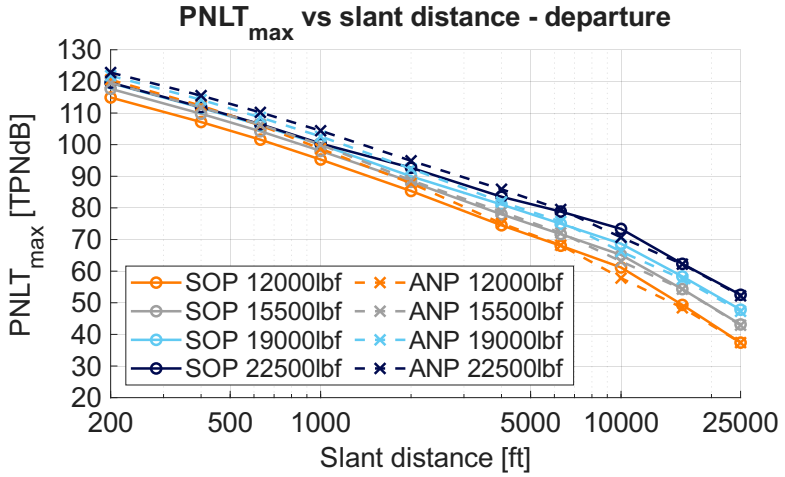

Figure 5.6: NPD PNLT$_{max}$ results for a departing A320 at various power settings for SOPRANO (SOP) and the ANP database

All root mean square errors (RMSE) across all slant distances are shown in Table 5.2. For L$_{A_{max}}$, the results are very close. Slightly larger deviations up to 2.5 dBA are observed for SEL. Since SEL is computed from L_A over a duration, this is to be expected. More variation is found for PNLT$_{max}$, likely due to differences in tones in the SPL results. This tonal variation affects the EPNL deviation as well.

Table 5.2: Root mean square error between SOPRANO and the ANP database for an A320

Operation	Thrust [lbf]	L$_{A_{max}}$ [dBA]	SEL [dBA]	PNLT$_{max}$ [TPNdB]	EPNL [EPNdB]
Departure	12,000	1.2	2.3	3.3	2.0
	15,500	1.0	2.5	1.4	1.7
	19,000	0.9	2.4	2.0	2.3
	22,500	1.1	2.3	2.7	1.4
Approach	2,700	0.3	1.4	1.9	2.0
	6,000	0.5	0.7	2.4	1.4
All	-	0.9	2.0	2.4	1.8

5.2.3. Comparison Boeing 777

This analysis was repeated for the Boeing 777-200LR with GE90-115B turbofan engines. The same geometrical parameters and GSP engine model are used as in [33]. An overview of the inputs are given in Table 5.3a and Table 5.3b [103]. It is assumed that slats and the single and double slotted flaps are both extended [104]. The flap deflection angle for departure and approach were chosen to be 15° and 30°, respectively. For the approach, the landing gear is deployed.

Table 5.3: Inputs used in ANS

(a) Boeing 777 airframe inputs

Parameter	Value
Wing span [m]	73.6
Wing surface area [m^2]	623.5
Flap span [m]	55.8
Flap surface area [m^2]	43.8
Main and noise wheel diameter [m]	1.27
Main strut length [m]	4.73
Nose strut length [m]	2.90
Number of main wheels per strut [-]	6
Number of main struts [-]	2
Number of nose wheels [-]	2
Number of nose struts [-]	1

(b) GE90-115B engine inputs

Parameter	Value
Fan diameter [m]	3.25
Number of blades [-]	22
Number of vanes [-]	54
RSS [-]	300
$M_{tr_{des}}$ [-]	1.30
$\Delta T_{des_{turb}}$ [K]	769.0
A_{core} [m^2]	0.695
A_{bypass} [m^2]	3.664
L_{core} [m]	1.4

With these parameters and the engine conditions following from GSP for the actual thrust at 1000 ft altitude and an airspeed of 160 kt, the results from SOPRANO were processed into NPD tables. As Table 5.4 shows, the differences between the ANP data and the semi-empirical model are somewhat larger than for the A320. The larger aircraft and engines cause higher noise levels and more deviations can be expected because of this. During departure $L_{A_{max}}$ and SEL are overpredicted for the smaller slant distances for all thrust settings but the lowest one as shown in Figure 5.7. The engine noise dominates. The higher rate of decrease in $L_{A_{max}}$ and SEL from SOPRANO causes an underprediction for the two largest slant distances. For the approach, the differences are smaller. The flyover plots are shown in Appendix D. The presence of engine noise likely affects the PNLT and thus $PNLT_{max}$ and EPNL. The overall RMSE is within an acceptable range. All NPD figures can be found in Appendix C.

Table 5.4: Root mean square error between SOPRANO and the ANP database for a Boeing 777

Operation	Thrust [lbf]	$L_{A_{max}}$ [dBA]	SEL [dBA]	$PNLT_{max}$ [TPNdB]	EPNL [EPNdB]
Departure	31000	1.9	2.1	2.1	2.5
	41000	2.7	2.6	2.7	2.2
	51000	3.9	3.7	3.9	2.8
	61000	4.2	4.1	4.1	3.2
	71000	4.0	4.2	3.9	3.5
	81000	3.2	4.4	2.3	3.0
Approach	12000	1.7	1.5	3.2	2.3
	17000	1.2	1.5	2.7	2.3
	22000	1.2	1.5	2.5	2.1
	27000	1.4	1.7	2.7	2.4
All	-	2.8	3.0	3.1	2.7

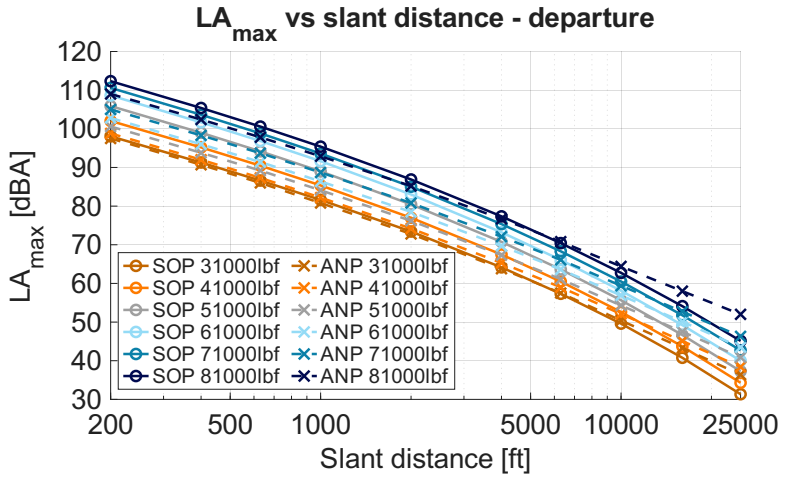

Figure 5.7: Comparison of NPD tables for $L_{A_{max}}$ during departure of a Boeing 777, from the ANP database and SOPRANO (SOP)

5.2.4. Comparison A330

The third aircraft that has been analyzed is an Airbus 330-301 with CF6-80E1 turbofan engines. The airframe and engine parameters are given in Table 5.5a and Table 5.5b [105, 106]. Both slats and single slotted flaps are deployed. The flap deflection angle for departure and approach were chosen to be 14° and 35°, respectively [107]. The landing gear is assumed to be down for the approach.

Table 5.5: Inputs used in ANS

(a) A330 airframe inputs

Parameter	Value
Wing span [m]	61.8
Wing surface area [m^2]	412.4
Flap span [m]	41.1
Flap surface area [m^2]	32.8
Main and noise wheel diameter [m]	1.33
Main strut length [m]	3.75
Nose strut length [m]	2.35
Number of main wheels per strut [-]	4
Number of main struts [-]	2
Number of nose wheels [-]	2
Number of nose struts [-]	1

(b) CF6-80E1 engine inputs

Parameter	Value
Fan diameter [m]	2.443
Number of blades [-]	34
Number of vanes [-]	60
RSS [-]	300
$M_{tr_{des}}$ [-]	1.44
$\Delta T_{des_{turb}}$ [K]	643.2
A_{core} [m^2]	0.370
A_{bypass} [m^2]	1.880
L_{core} [m]	1.1

After performing the same analysis, the RMSE as shown in Table 5.6 was found. The approach computed in SOPRANO is noticeably closer to the ANP database for $L_{A_{max}}$ and SEL than the departure. For 34000, 42000 and 52000 lbf the noise is overpredicted, while for 62000 lbf $L_{A_{max}}$ is underpredicted as shown in Figure 5.8. For the approach, the airframe and engine noise both dominate at 1000 ft altitude while for departure the engine noise is fully dominant. The flyovers are presented in Appendix D. The PNLT related RMSE are slightly larger, especially for departure. The differences in engine noise prediction is likely a combination of both the use of semi-empirical prediction methods and engine conditions obtained from GSP. All plots showing the NPD tables are given in Appendix C.

Table 5.6: Root mean square error between SOPRANO and the ANP database for an A330

Operation	Thrust [lbf]	$L_{A_{max}}$ [dBA]	SEL [dBA]	$PNLT_{max}$ [TPNdB]	EPNL [EPNdB]
Departure	34000	2.8	1.8	4.1	3.7
	42000	2.9	2.1	3.3	3.9
	52000	2.3	2.1	4.4	4.2
	62000	2.3	3.8	1.7	2.2
Approach	6000	0.5	1.1	1.8	2.0
	12000	0.8	0.6	2.6	1.7
All	-	2.2	2.2	3.2	3.1

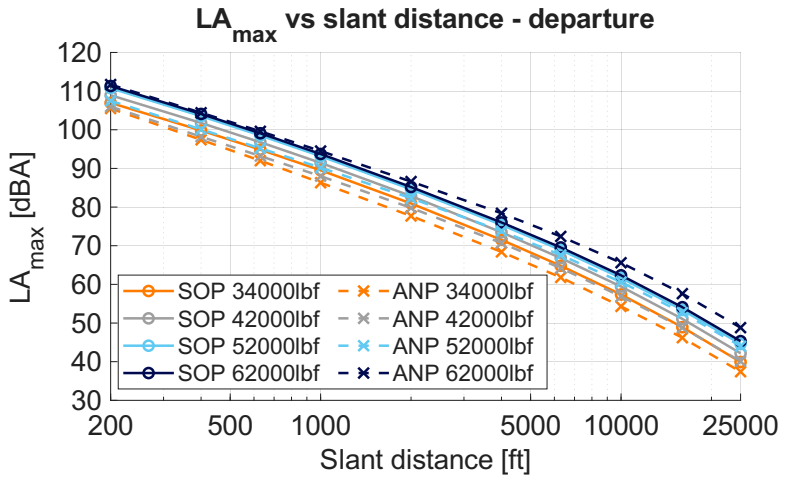

Figure 5.8: Comparison of NPD tables for $L_{A_{max}}$ during departure of an A330, from the ANP database and SOPRANO (SOP)

Overall, predicting the NPD tables using SOPRANO seems to give reasonable results. The airframe noise seems to be predicted well for TAW aircraft. The engine noise gives more deviations. This is possibly due to the turbofans modeled in GSP that give slightly different results, due to the defined parameters or the simulations themselves. Furthermore, the engine noise prediction using the conditions from GSP might make the differences more extreme. Moreover, measurement errors and corrections applied to the ANP data might cause deviations as well. The approach for all three cases shows an overprediction in $PNLT_{max}$ for the larger slant distances, likely due to a combination of using a constant angle $\theta_{PNLT_{max}}$ for $PNLT_{max}$ and the presence of tonal noise. For the largest slant distance, a sharp decrease in PNLT is shown resulting in levels similar to the ANP database for all but the departure of the Boeing 777.

6. Flight Profile

Representative power settings for departure and approach are necessary in order to generate NPD tables. The flight profile of the reference aircraft Airbus A320-214 has been analyzed for both departure and arrival following the method as described in ECAC Doc. 29 [5]. This method has been used to obtain flight performance data for Schiphol Airport [108]. Flight data for an A320-211 has been used due to unavailability of A320-214 data. Since the flight profile of the REEL-C is unknown, the same flight path is assumed for both the A320 and REBEL-C. The thrust for the BWB is computed assuming equal T/W ratios for both aircraft.

6.1. Flight path

Depending on the type of Noise Abatement Departure Procedure (NADP), aircraft accelerate and climb at different rates. It was found that NADP2 is the most commonly used at Schiphol Airport [109]. This procedures aims to reduce fuel consumption and produce less noise around a larger area. In contrast, the goal of NADP1 is to reduce noise closer by airports, in turn increasing the total area affected by aircraft noise [110]. There are three different NADP2 profiles which reduce thrust at 800, 1000 or 1500 ft. The NADP2-1500ft profile is most often used and therefore chosen for this analysis [111]. ECAC Doc. 29 dictates that the range of aircraft can be determined with a stage length, where stage length 1 indicates a range of 0 to 500 nmi, stage length 2 a range of 500 to 1000 nmi, etc [5]. For varying stage lengths different amounts of fuel need to be taken on board, changing the takeoff weight. This influences the climb angle, airspeed and thrust at the departure. For the A320, stage length 2 will be used since this includes the range of 900 nmi.

During departure, the landing gear gets retracted moments after lift-off when a positive climb rate has been established [112]. It is assumed that the reference aircraft will take off with both slats and flaps extended to 20° and 10°, respectively [113]. These HLD's retract fully during the thrust cutback sequence at 1500 ft altitude. The full flight path is shown in Figure 6.1a.

An approach at Schiphol Airport can be done in several ways. The first method is by a one or two step descent where an aircraft levels off to reduce speed. A second option is to use a continuous descent approach (CDA). Leveling off at 2000 ft altitude to reduce airspeed is most commonly used at Schiphol Airport during the day [111], after which the aircraft descents at a steady 3° glide slope. When ILS is used, the landing gear gets deployed below 2000 ft. The setting for landing flaps is selected after passing 1200 ft [114]. If the flaps get fully deflected, the deflection angle is 35° while the slats get extended to 22° [113]. The full flight path for both aircraft including airspeed at arrival is shown in Figure 6.1b.

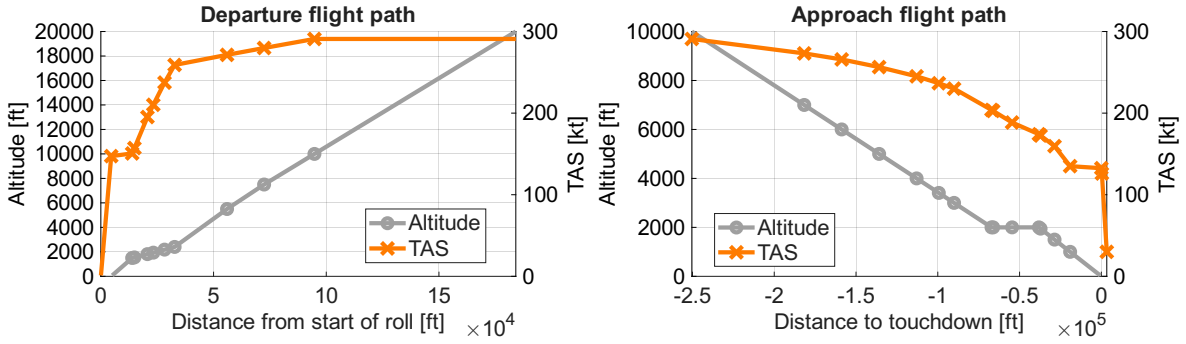

(a) Flight path at departure following NADP2, retracting flaps at 1500 ft

(b) Flight path at arrival including leveling of at 2000 ft

Figure 6.1: ANP flight paths at Schiphol Airport

6.2. Weight estimation

Before the flight profile of the BWB can be determined, a number of assumptions and calculations have to be made. The flight path is assumed to be the same for easy comparison, for a range of 900 nmi, with equal T/W ratios. For the A320, this means a takeoff weight (TOW) of 619.2 kN for stage length 2, while the MLW is 632.5 kN [65]. This is higher than the TOW since the A320 has lower fuel requirements for the range that is used here. To obtain the thrust at each point in the flight for the BWB, the maximum takeoff weight MTOW and MLW are computed first. This is done by a class I weight estimation method, based on Roskam [115] with adaptations from Vos et al. [116]. Although primarily designed for TAW aircraft, it is assumed that the same methodology can be applied for the REBEL-C. This method requires all segments in the mission profile to be known. The simplified mission profile for a regional aircraft that is used for this weight estimation is shown in Figure 6.2, with all segments defined in Table 6.1. It includes a possible diversion to another airport at a maximum range of 250 nmi.

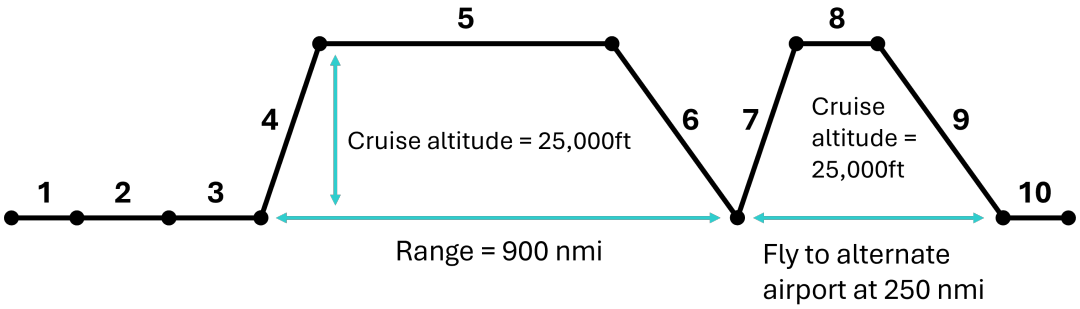

Figure 6.2: Schematic mission profile of the REBEL-C

The takeoff weight W_{TO} is a combination of three subweights; the operational empty weight W_{OE}, payload weight W_{PL} and fuel weight W_F. It is found by using

$$W_{TO} = W_{OE} + W_{PL} + W_F \tag{6.1}$$

where all weights are in N. These three weights are all computed with some form of

$$W = xW_{TO} + y \tag{6.2}$$

where W_{OE} is found with

$$\begin{aligned} W_{OE} &= W_E + W_{tfo} + W_{crew} \\ &= 0.4899W_{TO} + 30509 + M_{tfo}W_{TO} + 5m_{pax}g_0 \\ &= (0.4899 + M_{tfo})W_{TO} + 30509 + 5m_{pax}g_0. \end{aligned} \tag{6.3}$$

Here, W_E is the empty weight regression found from TAW transport jet statistics, W_{tfo} is the left over fuel vapor weight for empty fuel tanks as the fraction $M_{tfo} = 0.001$ of W_{TO} and W_{crew} is the crew weight [116]. There are five crew members on board [11]. The mass of one crew member or passenger m_{pax} includes luggage and is assumed to be 100 kg. Finally, g_0 is the gravitational acceleration of 9.80665 m/s^2. The payload weight becomes

$$W_{PL} = 100g_0m_{pax} \tag{6.4}$$

for 100 passengers. Fuel burn reduces the weight of an aircraft during each segment of the flight. The ratio of aircraft weight at the end of each segment over the start weight can be defined as a weight fraction. Multiplying all weight fractions gives a ratio of aircraft weight at the end of the mission to the initial weight [117]. The difference is the fuel weight, which is computed using fuel weight fraction M_{ff} as shown in Equation 6.5. The weight fractions fractions W_{i+1}/W_i are given in Table 6.1. The fractions are taken from empirical transport jet data [116], while both cruise fuel fractions are computed using the Breguet range equation given in Equation 6.6 [115]. The second cruise is calculated to obtain the amount of fuel reserves required in case an alternate airport has to be reached 250 nmi away for a

regional aircraft [116].

$$\begin{aligned} W_F &= M_{used} W_{TO} \\ &= (1 - M_{ff}) W_{TO} \\ &= \left(1 - \frac{W_1}{W_{TO}} \prod_{i=1}^{i=10} \frac{W_{i+1}}{W_i}\right) W_{TO} \end{aligned} \tag{6.5}$$

Table 6.1: Weight fractions for each flight section for fuel weight calculations

Segment	Segment type	Weight fraction [-]
1	Engine start and warm-up	0.99
2	Taxi	0.99
3	Takeoff	0.995
4	Climb according to NADP2-1500ft	0.98
5	Cruise	0.958
6	Descent including leveling at 2000ft	0.99
7	Climb in case an alternate airport has to be reached	0.98
8	Second cruise at same cruise conditions	0.993
9	Descent	0.99
10	Landing, taxi and shut-down	0.992

The range equation is given as

$$R = \left(\frac{V}{g_0 \text{SFC}}\right)_{cruise} \left(\frac{L}{D}\right)_{cruise} \ln\left(\frac{W_i}{W_{i+1}}\right) \tag{6.6}$$

where R is the range in m, V is the cruise velocity in m/s, SFC is the specific fuel consumption corrected for thrust in kg/Ns and g_0 is the gravitational acceleration at 9.80665 m/s^2. The L/D ratio of the BWB during cruise is 19.0 [11]. The range is computed by subtracting the distance it takes to climb to and descent from the cruise altitude of 25,000 ft. Figure 6.1a shows that the climb angle between 10,000 ft and 20,000 ft is 6.4°. It is assumed that the climb angle remains constant from 20,000 ft until the cruise altitude is reached. The descent angle is assumed to be 2.5° from flight level 250 to 100, the same as was found for flight level 100 to 20. This results in a cruise distance of 765 nmi at a Mach number of 0.5. The cruise velocity can be found using Equation 6.7, where the speed of sound c_0 is found using the specific heat ratio γ at 1.4 and R as the specific gas constant for air at 287.05 J/(kg K). The ambient temperature T_0 is obtained through ideal gas assumptions for a standard atmosphere using Equation 6.8 [102], where T_{ISA} is the temperature in the International Standard Atmosphere (ISA) of 288.15 K, λ_T is the temperature gradient of -0.0065 K/m, H_0 is the altitude of the aircraft in m and H_{ISA} is the altitude at sea level, set to 0 m. The second cruise covers a range of 115 nmi at the same cruise velocity of 155 m/s without the climb and descent.

$$V_0 = c_0 M_0 = \sqrt{\gamma R T_0} M_0 \tag{6.7}$$

$$T_0 = T_{ISA} + \lambda_T (H_0 - H_{ISA}) \tag{6.8}$$

Rewriting Equation 6.6 for the required fuel fraction results in

$$\frac{W_{i+1}}{W_i} = e^{-\frac{R g_0 \text{SFC}}{V(L/D)}} \tag{6.9}$$

where the SFC for an A320 engine is 16.88 mg/Ns [118]. The fuel fraction is recalculated in an iterative process since it depends on the thrust and for equal T/W ratios thus on the aircraft weight as well.

Combining all weights, the (maximum) takeoff weight is found with

$$\begin{aligned} W_{TO} &= (0.4899 + (1 - M_{ff}) + M_{tfo}) W_{TO} + 30509 + 105 g_0 m_{pax} \\ &= \frac{30509 + 105 g_0 m_{pax}}{1 - 0.4899 - (1 - M_{ff}) - M_{tfo}} \end{aligned} \tag{6.10}$$

which equates to 360.1 kN. The MLW depends on the structural design and usually cannot be easily calculated, however for short range aircraft such as the REBEL-C the MLW is assumed to be the same

as the MTOW according to Vos[1]. The MTOW and MLW for both aircraft are given in Table 6.2 for a range of 900 nmi.

Table 6.2: Takeoff and landing weight of both aircraft at 900 nmi range

Aircraft	MTOW (kN)	MLW (kN)
A320-214	619.2	632.5
REBEL-C	360.1	360.1

6.3. Thrust setting

The thrust for the BWB is computed with equal T/W ratios for both aircraft. Since the NPD tables are generated with 85% MTOW and 90% MLW, the aircraft weight as given in Table 6.2 is slightly altered. The flight profiles for the A320 are generated with the TOW corresponding to the range bracket for departure. For the BWB, 85% of MTOW will be used as TOW, to find thrust settings to be analyzed for the NPD tables. For approach it is simpler, since the flight profile is computed using 90% of MLW for the A320 [5]. To compute the thrust, 90% of the BWB MLW will be used. These power settings are shown in Figure 6.3 and Figure 6.4 for the departure and arrival, respectively. Since the MTOW and MLW had to be estimated for the BWB, the results for $\pm$10% MTOW and MLW are shown as well.

For departure, the cutback at 1500 ft during departure is clearly shown in Figure 6.3 with a drop in the power output. As a result of assuming equal T/W ratios, both thrust outputs follow a similar pattern.

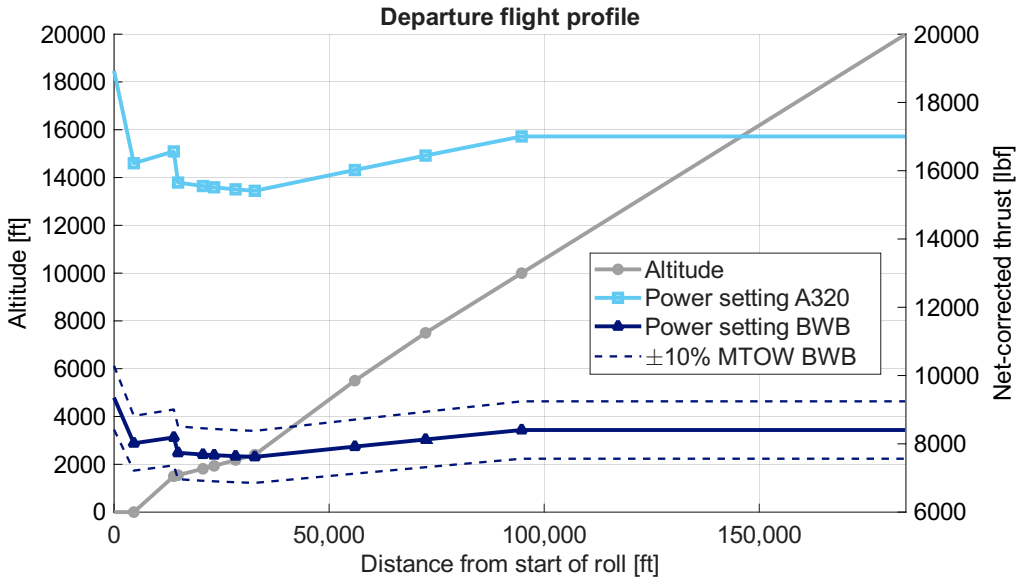

Figure 6.3: Thrust at departure following NADP2 and equal T/W ratios at TOW$_{A320} = 100\% W_{stagelength2}$ and TOW$_{BWB}$ = 85%MTOW

When idle thrust is selected during the approach the thrust does not actually become zero. Some ANP data show (near) zero results due to the computational method. These values are too low to analyze the engine parameters with GSP. Instead, the lowest thrust settings are taken to be at a value of N1%, meaning a percentage of the maximum fan rotational speed is taken and the corresponding thrust setting is used for further analysis. For the approach, van der Grift et al. stated that the measured idle rotational fan speed is around 30% [15]. This value has been used to compute the thrust for the lowest three values in Figure 6.4 for the A320. For all other data points of the TAW aircraft N1 is equal to or greater than 30%.

[1] private communication with R. Vos, associate professor at TU Delft

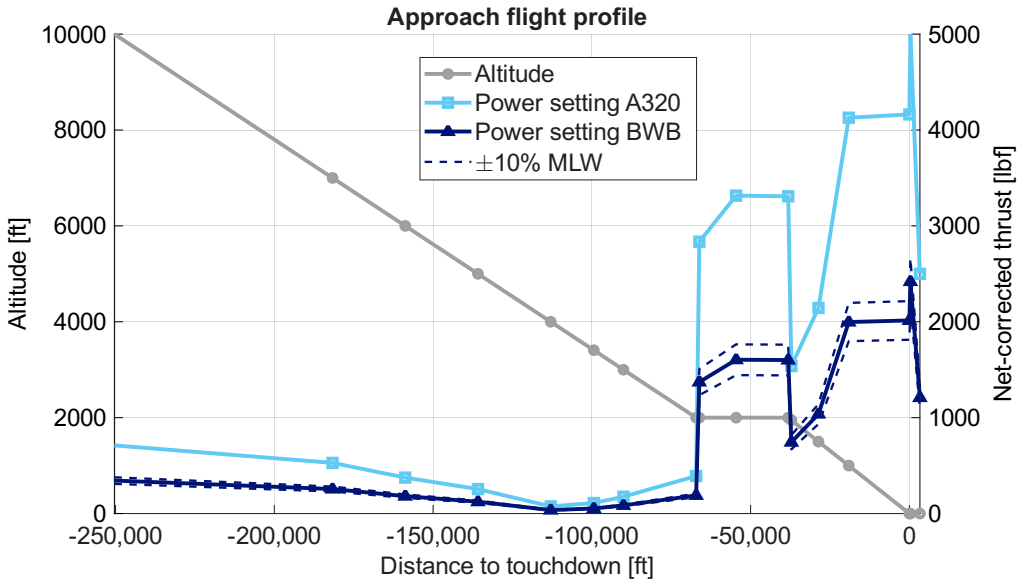

Figure 6.4: Thrust at arrival, with the lowest three thrusts of the A320 computed using N1% = 30%, with LW_{A320}=90%MLW and LW_{BWB}=90%MLW

6.4. Airframe component sizing

During both departure and approach HLD's are deployed for the A320. For the REBEL-C, the HLD requirements are unknown, just as the size of the landing gear. Due to the top-mounted engine installation that provides noise shielding, the engine noise is reduced and airframe noise is expected to be dominant. The sizing of the HLD's and landing gear is performed here. For the flaps, the deflection angle is determined as well.

6.4.1. High-lift devices

The HLD's are determined using BOLT, which is in the aircraft family of the REBEL-C developed in the same ARTEM project [31]. For BOLT, some analysis was done into the required slats and flaps with Krueger flaps designed for the leading edges of the wings. Inboard and outboard wing flaps were designed as well, shown in Figure 6.5 [9].

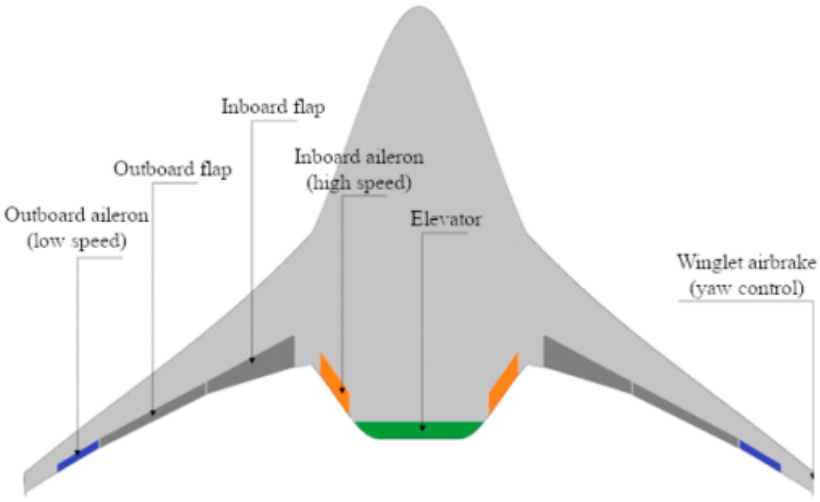

Figure 6.5: High-lift devices and control surfaces of BOLT, obtained from [9]

For the REBEL-C, it has been assumed that some of the HLD's are similar to BOLT. The leading edges of the wings will have Krueger flaps implemented. Separate research by NASA and DLR has shown that

Krueger flap noise and slat noise are quite similar in terms of noise levels, albeit with slightly different directivity patterns [119–121]. To simplify the modeling, it is assumed that the Krueger flap noise can be modeled well enough with Fink's slat noise method.

According to Vos, only the inboard flaps of BOLT are of use[2]. These are measured from Figure 6.5 and scaled to the size of the smaller REBEL-C, resulting in a total flap span of 8.0 m and a total flap area of 7.0 m^2. It is assumed that the trailing edge flaps are single-slotted flaps like the A320 and that the deflection angle is similar to that of the A320 during its flight.

6.4.2. Landing gear

The size of the wheels and struts of the landing gear is depends on the aircraft. Since the landing gear has not been designed for the REBEL-C, a sizing is done using conceptual design principles based on aircraft weight, runway types the aircraft encounters and AoA during takeoff and landing [122].

The number of main wheels N_{mw} is determined based on

$$N_{mw} = M_{TO}/210,000 \tag{6.11}$$

where the aircraft weight M_{TO} is in N and the number is rounded to the nearest multiple of 4, with a minimum of 4. This gives a total of 4 main wheels or 2 on each side. The number of nose wheels is set to 2 for transport aircraft. The amount of main struts N_{ms} is found by

$$N_{ms} = \begin{cases} 2, N_{mw} \leq 12 \\ 3 \text{ or } 4, N_{mw} > 12 \end{cases} \tag{6.12}$$

and with 4 main wheels, the number of main struts required is 2. The nose gear requires only one strut.

The wheel size depends on the type runway, which all have their own pavement classification number (PCN), indicating the maximum allowable tire pressure. With the flight profile obtained for Schiphol, the lowest asphalt pavement PCN it has is 79 [123]. The tire pressure is obtained through Equation 6.13 and found to be 1.2 MPa for the tires.

$$p_{tire} = 430 \ln(\text{PCN}) - 680, \text{ for } 10 < \text{PCN} < 100 \tag{6.13}$$

The second factor determining the tire size if the static load per wheel P_w. This is found using

$$P_w = \begin{cases} 0.92 W_{TO}/N_{mw}, \text{ for the main wheels} \\ 0.08 W_{TO}/N_{nw}, \text{ for the nose wheels} \end{cases} \tag{6.14}$$

where 0.92 indicates that 92% of M_{TO} is carried by the main gear [124]. Using both the tire pressure and the static wheel load, the wheel size can be determined through looking up existing wheels that can handle both in the graphs (Figure 10-15) given by Torenbeek [124]. This results in the main wheels having a diameter of 0.84 m and a width of 0.25 m, whereas the nose wheels are 0.46 m in diameter and 0.11 m wide.

Having determined the wheel sizes, the strut length can be found. The strut length depends on the location, since the main landing gear has to be positioned behind the center of gravity. As the center of gravity is unknown for the REBEL-C it is assumed that the landing gear location of BOLT, which is known [9], can be scaled to the REBEL-C using Figure 6.6.

This location is then used to determine the length of the strut, assuming a high scrape angle of 20° due to the high AoA used by BWB [24]. The absorber length is typically between 0.2 and 0.5 m [122]. A length of 0.4 m was chosen to ensure proper absorption. The main strut length is found via

$$l_s = l_{absorber} + \tan(20°)(l_{fuselage} - x_{mLG}) - d_{mw}/2 \tag{6.15}$$

where $l_{fuselage}$ is the fuselage length in m, x_{mLG} is the main landing gear location from the nose in m and d_{mw} is the main tire diameter in m. This results in the main strut length being 1.50 m. The nose

[2] private communication with R. Vos, associate professor at TU Delft

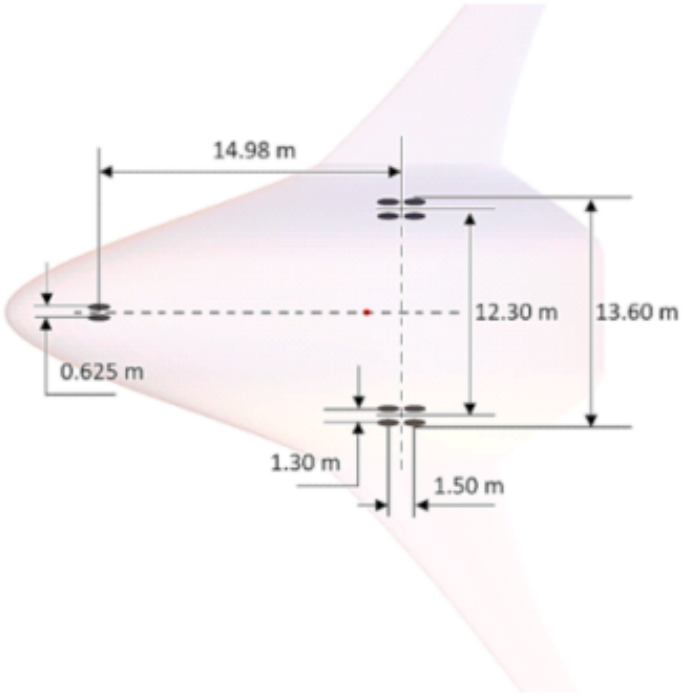

Figure 6.6: Landing gear location of BOLT, obtained from [9]

strut length is found by assuming the aircraft has to stand horizontal on the ground and is 1.57 m. All landing gear parameters are shown in Table 6.3.

Table 6.3: Landing gear sizing

Variable	Symbol	Main	Unit	Nose	Unit
Number of wheels	N_w	4	-	2	-
Wheel diameter	d_w	0.838	m	0.457	m
Number of struts	N_s	2	-	1	-
Strut length	l_s	1.50	m	1.57	m

7. Results and Discussion

Using the framework set up in chapter 5, the ΔSPL tables for engine noise shielding and the inputs from the flight profile, the flyovers are first computed in this chapter for the REBEL-C. This results in the NPD tables for the BWB, which are discussed and compared to the A320. Furthermore, a sensitivity analysis has been performed on airframe dimensions and noise shielding.

7.1. Input

In order to generate the NPD data, the thrust setting is required. The power settings chosen for analysis are a combination of the flight profile of the BWB and limitations of the CFM56-5B4 engine in GSP. The CFM56-5B4 is used in this analysis since the turbofan design of the REBEL-C is unknown.

For departure, maximum takeoff thrust is used at 160 kt corresponding to 22500 lbf, as well as 85% of maximum takeoff thrust corresponding to 19000 lbf. Both are values often used for environmental (emissions) assessment [125]. To prevent extrapolation, the minimum thrust is chosen below the lowest thrust setting required for the BWB, taking the $\pm$10% in MTOW into account. Looking at Figure 6.3 this is 6000 lbf net-corrected thrust. With an equal T/w ratio, this is roughly equivalent to 12000 lbf thrust of the A320. The highest thrust settings used by the BWB during departure at 85% MTOW is short of 11000 lbf net-corrected thrust. Since 11000 lbf correlates to using 22500 lbf for the A320 using equal T/W ratios, this value has been chosen. One more thrust setting is chosen at 8500 lbf net-corrected thrust, right in between the two. An overview of all the net-corrected power settings analyzed is given in Table 7.1. The Krueger flaps, which are modeled as slats [121] and the single slotted flaps are both deployed, the latter at an 10° deflection angle like the A320 [113].

For arrival, ICAO recommends using 30% and 7% of maximum thrust [125] for emissions calculations, corresponding to 6800 lbf and 1600 lbf thrust, respectively. Figure 6.4 indicates that the lowest net-corrected thrust setting is just 36 lbf. This is however too low for GSP to calculate the engine conditions. The minimum fan rotational speed GSP is able to compute for is for N1 = $\pm$15%. Therefore, the thrust corresponding with N1 = 15% has been chosen, which is 155 lbf at 1000 ft altitude and 160 kt. To ensure the full flight path is captured, 2900 lbf has been used. Using equal T/W ratios, 2900 lbf corresponds to the 6000 lbf case from the A320 as well. A 1000 lbf thrust case will be used in a sensitivity analysis, where the airframe noise is expected to dominate fully. All these net-corrected thrusts have been recomputed to the actual thrust at 1000 ft altitude and a speed of 160 kt. The engine conditions are analyzed using GSP. All thrust settings used in the analysis are shown in Table 7.1. The flaps are extended to 35°, similar to the A320 [113]. The slats and landing gear are both deployed.

Table 7.1: Net-corrected power settings used to obtain NPD tables for the REBEL-C

Departure F_N/δ [lbf]	**Approach F_N/δ [lbf]**
22500	6800
19000	2900
11000	1600
8500	1000
6000	155

The data from the CFM56-5B4 is used with the settings as shown in Table 5.1b. The airframe inputs are shown in Table 7.2.

Table 7.2: BWB airframe inputs

Parameter	Value
Wing span [m]	32.45
Wing surface area [m^2]	326.03
Flap span [m]	8.0
Flap surface area [m^2]	7.0
Main wheel diameter [m]	0.838
Nose wheel diameter [m]	0.457
Main strut length [m]	1.50
Nose strut length [m]	1.57
Number of wheels per strut [-]	2
Number of main struts [-]	2
Number of nose struts [-]	1

7.2. Departure

The five departure thrust settings are analyzed first. Flyovers calculated with SOPRANO at 1000 ft are shown. These are used to perform the calculations for the NPD tables of the REBEL-C, which are then compared to the tables of the A320.

7.2.1. Flyover

For the maximum net-corrected thrust of 22500 lbf a direct comparison can be made with the A320. Figure 7.1 shows the results for the maximum and minimum thrust. The noise reduction due to the engine placement becomes quite clear, showing a reduction of 12.4 dBA for $L_{A_{max}}$ at F_N/δ = 22500 lbf. Taking the results at each 0.5 s interval shows sharp peaks from the engine noise shielding, with an area around t = 0 s where there is less noise compared to before and after. The engine noise shielding increases the 10 dBA downtime significantly. Since Figure 6.3 indicates the maximum thrust of the CFM56-5B4 engine will not be needed during takeoff, an equal T/W ratio case has been analyzed as well. The maximum power setting corresponding with this is 11000 lbf of thrust. $L_{A_{max}}$ is reduced by 18.7 dBA. For this power setting, the airframe noise dominates at $L_{A_{max}}$, however the engine noise is still present before the peak and after the peak it dominates. The airframe noise already becomes dominant for the maximum departure thrust the BWB is expected to use. The two lower thrust settings, 8500 lbf and 6000 lbf, show even more airframe noise dominance. Since this remains constant $L_{A_{max}}$ remains roughly equal. All flyovers are shown on a component basis in Appendix D.

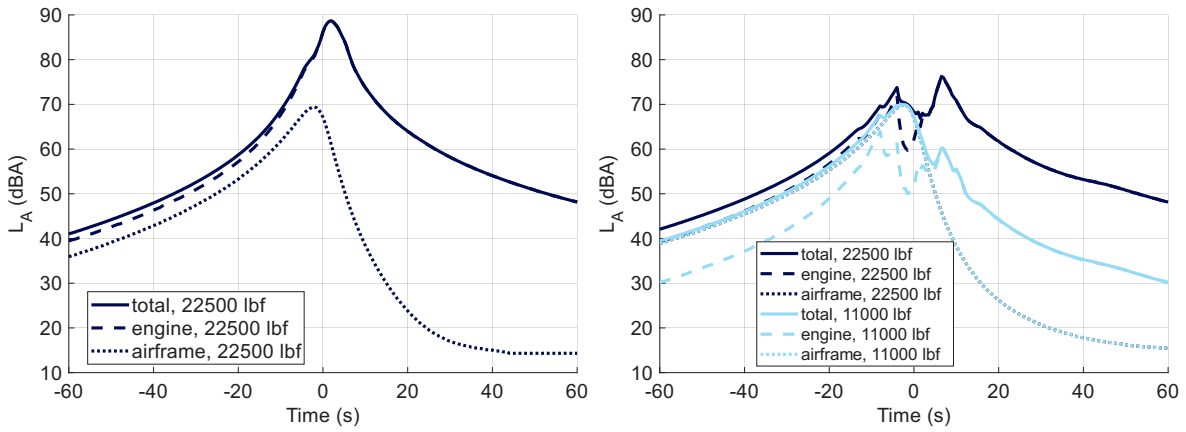

(a) Noise of an A320 at F_N/δ = 22500 lbf

(b) Noise of the REBEL-C at F_N/δ = 22500 lbf and F_N/δ = 11000 lbf

Figure 7.1: Flyover at 1000 ft and 160 kt of A320 and BWB simulated in SOPRANO for various power settings during departure

7.2.2. Noise-power-distance tables

The NPD results for the flyover at 1000 ft have been propagated to the other slant distances following the methodology from chapter 5. As expected, Figure 7.2 shows that $L_{A_{max}}$ for the lowest three power

settings is very similar, with differences only shown for the shortest slant distances. This might be due to the presence of high frequency fan inlet noise, which does not get absorbed at these shorter distances. Following $L_{A_{max}}$, the SEL shown in Figure E.1 in Appendix E shows the same type of regression.

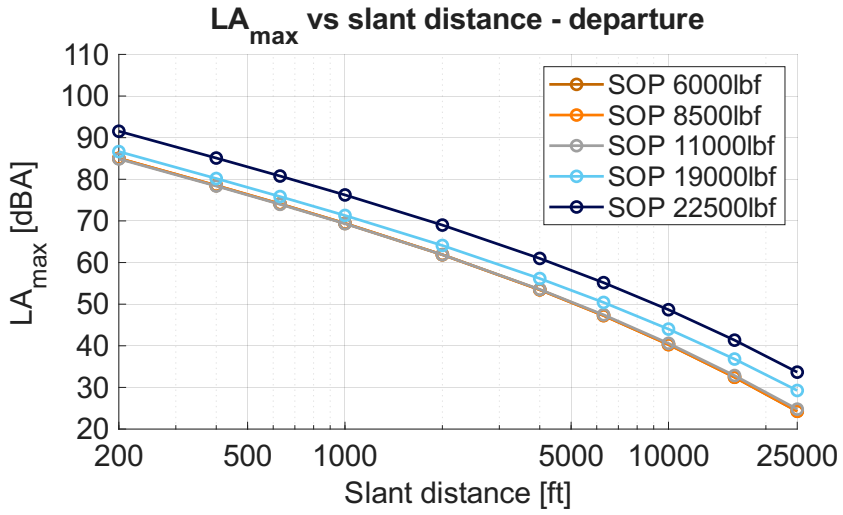

Figure 7.2: L_{Amax} for the BWB during departure

The tonal corrections performed on the data to obtain PNLT likely causes Figure 7.3 to be less smooth. $PNLT_{max}$ is similar for the three lowest power settings, just as for $L_{A_{max}}$. The same can be said about the EPNL shown in Figure C.2 in Appendix E. Table E.1 contains all NPD values for the departure.

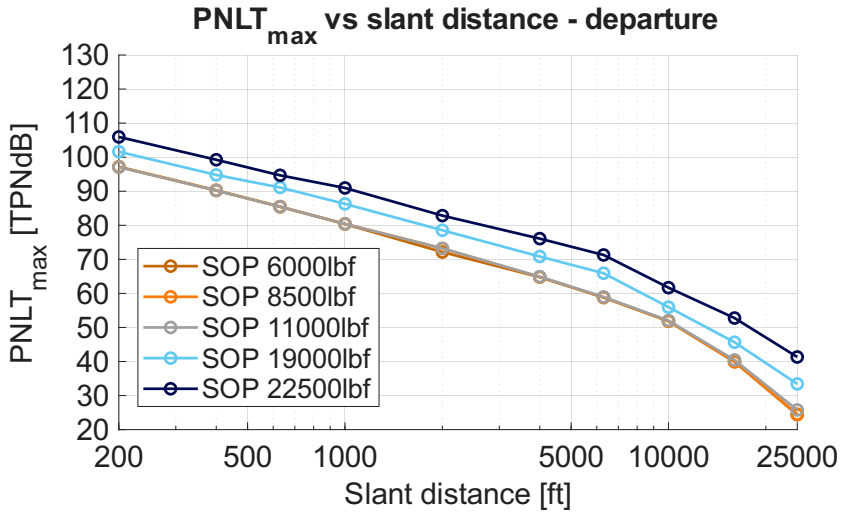

Figure 7.3: $PNLT_{max}$ for the BWB during departure

7.3. Approach

During approach, the thrust settings are generally lower than during departure and thus even more airframe noise dominance is expected. The higher flap deflection angle should increase the flap noise, while the presence of the landing gear should show as well.

7.3.1. Flyover

Comparing the 2900 lbf thrust for the BWB with the 6000 lbf thrust of the A320 in Figure 7.4 gives the opportunity to see the effect of the lower aircraft weight. For the A320 both engine and airframe noise dominate. This is different for the REBEL-C, where the airframe noise fully dominates. Overall $L_{A_{max}}$ is reduced by 3.8 dBA, much less than for departure. For all other power settings the airframe noise

is dominant as well. Flyovers showing all noise components for each power setting can be found in Appendix D.

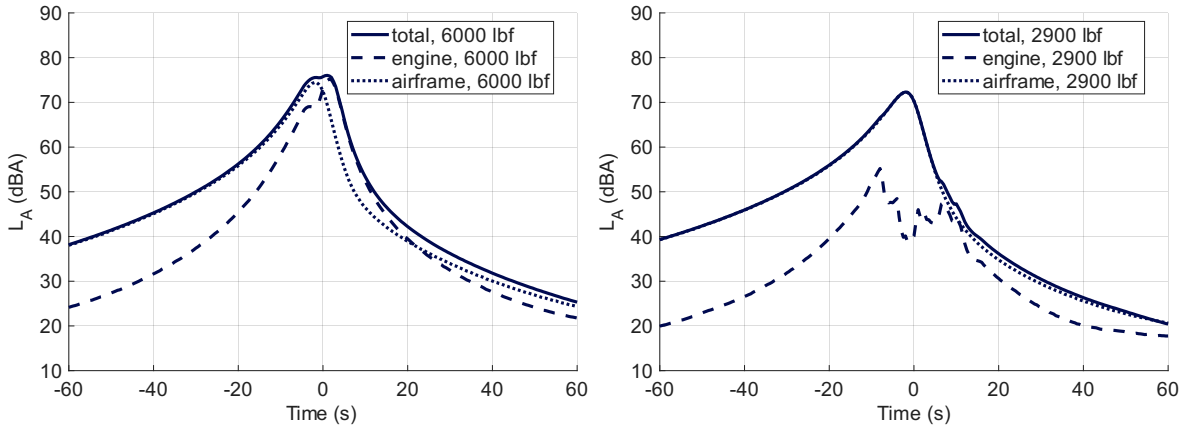

(a) Noise of an A320 at F_N/δ = 6000 lbf

(b) Noise of the REBEL-C at F_N/δ = 2900 lbf

Figure 7.4: Flyover at 1000 ft and 160 kt of A320 and BWB simulated in SOPRANO for various power settings during approach

7.3.2. Noise-power-distance tables

Due to the consistent airframe dominance, $L_{A_{max}}$ is the same for all approach power settings. The SEL differs slightly for the lowest slant distance at 6800 lbf thrust, due to the presence of fan inlet noise as shown in Figure D.5. For 2900 lbf thrust, this has already decreased to such a level that it has no effect on the results. The SEL plot can be found in Appendix E.

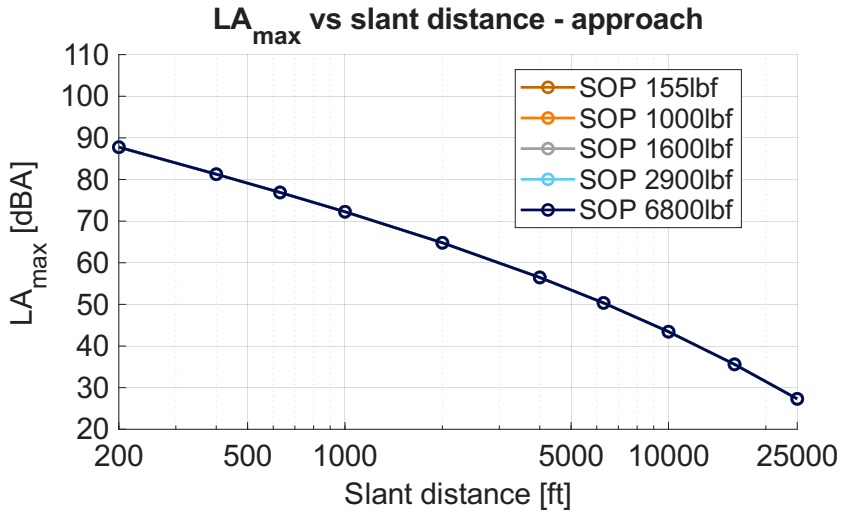

Figure 7.5: L_{Amax} for the BWB during approach

The same can be said about $PNLT_{max}$, as shown in Figure 7.6. Therefore, one might argue that just using 6800 lbf, 1600 lbf and 155 lbf should suffice for the NPD tables. The EPNL results show the same trend and can be found in Appendix E. Table E.2 contains all NPD values for the approach.

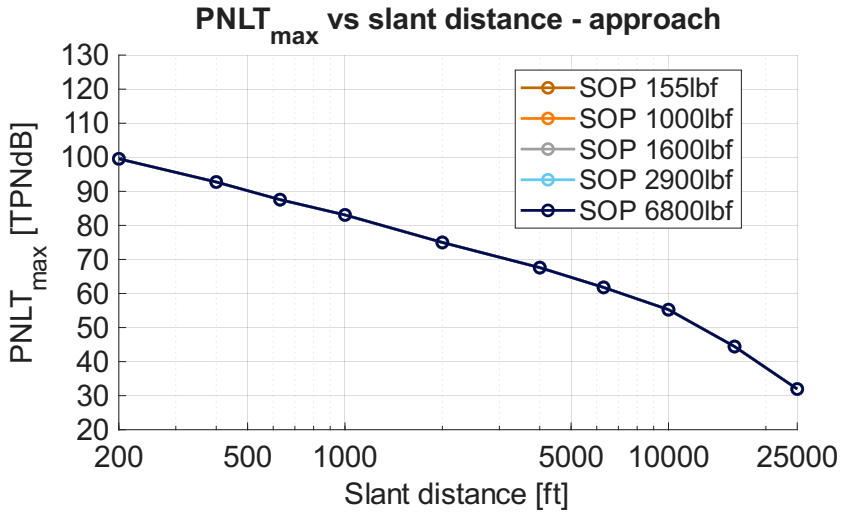

Figure 7.6: PNLT$_{max}$ for the BWB during approach

7.4. Comparison with A320

In order to better grasp the effect of using a BWB aircraft compared to a TAW aircraft, the noise metrics for the REBEL-C and A230 are studied side by side. The results from SOPRANO are used for both aircraft. Three cases are compared, one for maximum thrust for both aircraft and two using equal T/W ratio assumptions for maximum thrust and minimum thrust. These are shown in Figure 7.7. The largest reduction is obtained for 22500 lbf thrust for the A320 and 11000 lbf thrust for the REBEL-C. For the A320, the engine noise dominates at this thrust setting while for the REBEL-c, the shielding reduces the engine noise to levels well below the airframe noise. The median is -18.2 dBA for L$_{A_{max}}$ and the difference is even larger for PNLT$_{max}$ at -21.2 TPNdB. If both aircraft fly at the maximum thrust of the CFM56-5B engines, the difference becomes smaller since the engine noise is present for the BWB. The difference is still relatively large. For the lowest thrust settings of departure, 12000 lbf for the A320 and 6000 lbf for the BWB are compared. Although the actual T/W ratio would dictate a slightly lower thrust setting for the REBEL-C, since the airframe already dominates the differences will be negligible. A much larger spread is shown compared to the other two departure cases, however the noise reduction is still substantial.

For the approach, two cases are depicted. The first one is shown for 6000 lbf and 2900 lbf for the A320 and REBEL-C, respectively. Compared to the departure, the differences are much smaller, although still in favor of the BWB. For the A320 there is still some engine noise present, whereas for the REBEL-C the airframe noise is fully dominant. For the lowest thrust setting of the A320 the airframe noise dominates more, reducing the noise metrics slightly. For the REBEL-C, no equal T/W ratio was computed for 2700 lbf of the A320. For the lower thrust settings of 1000 and 1600 lbf of the BWB no differences are expected between them since the airframe dominates fully, thus a comparison was made. For this case, the differences are smallest, with the median not getting below -2.9 dB across all four noise metrics.

Overall, the noise produced by the REBEL-C is lower than the A320 for all analyzed cases. Since the difference varies, two comparison cases are plotted for L$_{A_{max}}$ to better understand the deviations. When looking at Figure 7.8 it immediately becomes apparent that the lowest departure thrust for the REBEL-C of 6000 lbf results in lower L$_{A_{max}}$ than for the approach thrust of 2900 lbf. Since the airframe noise dominates for both cases, the retracted landing gear and lower flap deflection angle cause the lower results for the departing BWB. When comparing the BWB with the A320, it becomes clear that L$_{A_{max}}$ decreases at a faster rate for the TAW aircraft. Presence of more mid to high frequency noise in the spectrum of the A320 is the likely cause of this, since high frequencies get absorbed more quickly. High frequencies are attenuated the most due to shielding for the REBEL-C. The spectra will likely be dominated by low frequency noise, for which the atmospheric absorption is lower. For the approach the decrease of the A320 is closer to that of the REBEL-C due to the lower engine noise.

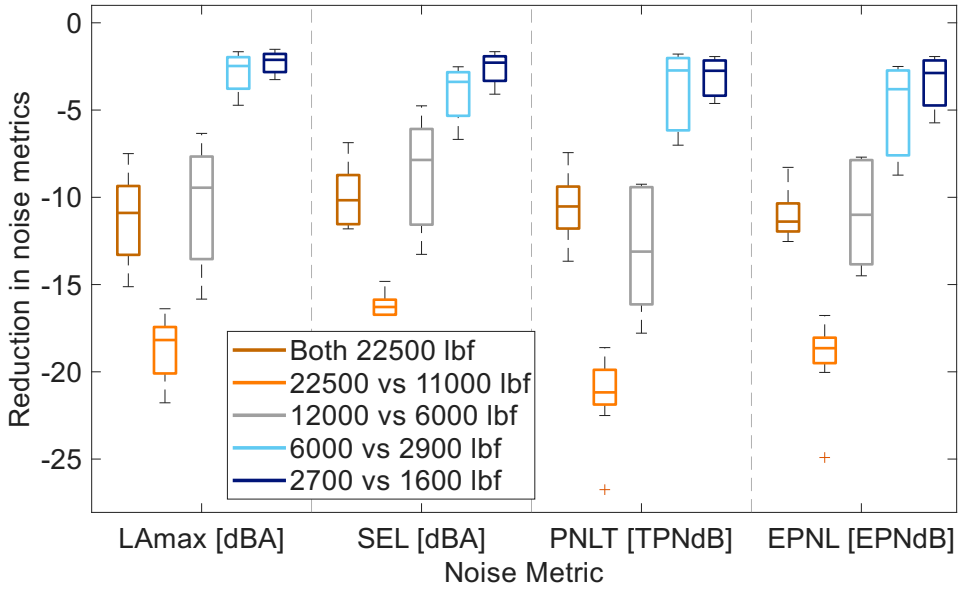

Figure 7.7: Boxplot showing the reduction in noise metrics for the REBEL-C compared to the A320

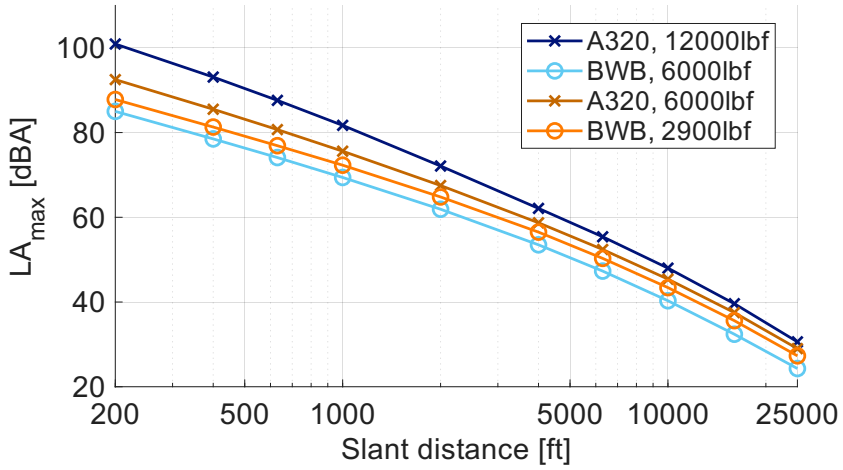

Figure 7.8: $L_{A_{max}}$ for various thrust settings of the A320 and REBEL-C

Since the airframe of the REBEL-C is distinct from a TAW aircraft like the A320, a more in-depth analysis of the airframe noise has been done using the flyover data. As Figure 7.9 shows, the total airframe noise of the A320 is higher during approach. The wing with a larger span generates more noise than the wing of the BWB around the peak, even though the wetted area of the BWB is much larger. It should be noted that the BWB has both wing and operating characteristics that are outside the assumptions made by Fink [82], such as the sweep angle and AoA. For both aircraft the wing noise is lower than other noise sources. While the flaps, slats and landing gear dominate for both aircraft, a difference in flap and slat presence is seen. The flap noise is higher for the A320 due to the larger flap size, while the wing planform increases the slat noise for the BWB. The directivity function of the flap causes the sharp decrease t = 5.5 s. The larger landing gear produces more noise for the A320, however SOPRANO does not consider the higher freestream velocities the landing gear of the BWB encounter [13]. This will likely increase the landing gear noise.

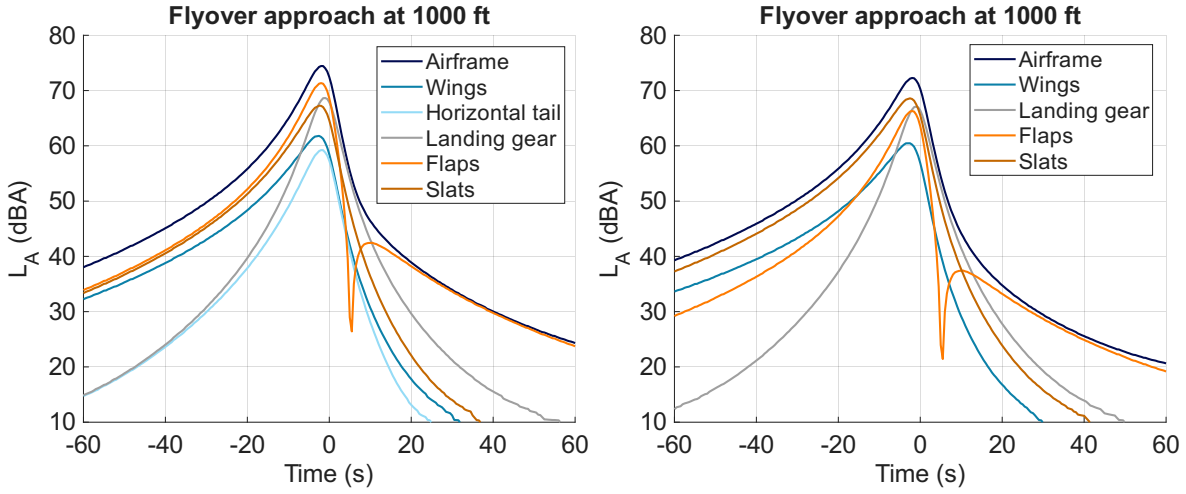

(a) A320 airframe noise

(b) REBEL-C airframe noise

Figure 7.9: Approach airframe noise comparison between the A320 and REBEL-C for a flyover at 1000 ft

7.5. Sensitivity Analysis

Since assumptions had to be made on both the airframe components and the engine noise shielding, a sensitivity analysis was done to analyze the effect of these assumptions on one approach case where the thrust is 1000 lbf.

7.5.1. Airframe

The flap size has been assumed using BOLT as a reference as shown in subsection 6.4.1. The flap deflection angle has been based on the A320. The landing gear has been sized using the estimated aircraft weight and should therefore be analyzed as well.

First the flaps are both decreased and increased up to -20% and +40% in span and surface area. Increasing the flap size by up to 40% does increase the overall noise, however it is limited to less that 1 dBA at 1000 ft. Increasing the flap surface area only by 40% or flap span only by 40% results in the same increase as increasing both the flap surface area and span by 20%. The largest increase is shown if there are outboard flaps present and deployed as well. The effect of including outboard flaps on the NPD tables is shown in Figure 7.10. The flyover including showing the effect for changing the flap size is shown in Appendix D.

Secondly, the flap deflection is speculated to influence the results as well. Whereas higher flap deflection angles might not be realistic, less flap deflection has been analyzed, decreasing the flap angle by 5° until reaching 15°. A reduced flap setting is often used [111], for which the flaps of the A320 deploy to 20° and the slats extend to 22° [113]. This reduced flap deflection angle decreases the total noise on average by less than 0.5 dB when looking at Figure 7.10. All flyover plots can be found in Appendix D.

Next, the landing gear struts length and wheel diameter were varied by 20% to see the effect of the assumptions that were made regarding the aircraft weight and runway surface, including what would happen in twice the amount of wheels were used. It was found that increasing only the strut length by 20% does not change the results noticeably, as it is on the same level as the baseline. The same trend is found for a 20% increase in wheel diameter, which gives virtually the same results with and without increasing the strut length. The noise increase is on average between 0.5 and 0.8 dB for all noise metrics in the NPD tables, as shown in Figure 7.10. The flyovers are shown in Appendix D.

Finally, the Krueger flap noise has been assumed to be similar to the slat noise. This is however assuming a simple Krueger flap, not an optimized Krueger flap. It has been shown by DLR that a noise reduction of 3 dB can be reached for frequencies up to 2000 Hz. For higher frequencies an optimized Krueger flap might produce 5 dB less [121]. Using this as a constant reduction for each polar angle, Figure 7.10 shows an average slat noise reduction of 0.5 to 1.0 dB can be achieved for the NPD tables. Overall, the difference between the baseline and the variation in HLD and landing gear size was found

to be small.

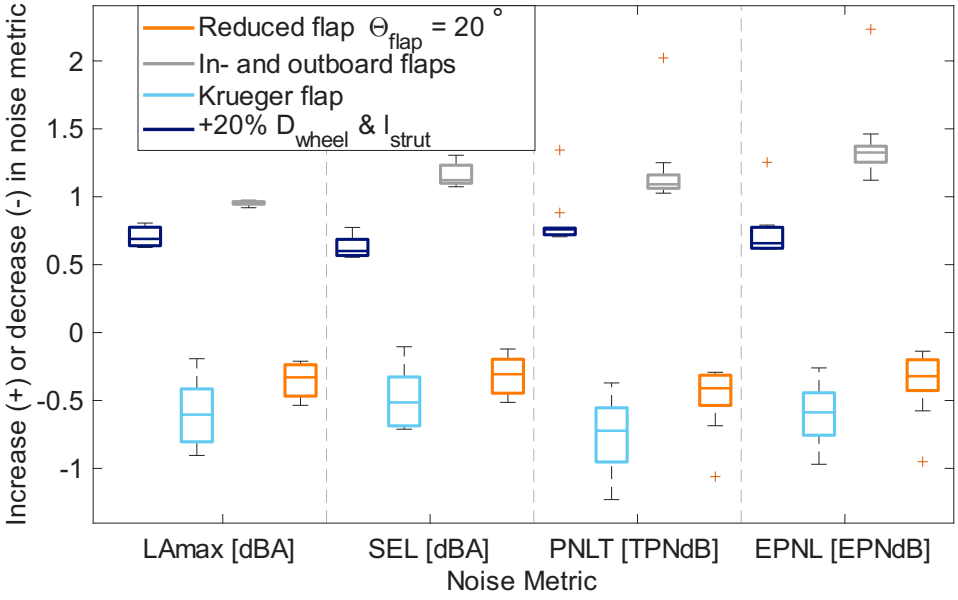

Figure 7.10: Boxplot showing the reduction and increase of the NPD results at approach with variation in airframe size for F_N/δ = 1000 lbf

7.5.2. Engine shielding

To analyze the effect of the shielding spatial resolution, the three variations mentioned in subsection 4.2.4 have been run. Using a lower number of data points (u = 36) results in a much coarser overall flyover plot. Although the attenuation due to shielding only has to be performed once, if lateral flyovers have to be considered for other research the computational time and power required would increase enormously. Using a 10° increment between observers on the hemisphere defined in chapter 4 would take just 50-60 minutes to run instead of 9.5 hours for the fine grid that has been used here, which was only analyzed directly below the aircraft.

The overall difference for all NPD results is given in Figure 7.11. Here it can be noticed that the peaks for the largest thrust setting, which are also present in Figure D.10 in Appendix D, cause a deviation in the results. For the tone corrected result, PNLT_{max}, the results differ the most. If just one engine noise source location is considered, in this case the fan exit location since it is located in the middle, the results would be quite different. Figure 7.11 shows the effect it has compared to using multiple noise source locations.

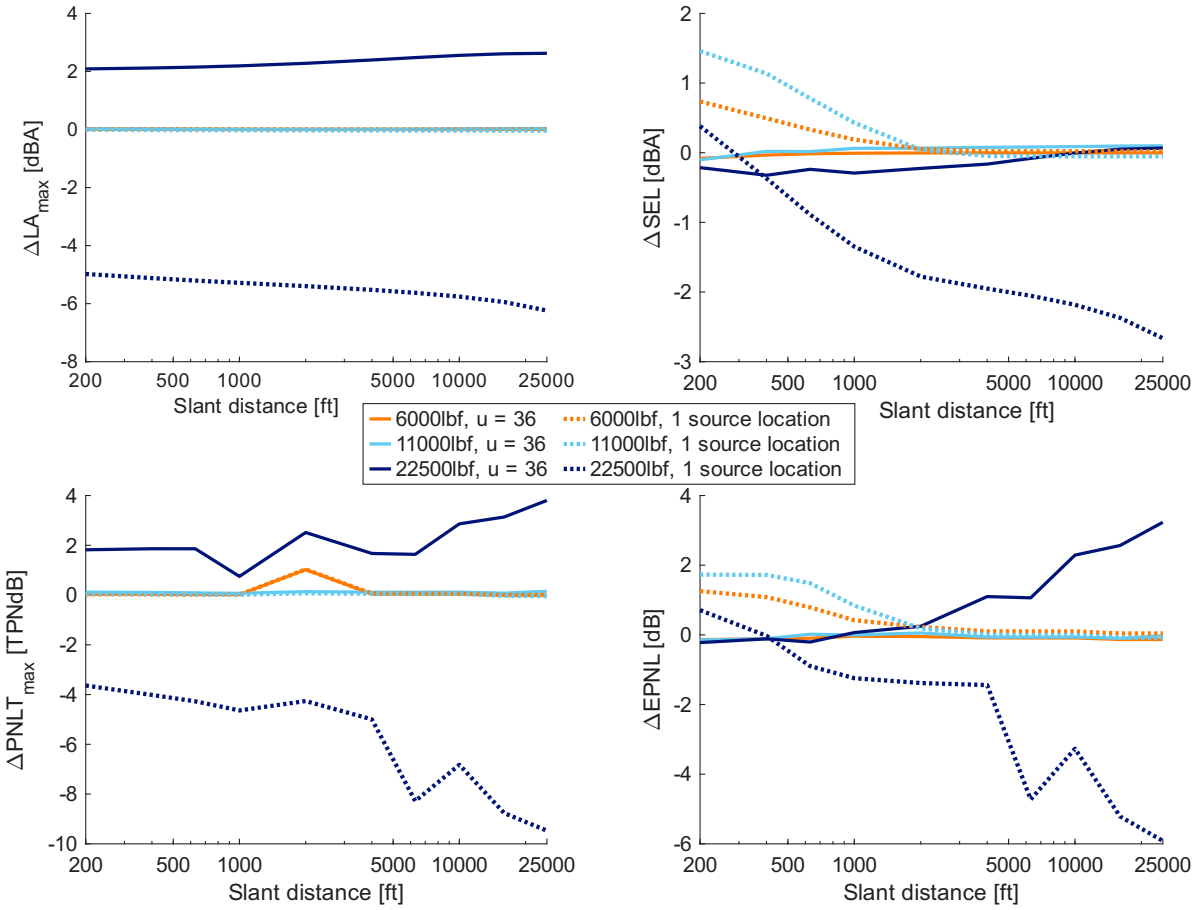

Figure 7.11: $\Delta L_{A_{max}}$, ΔSEL, ΔPNLT_{max} and ΔEPNL for using u = 36 vertices in the shielding calculations or using one engine noise source location for all engine noise sources. Computed using $\Delta L_{A_{max}} = L_{A_{max,base}} - L_{A_{max,var}}$ where var is one of the two new variants

8. Conclusion

In this chapter conclusions are drawn, followed by recommendations for future research.

8.1. Conclusions

The objective of this report was to develop a method for and obtain the NPD tables of the REBEL-C. This was done using the semi-empirical noise modeling program SOPRANO, for which engine parameters were obtained with GSP. ΔSPL tables were included for engine noise shielding, which was analyzed separately for three noise source locations. The flyovers defined in SOPRANO gave the results for one altitude of 1000 ft, which were propagated to the other slant distances following the methodology of SAE AIR1845.

Looking at noise shielding, including creep in the calculations had relatively little effect on the results compared to using edge-diffraction only. The effect was larger for higher frequencies, where more attenuation was observed. The engine component source location was shown to be of importance. The jet noise source, located more aft, was shielded less even in front of the aircraft. It is hypothesized that this is due to more or stronger edge-diffraction. The more central location of the fan inlet caused more attenuation due to shielding.

The framework to obtain NPD tables using a flyover in SOPRANO was set up. Using the same power settings for the A320 the results matched those in the ANP database quite well, with a maximum RMSE found for PNLT$_{max}$ at 2.3 TPNdB. For the Boeing 777 and A330 the RMSE was maximum for the same noise metric at 3.4 and 3.5 TPNdB, respectively. It is therefore concluded that using semi-empirical noise modeling to predict NPD tables seems promising. The engine noise was found to dominate during departure. The airframe noise was more dominant during arrival, while the fan outlet noise is still present. No noise reduction measures such as fan liners or engine noise reflection by the wing was included.

The same set up was used for the REBEL-C, for which the same CFM56-5B4 engine was used. It was shown that engine noise is dominant for the highest thrust settings, however airframe noise starts to dominate for thrust settings of 11,000 lbf and lower. This is shown in the NPD tables as well, with the two highest thrust settings clearly distinct and the lower three all more or less overlapping. Comparing the maximum thrust results of both aircraft show a reduction in $L_{A_{max}}$ of 12.4 dBA for a distance of 1000 ft for the REBEL-C. Assuming equal T/W ratios, $L_{A_{max}}$ is reduced by 18.7 dBA. For approach the differences are smaller, with the REBEL-C producing 3.8 dBA less in $L_{A_{max}}$ for equal T/W ratios at 1000 ft. It was shown that this was due to airframe dominance, which is why all results in the NPD tables are similar. Due to the airframe configuration and noise shielding, the BWB produces more noise during approach than during departure.

A sensitivity analysis on the flap surface area and span, flap deflection angle, type of leading edge device and landing gear size showed a mean absolute deviation in the NPD tables between 0.3 to 1.1 dBA and 0.3 to 1.4 PNdB. This shows that the assumptions made on the sizing do not greatly influence the results. Comparing ΔSPL tables for a lower number of vertices showed more differences of up to 4 EPNdB across all slant distances for the highest thrust setting of 22500 lbf where engine noise dominates. Using a very crude 10° increment between polar and azimuthal angles in the ΔSPL tables reduces the computational time by a factor of 8-10. A larger deviation was found when only one noise source is considered, showing differences getting close to 10 TPNdB. It can therefore be concluded that using multiple source locations and a refined observer grid is important.

8.2. Recommendations

Insights gained in this research have led to a number of recommendations. First, recommendations on for noise calculations on the REBEL-C itself are given.

- The flight path of the BWB aircraft needs to be analyzed in more detail. The climb angle of the REBEL-C is expected to be much higher than that of the A320. This will effect the power settings and with that the results.
- Fink's method has been developed for conventional aircraft and used for the REBEL-C here as well. A better option would be to develop a new airframe component noise model for BWB aircraft, due to the higher AoA, high sweep and different local airspeed around components. The landing gear for example will probably produce more noise due to the higher local velocity.
- Using a ultra-high BPR turbofan compatible with the REBEL-C to compute the engine conditions instead of the older CFM56-5B will give more accurate and probably lower noise levels. Using the engine from the A320neo (LEAP-1A) might already be better, however that is still overpowered.

Secondly, some recommendations are done on the NPD tables, for the generation of the noise metrics or the use of them.

- Noise reduction technologies could be applied into SOPRANO, such as fan liners or porous materials. Furthermore, installation effects as wing reflection and wing scattering for the A320 could be included as well. This has not been implemented in this research for the BWB nor A320. Furthermore, the BWB might contain more noise reducing technologies in the airframe.
- The lateral engine installation correction used in Doc 29 is likely not applicable for the REBEL-C. Finding a new correction by means of an equation or by generating a table for this is recommended.

Finally, the noise shielding analysis might benefit from extra research in the future.

- The $\triangle$SPL tables used for shielding are now computed using a monopole noise source, whereas in reality this is not the case. The best option would be to use the actual engine component results and directivity.
- The engine component source location used for the shielding analysis could be done for an optimized engine location in terms of noise shielding. The lower attenuation of jet noise would be another interesting research topic within this category. Furthermore, the jet source depends on the power setting and moves further aft when more thrust is required. The effect this has the actual attenuation resulting from it would require more research.

References

[1] C. Eriksson et al. “Long-Term Aircraft Noise Exposure and Body Mass Index, Waist Circumference, and Type 2 Diabetes: A Prospective Study”. In: *Environmental Health Perspectives* 122.7 (2014), pp. 687–694. DOI: 10.1289/ehp.1307115. URL: https://ehp.niehs.nih.gov/doi/abs/10.1289/ehp.1307115.

[2] C. Baudin et al. “Aircraft Noise and Psychological Ill-Health: The Results of a Cross-Sectional Study in France”. In: *International Journal of Environmental Research and Public Health* 15.8 (2018). ISSN: 1660-4601. DOI: 10.3390/ijerph15081642. URL: https://www.mdpi.com/1660-4601/15/8/1642.

[3] European Parliament and Council of the European Union. *Decision (EU) 2022/591 of the European Parliament and of the Council of 6 April 2022 on a General Union Environment Action Programme to 2030*. Official Journal of the European Union, L 114, 12 April 2022, pp. 22–36. Accessed 07-04-2026. 2022. URL: https://eur-lex.europa.eu/eli/dec/2022/591/oj/eng.

[4] European Environment Agency. *Environmental noise in Europe 2025*. EEA Report 05/2025. DOI: doi:10.2800/5134480.

[5] European Civil Aviation Conference. *Report on Standard Method of Computing Noise Contours around Civil Airports Volume 2: Technical Guide*. ECAC.CEAC Doc 29. Dec. 2016.

[6] European Civil Aviation Conference. *Report on Standard Method of Computing Noise Contours around Civil Airports Volume 1: Applications Guide*. ECAC.CEAC Doc 29. Dec. 2016.

[7] International Civil Aviation Organization. *Guidance on the Balanced Approach to Aircraft Noise Management (Doc 9829)*. 2nd ed. International Civil Aviation Organization. 2008.

[8] X. Liu et al. “Development and progress in aeroacoustic noise reduction on turbofan aeroengines”. In: *Progress in Aerospace Sciences* 130 (2022), p. 100796. ISSN: 0376-0421. DOI: https://doi.org/10.1016/j.paerosci.2021.100796. URL: https://www.sciencedirect.com/science/article/pii/S037604212100097X.

[9] R. Pieren et al. “Perception-based noise assessment of a future blended wing body aircraft concept using synthesized flyovers in an acoustic VR environment—The ARTEM study”. In: *Aerospace Science and Technology* 144 (2024), p. 108767. ISSN: 1270-9638. DOI: https://doi.org/10.1016/j.ast.2023.108767. URL: https://www.sciencedirect.com/science/article/pii/S1270963823006636.

[10] P.D. Bravo-Mosquera, F.M. Catalano, and D.W. Zingg. “Unconventional aircraft for civil aviation: A review of concepts and design methodologies”. In: *Progress in Aerospace Sciences* 131 (2022). ISSN: 0376-0421. DOI: https://doi.org/10.1016/j.paerosci.2022.100813. URL: https://www.sciencedirect.com/science/article/pii/S0376042122000070.

[11] F. Centracchio, M. Rossetti, and U. Iemma. “Approach to the Weight Estimation in the Conceptual Design of Hybrid-Electric-Powered Unconventional Regional Aircraft”. In: *Journal of Advanced Transportation* 2018.1 (2018), p. 6320197. DOI: https://doi.org/10.1155/2018/6320197. URL: https://onlinelibrary.wiley.com/doi/abs/10.1155/2018/6320197.

[12] J.J. Berton and W.J. Haller. “A Noise and Emissions Assessment of the N3-X Transport”. In: *52nd Aerospace Sciences Meeting*. Jan. 2014. DOI: 10.2514/6.2014-0594. URL: https://arc.aiaa.org/doi/abs/10.2514/6.2014-0594.

[13] Y. Guo, C.L. Burley, and R.H. Thomas. “On Noise Assessment for Blended Wing Body Aircraft”. In: *52nd Aerospace Sciences Meeting*. American Institute of Aeronautics and Astronautics, Jan. 2014. DOI: 10.2514/6.2014-0365. URL: https://arc.aiaa.org/doi/abs/10.2514/6.2014-0365.

[14] R. Thomas, C. Burley, and E. Olson. “Hybrid Wing Body Aircraft System Noise Assessment with Propulsion Airframe Aeroacoustic Experiment”. In: *16th AIAA/CEAS Aeroacoustics Conference*. June 2010. DOI: 10.2514/6.2010-3913. URL: https://arc.aiaa.org/doi/abs/10.2514/6.2010-3913.

[15] R.C. van der Grift et al. “Aircraft Noise Model Improvement by Calibration of Noise-Power-Distance Values Using Acoustic Measurements”. In: *30th AIAA/CEAS Aeroacoustics Conference (2024)*. AIAA, 2024. DOI: 10.2514/6.2024-3132. URL: https://arc.aiaa.org/doi/abs/10.2514/6.2024-3132.

[16] S. Ammar, C. Legros, and J. Trépanier. “Conceptual design, performance and stability analysis of a 200 passengers Blended Wing Body aircraft”. In: *Aerospace Science and Technology* 71 (2017), pp. 325–336. ISSN: 1270-9638. DOI: https://doi.org/10.1016/j.ast.2017.09.037. URL: https://www.sciencedirect.com/science/article/pii/S1270963816312640.

[17] E. Torenbeek. “Blended-wing-body aircraft: A historical perspective”. In: *Encyclopedia of Aerospace Engineering*. John Wiley & Sons, Ltd, 2016. Chap. 7, pp. 114–127. ISBN: 9780470686652. DOI: https://doi.org/10.1002/9780470686652.eae1003.

[18] J. Benad and R Vos. “Design of a Flying V Subsonic Transport”. In: *33rd ICAS Congress*. 2022. URL: https://resolver.tudelft.nl/uuid:95ea413d-d5b1-4cb2-a650-828cb106dbbd.

[19] NASA. *N3-X*. https://www.nasa.gov/eap-aircraft-concepts/n3-x/. Accessed: 08-07-2025.

[20] M.F. Liou et al. “Aerodynamic Design of the Hybrid Wing Body with Nacelle: N3-X Propulsion-Airframe Configuration”. In: *34th AIAA Applied Aerodynamics Conference*. American Institute of Aeronautics and Astronautics, 2016. DOI: 10.2514/6.2016-3875. URL: https://doi-org.tudelft.idm.oclc.org/10.2514/6.2016-3875.

[21] J.L. Felder, M. Tong, and L. Chu. “Sensitivity of Mission Energy Consumption to Turboelectric Distributed Propulsion Design Assumptions on the N3-X Hybrid Wing Body Aircraft”. In: *48th AIAA/ASME/SAE/ASEE Joint Propulsion Conference & Exhibit*. July 2012. DOI: 10.2514/6.2012-3701. URL: https://arc.aiaa.org/doi/abs/10.2514/6.2012-3701.

[22] J.L. Felder et al. “Turboelectric Distributed Propulsion in a Hybrid Wing Body Aircraft”. In: *20th International Society for Airbreathing Engines (ISABE) Conference*. Sept. 2011. DOI: ISABE-2011-1340.

[23] R. H. Liebeck. “Design of the Blended Wing Body Subsonic Transport”. In: *Journal of Aircraft* 41.1 (2004), pp. 10–25. DOI: 10.2514/1.9084. URL: https://doi.org/10.2514/1.9084.

[24] P. Okonkwo and H. Smith. “Review of evolving trends in blended wing body aircraft design”. In: *Progress in Aerospace Sciences* 82 (Feb. 2016). DOI: 10.1016/j.paerosci.2015.12.002.

[25] J. Trac-Pho. “Conceptual Design of a Blended Wing Body Airliner”. MA thesis. San José State University, 2022. URL: https://www.sjsu.edu/ae/docs/project-thesis/Jeffrey.Trac-Pho-F22.pdf.

[26] M. Voskuijl, G. La Rocca, and F. Dircken. “Controllability of Blended Wing Body Aircraft”. In: *Proceedings of the 26th International Congress of the Aronautical Sciences, ICAS 2008, including the 8th AIAA Aviation Technology, Integration and Operations (AIO) Conference, Anchorage, Alaska, September 14-19, (2008)* 5 (Jan. 2008).

[27] L. Lv. “Theoretical and Experimental Investigation of Boundary Layer Ingestion for Aircraft Application”. PhD thesis. Delft University of Technology, 2019. DOI: https://doi.org/10.4233/uuid:6d8bd168-e057-4ee9-854c-32c84015e4c4.

[28] Florence V. Hutcheson et al. “Shielding of Turbomachinery Broadband Noise from a Hybrid wing Body Aircraft Configuration”. In: *20th AIAA/CEAS Aeroacoustics Conference*. American Institute of Aeronautics and Astronautics, 2014. DOI: 10.2514/6.2014-2624. URL: https://arc.aiaa.org/doi/abs/10.2514/6.2014-2624.

[29] Shanling Yang, Mark Page, and Ed Smetak. “Achievement of NASA New Aviation Horizons N+2 Goals with a Blended-Wing-Body X-Plane Designed for the Regional Jet and Single-Aisle Jet Markets”. In: *2018 AIAA Aerospace Sciences Meeting*. Jan. 2018. DOI: 10.2514/6.2018-0521.

[30] I. Legriffon et al. “Flyover noise evaluation of low-noise technologies applied to a blended wing body aircraft”. In: *Inter Noise 2022*. Sept. 2022. DOI: 10.25144/14610.

[31] ARTEM consortium. *Research Project ARTEM*. Accessed 01-02-2026. URL: https://www.dlr.de/en/at/research-transfer/projects/artem.

[32] AirFrance. *Our Airbus A320 et A321*. Accessed 03-04-2026. URL: https://wwws.airfrance.nl/information/prepare/nos-avions/a320-a321.

[33] A.E. Vieira et al. “Comparison of Semi-Empirical Noise Models with Flyover Measurements of Operating Aircraft”. In: *Journal of Aircraft* 59.6 (June 2022), pp. 1574–1587. DOI: 10.2514/1.C036387.

[34] R. Martinez-Val, E. Perez, and J. Palacin. “Historical Perspective of Air Transport Productivity and Efficiency”. In: *43rd AIAA Aerospace Sciences Meeting and Exhibit*. AIAA, 2005. DOI: 10.2514/6.2005-121. URL: https://arc.aiaa.org/doi/abs/10.2514/6.2005-121.

[35] Airbus. *AIRCRAFT CHARACTERISTICS AIRPORT AND MAINTENANCE PLANNING*. Tech. rep. Revision No. 41 - Mar 01/22. Airbus, 2022. URL: https://www.aircraft.airbus.com/sites/g/files/jlcbta126/files/2023-02/Airbus-techdata-AC_A320_0322.pdf.

[36] D.G. Simons and M. Snellen. *Aircraft Noise - An introduction to general acoustics and aircraft noise*. TU Delft, 2023.

[37] B. von den Hoff. “Noise emissions and annoyance of sustainable aviation systems: Identifying noise sources and validating noise prediction models”. PhD thesis. Delft University of Technology, 2025. DOI: https://doi.org/10.4233/uuid:e97e1d99-11f0-46f3-9be9-2f8eeddde3bc.

[38] L. Bertsch, D.G. Simons, and M. Snellen. *Aircraft Noise: The major sources, modelling capabilities, and reduction possibilities*. Tech. rep. DLR & TU Delft, 2015. URL: https://elib.dlr.de/95939/.

[39] F. Petrosino and M. Barbarino. “Survey of Semi-Empirical Jet Noise Models for Preliminary Aircraft Engine Design”. In: *Aerospace* 10 (July 2023), p. 625. DOI: 10.3390/aerospace10070625.

[40] International Civil Aviation Organization. *Environmental Technical Manual, Volume I: Procedures for the Noise Certification of Aircraft*. Tech. rep. ICAO Doc 9501, Order Number: 9501-1. Montréal, Canada: International Civil Aviation Organization, 2018.

[41] L.S. Hultgren. *Semi-Empirical Modeling and Prediction of Direct Combustor Noise*. eng. NASA Report. 2018.

[42] SAE. *Procedure for the Calculation of Airplane Noise in the Vicinity of Airports*. Tech. rep. SAE AIR1845A. SAE Aeropspace, 2012. DOI: https://doi.org/10.4271/AIR1845A.

[43] SAE Aerospace. *Standard Values of Atmospheric Absorption as a Function of Temperature and Humidity*. Tech. rep. SAE ARP886B. SAE International Group, 2012.

[44] International Civil Aviation Organization. *Annex 16 to the Convention on International Civil Aviation, Environmental Protection, Volume I - Aircraft Noise*. 2017.

[45] G.S. Hreinsson. *Aircraft Noise*. Virginia Polytechnic Institute and State University, 1993. URL: https://archive.aoe.vt.edu/mason/Mason_f/HreinssonACNoise.pdf.

[46] Federal Aviation Administration. *New York/New Jersey/Philadelphia Metropolitan Area Airspace Redesign: Final Environmental Impact Statement (FEIS), Volume I*. Tech. rep. Federal Aviation Administration, 2007. URL: https://www.faa.gov/sites/faa.gov/files/air_traffic/nas/nynjphl_redesign/documentation/FEIS-VolumeOne.pdf.

[47] L. Rego et al. “Jet-installation noise and near-field characteristics of jet–surface interaction”. In: *Journal of Fluid Mechanics* 895 (2020). DOI: 10.1017/jfm.2020.294.

[48] F. Centracchio et al. “Noise shielding models for the conceptual design of unconventional aircraft”. In: *INTER-NOISE and NOISE-CON Congress and Conference Proceedings, Internoise 2018*. Aug. 2018.

[49] Z. Maekawa. “Noise reduction by screens”. In: *Applied Acoustics* 1.3 (1968), pp. 157–173. ISSN: 0003-682X. DOI: https://doi.org/10.1016/0003-682X(68)90020-0. URL: https://www.sciencedirect.com/science/article/pii/0003682X68900200.

[50] J.B. Keller. “Geometrical Theory of Diffraction”. In: *Journal of the Optical Society of America* 52 (2 1962), pp. 116–130.

[51] A.E.A. Vieira. “Improving Capabilities in Modeling Aircraft Noise Sources”. PhD thesis. Delft University of Technology, 2021. DOI: https://doi.org/10.4233/uuid:806e1965-8320-4a40-b0fc-0b060ac62799. URL: https://resolver.tudelft.nl/uuid:806e1965-8320-4a40-b0fc-0b060ac62799.

[52] M. van Ieperen. “Noise Prediction of the Flying V”. MA thesis. Delft University of Technology, 2021. URL: https://resolver.tudelft.nl/uuid:1697f11f-4b01-49d2-9cf8-9006dfdd4b57.

[53] C. Burley et al. “Noise Scaling and Community Noise Metrics for the Hybrid Wing Body Aircraft”. In: *20th AIAA/CEAS Aeroacoustics Conference*. June 2014. DOI: 10.2514/6.2014-2626.

[54] Airbus. *A320 family*. Accessed: 05/04/2026. URL: https://www.aircraft.airbus.com/en/aircraft/a320-family/a320neo.

[55] Airbus. Accessed 22-04-2026. URL: https://www.aircraft.airbus.com/en/aircraft/a330/a330-300.

[56] Boeing. Accessed 29-04-2026. URL: https://www.boeing.com/content/dam/boeing/boeingdotcom/company/about_bca/startup/pdf/historical/777_passenger.pdf.

[57] EUROCONTROL. Accessed 29-04-2026. URL: https://learningzone.eurocontrol.int/ilp/customs/ATCPFDB/default.aspx?GroupFilter=3.

[58] U. Michel. “Correlation of aircraft certification noise levels EPNL with controlling physical parameters”. In: *19th AIAA/CEAS Aeroacoustics Conference*. May 2013. ISBN: 978-1-62410-213-4. DOI: 10.2514/6.2013-2014.

[59] L.V. Lopes and C.L. Burley. *ANOPP2 User’s Manual*. NASA/TM–2016–219342. Oct. 2016.

[60] European Unioin Aviation Safety Agency. *TYPE-CERTIFICATE DATA SHEET FOR NOISE - No. EASA.A.064.3 for Airbus A320*. Tech. rep. TCDSN No.: EASA.A.064.3 issue: 28. EASA, 2020.

[61] European Unioin Aviation Safety Agency. *TYPE-CERTIFICATE DATA SHEET FOR NOISE - No. EASA.A.151 for Airbus A350*. Tech. rep. TCDSN No.: EASA.A.151 issue: 30. EASA, 2025.

[62] European Aviation Safety Agency. *TYPE-CERTIFICATE DATA SHEET FOR NOISE - No. EASA.IM.A.003 for Boeing 777*. TCDSN No.: EASA.IM.A.003 issue:24. 2021.

[63] European Unioin Aviation Safety Agency. *TYPE-CERTIFICATE DATA SHEET FOR NOISE - No. EASA.A.004 for Airbus A330*. Tech. rep. TCDSN No.: EASA.A.004 issue: 46. EASA, 2025.

[64] Aircraft Commerce. Issue 87, Accessed 29-04-2026. 2013. URL: https://www.aircraft-commerce.com/wp-content/uploads/aircraft-commerce-docs/Developments/2013/ISSUE%2087_DEVELOP.pdf.

[65] EASE. *ANP legacy data*. URL: https://www.easa.europa.eu/en/domains/environment/policy-support-and-research/aircraft-noise-and-performance-anp-data/anp-legacy-data.

[66] D. Lee and H. Sung. “Performance Design of a Turbofan Engine Using Multi-objective Particle Swarm Optimization (MOPSO)”. In: *Int. J. Aeronaut. Space Sci.* 23 (2022), pp. 533–545. URL: https://doi-org.tudelft.idm.oclc.org/10.1007/s42405-022-00451-w.

[67] M. Koch and L. Bertsch. “Engine Noise Source Placement for Shielding Calculation”. In: *Inter-noise 2019: Madrid, Spain*. June 2019.

[68] M.F. Heidmann. *Interim Predictoin Method for Fan and Compressor Source Noise*. NASA Technical Memorandum X-71763. Lewis Research Center, NASA, 1979.

[69] A. Sahai. “Consideration of aircraft noise annoyance during conceptual aircraft design”. PhD thesis. RWTH AAchen University, June 2016. URL: https://publications.rwth-aachen.de/record/668901/files/668901.pdf.

[70] K.B. Kontos, B.A. Janardan, and P.R. Gliebe. *Improved NASA-ANOPP Noise PredictionComputer Code for Advanced Subsonic Propulsion Systems*. Volume 1: ANOPP Evaluation and Fan Noise Model Improvement. Lewis Research Center, NASA, 1996.

[71] L. S. Hultgren. “A Comparison of Combustor-Noise Models”. In: *18th AIAA/CEAS Aeroacoustics Conference (33rd AIAA Aeroacoustics Conference)* (2012). DOI: 10.2514/6.2012-2087.

[72] Society of Automotive Engineers International. *Gas Turbine Jet Exhaust Noise Prediction*. Technical Standard SAE ARP876 Rev. F. 2021.

[73] P. Ho and V. Doyle. “Combustion noise prediction update”. In: *5th Aeroacoustics Conference*. Mar. 1979. DOI: 10.2514/6.1979-588. URL: https://arc.aiaa.org/doi/abs/10.2514/6.1979-588.

[74] J.R. Stone. *Interim Prediction Method for Jet Noise*. Tech. rep. NASA TM X-71618. NASA Lewis Research Center, 1974.

[75] J.R. Stone and F.J. Montegani. “An improved prediction method for the noise generated in flight by circular jets”. In: *The Journal of the Acoustical Society of America* 67 (Apr. 1980), S4. DOI: 10.1121/1.2018248.

[76] J.R. Stone, D.E. Groesbeck, and C.L. Zola. “Conventional profile coaxial jet noise prediction”. In: *AIAA Journal* 21.3 (1983), pp. 336–342. DOI: 10.2514/3.8077. URL: https://doi.org/10.2514/3.8077.

[77] J.R. Stone et al. *Jet Noise Modeling for Suppressed and Unsuppressed Aircraft in Simulated Flight*. Tech. rep. NASA/TM—2009-215524. NASA Glenn Research Center, 2009.

[78] W.P.J. Visser. “Generic Analysis Methods for Gas Turbine Engine Performance”. PhD thesis. Delft University of Technology, 2015. URL: https://doi.org/10.4233/uuid:f95da308-e7ef-47de-abf2-aedbfa30cf63.

[79] M.R. Fink. *Airframe Noise Prediction Method*. Tech. rep. prepared for Federal Aviation Administration, FAA-RD-77-29. United States Research Center, Mar. 1977.

[80] W.E. Zorumski. *Aircraft Noise Prediction Program Theoretical Manual, part 2*. NASA-TM-83199-PT-2. Langley Research Center, NASA, 1982.

[81] V. Jazarevic and B. Rašuo. “Numerical Calculation of Aerodynamic Noise Generated from an Aircraft in Low Mach Number Flight”. In: *Boundary and Interior Layers, Computational and Asymptotic Methods - BAIL 2016* (2017). Lecture Notes in Computational Science and Engineering. URL: https://doi.org/10.1007/978-3-319-67202-1.

[82] Y. Guo et al. “Hybrid Wing Body (HWB) Slat Noise Analysis”. In: *51st AIAA Aerospace Sciences Meeting including the New Horizons Forum and Aerospace Exposition*. Jan. 2013. DOI: 10.2514/6.2013-462. URL: https://arc.aiaa.org/doi/abs/10.2514/6.2013-462.

[83] M. Arntzen. “Aircraft noise calculation and synthesis in a non-standard atmosphere”. PhD thesis. Delft University of Technology, 2014. URL: https://doi.org/10.4233/uuid:c56e213c-82db-423d-a5bd-503554653413.

[84] Engineering Sciences Data Unit. *Prediction of noise generated by fans and compressors in turbojet and turbofan engines*. Technical Report 98008. 2011.

[85] Engineering Sciences Data Unit. *Prediction of combustor noise from gas turbine engines*. Technical Report 05001. 2010.

[86] Engineering Sciences Data Unit. *Airframe noise prediction*. Technical Report 90023. 2008.

[87] Aircraft Commerce. “A321neo and narrowbody fuel burn and operating performance”. In: *Aircraft Commerce* 123 (2019). URL: https://www.aircraft-commerce.com/wp-content/uploads/aircraft-commerce-docs/General%20Articles/2019/123_FLTOPS_A.pdf.

[88] European Union Aviation Safety Agency. *TYPE-CERTIFICATE DATA SHEET No. E.003 for CFM56□5B and CFM56□5C series engines*. TCDS No.: E.003 Issue: 066. Jan. 2023.

[89] J. Buchwald and C. Yeang. “Kirchhoff’s Theory for Optical Diffraction, Its Predecessor and Subsequent Development: The Resilience of an Inconsistent Theory”. In: *Archive for History of Exact Sciences* 70 (Feb. 2016), pp. 463–511.

[90] L. W. Ng and Z. S. Spakovszky. “Turbomachinery noise shielding assessment of advanced aircraft configurations”. In: *16th AIAA/CEAS Aeroacoustics Conference* (2010). DOI: 10.2514/6.2010-3914.

[91] M. Lummer. “Maggi-Rubinowicz Diffraction Correction for Ray-Tracing Calculations of Engine Noise Shielding”. In: *14th AIAA/CEAS Aeroacoustics Conference (29th AIAA Aeroacoustics Conference)*. May 2008. DOI: 10.2514/6.2008-3050. URL: https://arc.aiaa.org/doi/abs/10.2514/6.2008-3050.

[92] A.E. Alves Vieira, M. Snellen, and D.G. Simons. “Assessment of engine noise shielding by the wings of current turbofan aircraft”. In: *24th International Congress on Sound and Vibration: London calling 2017* (2017).

[93] K. Miyamoto and E. Wolf. “Generalization of the Maggi-Rubinowicz Theory of the Boundary Diffraction Wave—Part I”. In: *Journal of the Optical Society of America* 52 (June 1962), pp. 615–625. DOI: 10.1364/JOSA.52.000615.

[94] Y. Umul. “Modified theory of physical optics”. In: *Optics Express* 12 (Oct. 2004), pp. 4959–4972. DOI: 10.1364/OPEX.12.004959.

[95] D.P. Hewett. “Tangent ray diffraction and the Pekeris caret function”. In: *Wave Motion* 57 (2015), pp. 257–267. ISSN: 0165-2125. DOI: https://doi.org/10.1016/j.wavemoti.2015.05.003. URL: https://www.sciencedirect.com/science/article/pii/S0165212515000712.

[96] A. Kirpichnikova and N. Kirpichnikova. *Matching creeping waves with lit area diffraction field*. DAYS on DIFFRACTION 2021. 2021. DOI: https://doi.org/10.1109/DD52349.2021.9598659.

[97] I.V. Andronov and D. Bouche. “On the degeneration of creeping waves in a vicinity of critical values of the impedance”. In: *Wave Motion* 45.4 (2008), pp. 400–411. ISSN: 0165-2125. DOI: https://doi.org/10.1016/j.wavemoti.2007.09.009. URL: https://www.sciencedirect.com/science/article/pii/S0165212507000972.

[98] F. Yunus et al. “Efficient prediction of urban air mobility noise in a vertiport environment”. In: *Aerospace Science and Technology* 139 (2023), p. 108410. ISSN: 1270-9638. DOI: https://doi.org/10.1016/j.ast.2023.108410. URL: https://www.sciencedirect.com/science/article/pii/S1270963823003073.

[99] F.P. Adamo and M. Barbarino et al. “Aeroacoustic assessment of blended wing body configuration with low noise technologies”. In: *Materials Research Proceedings*. Vol. 37. 2023. DOI: https://doi.org/10.21741/9781644902813-1.

[100] A. P. Synodinos, R. H. Self, and A. J. Torija. “Framework for Predicting Noise–Power–Distance Curves for Novel Aircraft Designs”. In: *Journal of Aircraft* 55.2 (2018), pp. 781–791. DOI: 10.2514/1.C034466. URL: https://doi.org/10.2514/1.C034466.

[101] D.E. Bishop, J.M. Beckmann, and M.P. Bucka. *Revision of Civil Aircraft Noise Data for the Integrated Noise Model (INM)*. Tech. rep. for the Transportation System Center, Department of Transportation. BBN Laboratories Incorerated, Sept. 1986.

[102] G.J.J. Ruijgrok. *Elements of airplane performance*. 6th ed. Delft Academic Press, 2013. ISBN: 978-90-6562-204-4.

[103] European Union Aviation Safety Agency. *TYPE-CERTIFICATE DATA SHEET No. IM.E.002 for GE90 Series Engines*. TCDS No.: IM.E.002 issue 05. Mar. 2023.

[104] F.M. Rebello da Silva et al. “Flap Optimatization for Take-off and Landing”. In: *Proceedings of the 10th Brazilian Congress of Thermal Sciences and Engineering - ENCIT 2004*. 2004.

[105] European Union Aviation Safety Agency. *TYPE-CERTIFICATE DATA SHEET EASA.IM.E.007 for CF6-80E1 series engines*. TCDS No.: IM.E.007 issue 03. July 2020.

[106] GE Aviation. Accessed 20-04-2026. URL: https://www.geaerospace.com/sites/default/files/datasheet-CF6-80E1.pdf.

[107] Accessed 20-04-2026. URL: https://www.aircraft.airbus.com/en/newsroom/stories/2024-02-airbus-to-introduce-a330neo-takeoff-performance-enhancements.

[108] R. van der Grift. “Flight profile points Schipfol Airport”. Unpublished ANP flight profile points data for Schiphol Airport.

[109] European Committee. *BESLUIT (EU) 2025/519 VAN DE COMMISSIE van 5 maart 2025 betreffende de procedure voor de invoering van exploitatiebeperkingen op de luchthaven Schiphol overeenkomstig Verordening (EU) nr. 598/2014 van het Europees Parlement en de Raad*. C(2025) 1355. Mar. 2025.

[110] F. Hoyas. "Skyward Action - Realizing Aviation's Sustainable Future". In: 2025 Environmental Report. ICAO, 2025. Chap. 10. URL: https://www.icao.int/sites/default/files/environmental-protection/Documents/EnvironmentalReports/2025/ICAO-EnvReport-2025.pdf.

[111] Advanced Decision Systems Adecs Airinfra Consultants BV. *Contra-expertise Gebruiksprognose Schiphol 2020*. Tech. rep. Ministerie van Infrastructuur en Waterstaat, Oct. 2019. URL: https://www.eerstekamer.nl/overig/20191118/contra_expertise_gebruiksprognose/document.

[112] Airbus. *A318/A319/A320/A321 Flight crew operating manual*. Accessed: 12-12-2025. 2017. URL: https://repo.poltekbangsby.ac.id/id/eprint/571/1/A318_A319_A320_A321%20%28%20PDFDrive%20%29.pdf.

[113] Airbus. *A319/A320/A321 Flight deck and systems briefing for pilots*. https://ads-b.ca/a320/A319-320-321_Flight_Deck_and_Systems_Briefing_for_Pilots.pdf. Accessed: 31-10-2025.

[114] LVNL. *Aeronautical Inoformation Publication*. AIRAC AMDT 10/2025. 2025. URL: https://eaip.lvnl.nl/web/eaip/AIRAC%20AMDT%2010-2025_2025_10_02/index.html.

[115] J. Roskam. *Airplane Design - Part I: Preliminary Sizing of Airplanes*. Design Analysis and Research Corporation, 1997. ISBN: 188488542X.

[116] R. Vos, J.A. Melkert, and B.T.C. Zanbergen. *A/C Preliminary Sizing (class I weight estimation method)*. part of Aerospace Design and Systems Engineering Elements I – Delft University of Technology, accessed on 28-11-2025. 2017.

[117] D.P. Raymer. *Aircraft Design: A Conceptual Approach*. 2nd ed. American Institute of Aeronautics and Astronautics, 1992. ISBN: 0-930403-51-7.

[118] L. Jenkinson, P Simpkin, and D. Rhodes. *Civil Jet Aircraft Design*. Appendix B: Engine Data File. URL: https://booksite.elsevier.com/9780340741528/appendices/data-b/default.htm.

[119] C.J. Bahr et al. "A Comparison of the Noise Characteristics of a Conventional Slat and Krueger Flap". In: *22nd AIAA/CEAS Aeroacoustics Conference*. American Institute of Aeronautics and Astronautics, 2016. DOI: 10.2514/6.2016-2961. URL: https://arc.aiaa.org/doi/abs/10.2514/6.2016-2961.

[120] Mitsuhiro Murayama et al. "Computational Study of Noise Characteristics From 30P30N Leading-Edge Slat and Krueger Flap". In: *30th AIAA/CEAS Aeroacoustics Conference (2024)*. American Institute of Aeronautics and Astronautics, 2024. DOI: 10.2514/6.2024-3284. URL: https://arc.aiaa.org/doi/abs/10.2514/6.2024-3284.

[121] M. Pott-Pollenske and J. Wild. "On the Noise Generation of Krueger Leading Edge Devices". In: *21st AIAA/CEAS Aeroacoustics Conference*. American Institute of Aeronautics and Astronautics, 2015. DOI: 10.2514/6.2015-3142. URL: https://arc.aiaa.org/doi/abs/10.2514/6.2015-3142.

[122] R. Vos and J.A. Melkert. *Wing Positioning, Landing Gear and Empennage Design*. part of Aerospace Design and Systems Engineering Elements I at Delft University of Technology, accessed 09-03-2026. 2019.

[123] Luchtverkeersleiding Nederland. *EHAM AD 2 - Amsterdam Airport Schiphol aerodome information*. Aeronautical Information Publication, accessed: 02-12-2026. 2026. URL: https://eaip.lvnl.nl/web/eaip/AIRAC%20AMDT%2001-2026_2026_01_22/eAIP/EH-AD%202%20EHAM%201-en-GB.html.

[124] E. Torenbeek. *Synthesis of Subsonic Airplane Design*. Springer Science+Business Media, B.V., 1982. ISBN: 978-90-481-8273-2.

[125] International Civil Aviation Organization. *Annex 16 to the Convention on International Civil Aviation, Environmental Protection, Volume II - Aircraft Engine Emissions*. 4th ed. International Civil Aviation Organization, 2017. ISBN: 978-92-9258-314-9.

A. Tone Correction for Perceived Noise Level

The tone correction C used in Equation 2.8 for L_{PN} is found using the following procedure:

1. For i as a 1/3 octave band number of 4 to 24 (100 Hz to 10 kHz), the change in SPL (ΔSPL) is

$$\Delta SPL(i) = SPL(i) - SPL(i-1) \tag{A.1}$$

   while for band number 3 (80 Hz), $\Delta SPL(3) = 0$.

2. If $|\Delta SPL| > 5$ dB, there are two options:
   - Encircle $SPL(i)$ if $\Delta SPL(i) > \Delta SPL(i-1)$ and $\Delta SPL(i) > 0$.
   - Encircle $SPL(i-1)$ if $\Delta SPL(i) \leq 0$ and $\delta SPL(i-1) > 0$

   For all encircled SPL compute the new SPL (SPL') with

$$SPL'(i) = 1/2[SPL(i-1) + SPL(i+1)] \tag{A.2}$$

   for SPL in bands 2 to 23. For band 24, use

$$SPL'(24) = SPL(23) + \Delta SPL(23)$$

   If $|\Delta SPL| \leq 5$, SPL' is found with

$$SPL'(i) = SPL(i). \tag{A.3}$$

3. Compute $\Delta SPL'$ using the new SPL' values with

$$\Delta SPL'(i) = SPL'(i) - SPL'(i-1) \tag{A.4}$$

   An imaginary 25th band is included using $\Delta SPL'(25) = \Delta SPL'(24)$. For band number 3, $\Delta SPL'(3) = \Delta SPL'(4)$ [45].

4. From band 3 to 23, compute the average of three adjacent steps of $\Delta SPL'$ using

$$\overline{\Delta SPL'}(i) = 1/3[\Delta SPL'(i) + \Delta SPL'(i+1) + \Delta SPL'(i+2)] \tag{A.5}$$

5. Compute the 1/3 octave band $SPL^{"}$ from band 3 to 24 with

$$\begin{gathered} SPL^{"}(3) = SPL(3) \\ SPL^{"}(i) = SPL^{"}(i-1) + \overline{\Delta SPL'}(i-1) \\ SPL^{"}(24) = SPL^{"}(23) + \overline{\Delta SPL'}(23) \end{gathered} \tag{A.6}$$

6. The difference F_{diff} between the original and final SPL is obtained by

$$F_{diff}(i) = SPL(i) - SPL^{"}(i) \tag{A.7}$$

   For all values where $F_{diff}(i) \geq 3$, find the tone correction factor C using Table A.1 [44].

Table A.1: Tone correction factor [45]

Frequency f [Hz]	**F$_{diff}$ [dB]**	**C [dB]**
$50 \leq f < 500$	$3 \leq F_{diff} < 20$	$F_{diff}/6$
	$20 \leq F_{diff}$	3.333
$500 \leq f < 5000$	$3 \leq F_{diff} < 20$	$F_{diff}/3$
	$20 \leq F_{diff}$	6.667
$f \geq 5000$	$3 \leq F_{diff} < 20$	$F_{diff}/6$
	$20 \leq F_{diff}$	3.333

7. The largest tone correction factor C is added to L_{PN} to obtain PNLT using Equation 2.8 [45].

B. Semi-empirical Model Comparison

B.1. Total aircraft noise

B.1.1. Departure

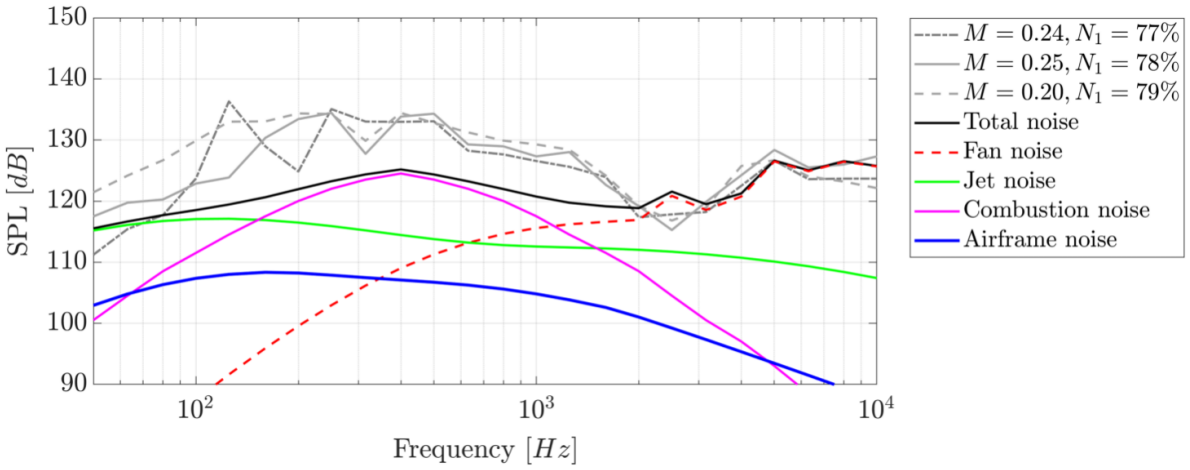

Figure B.1: Spectrum at θ = 90°, ϕ = 0° of a flyover during departure, obtained from [33]

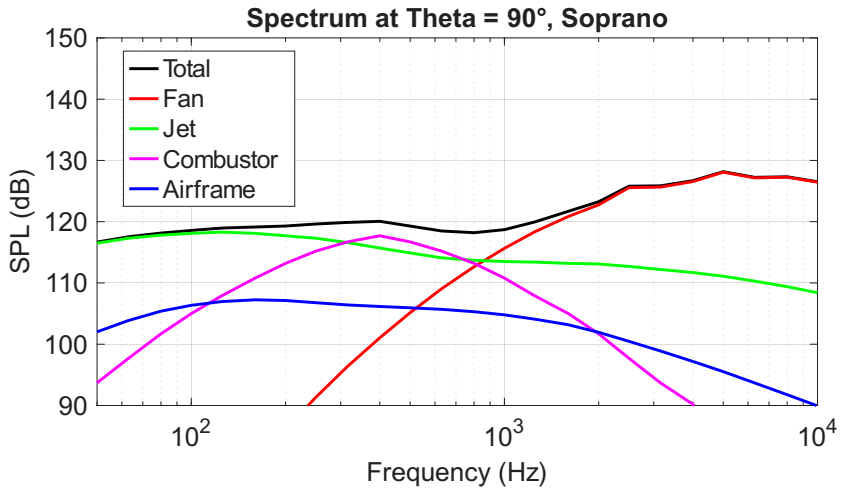

Figure B.2: Spectrum for a departing A320 using SOPRANO at θ = 90°, ϕ = 0°

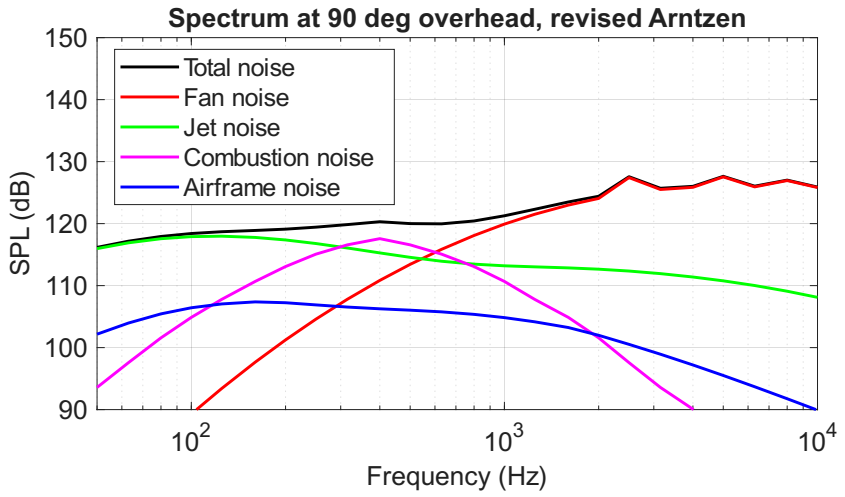

Figure B.3: Spectrum for a departing A320 using the revised model from Arntzen at θ = 90°, ϕ = 0°

B.1.2. Approach

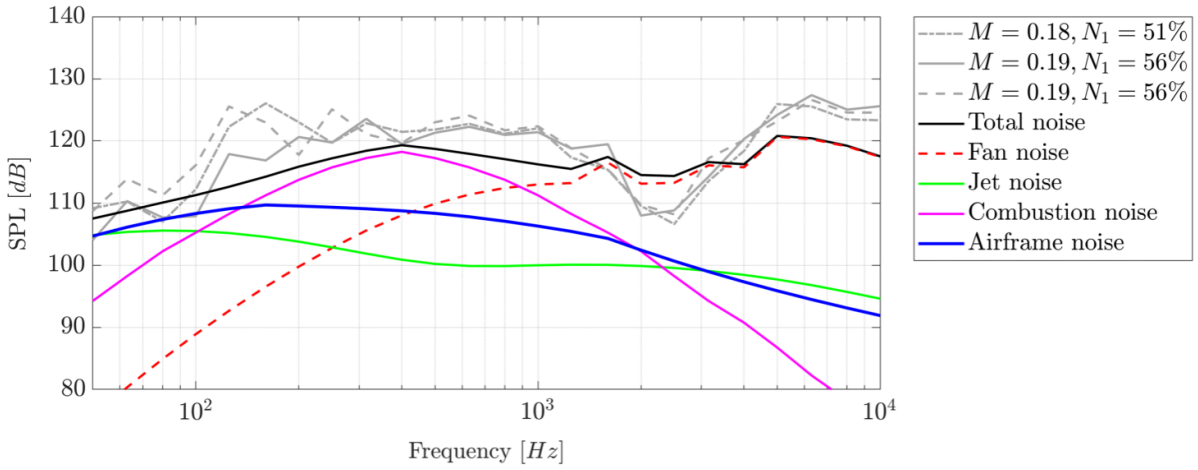

Figure B.4: Spectrum at θ = 90°, ϕ = 0° of a flyover during approach, obtained from [33]

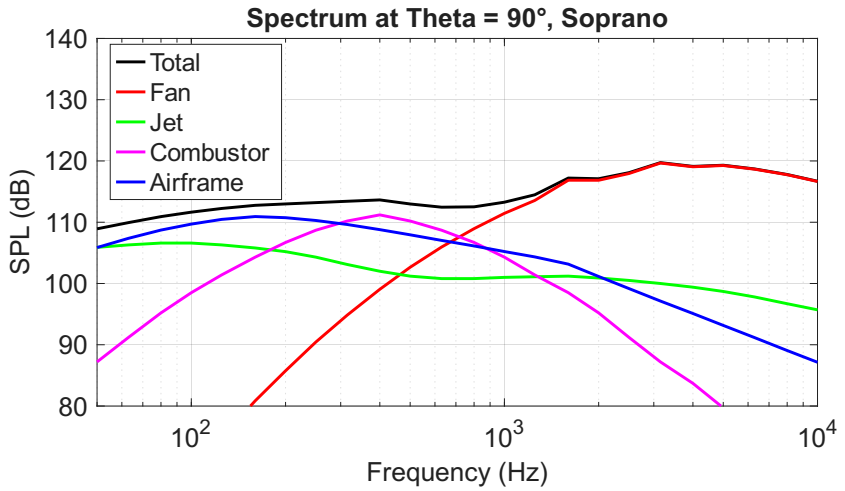

Figure B.5: Spectrum for an approach A320 using SOPRANO at θ = 90°, ϕ = 0°

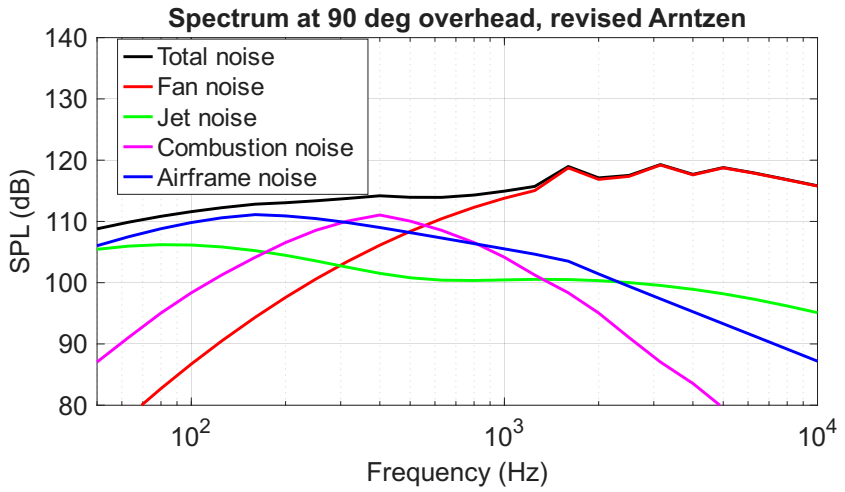

Figure B.6: Spectrum for an approaching A320 using the revised model from Arntzen at $\theta = 90°$, $\phi = 0°$

B.2. Airframe noise

B.2.1. Departure

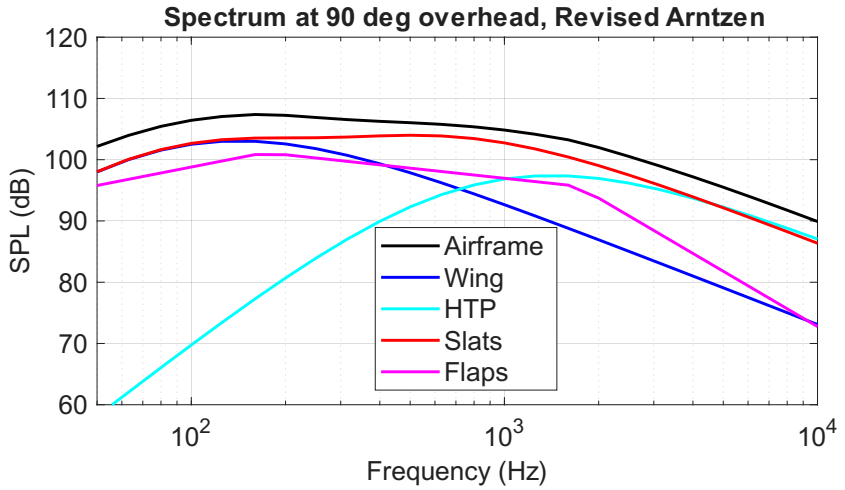

Figure B.7: Spectrum at $\theta = 90°$, $\phi = 0°$ of the airframe noise components during departure using a revised version of Arntzen's model

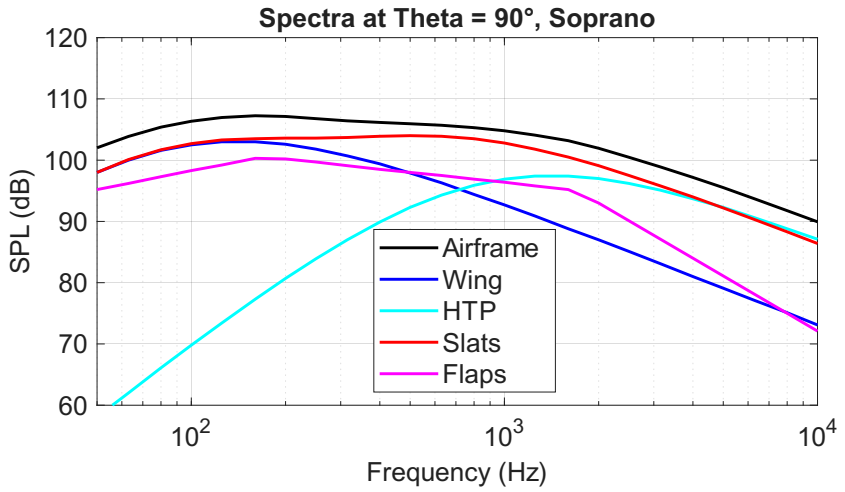

Figure B.8: Spectrum at $\theta = 90°$, $\phi = 0°$ of the airframe noise components during departure using SOPRANO

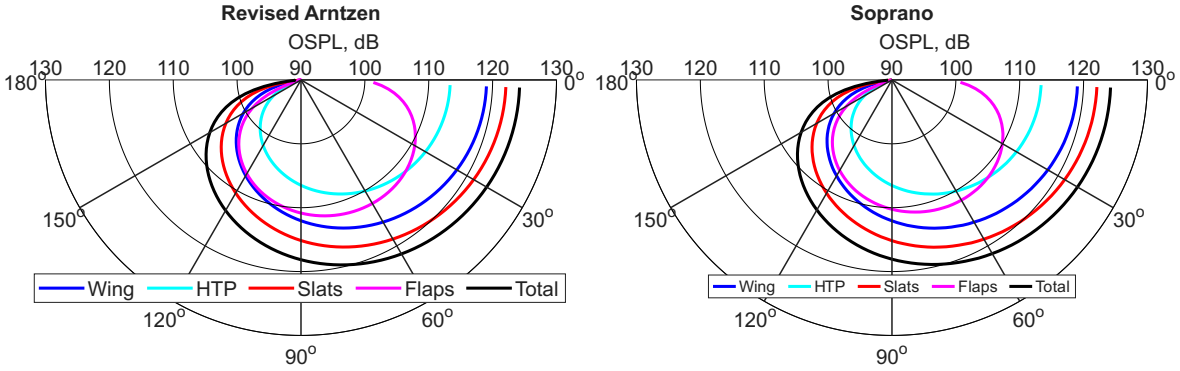

(a) Polar plot of the airframe noise components during departure using a revised version of Arntzen's model

(b) Polar plot of the airframe noise components during departure using SOPRANO

Figure B.9: Airframe noise polar plot comparison for departure

B.2.2. Arrival

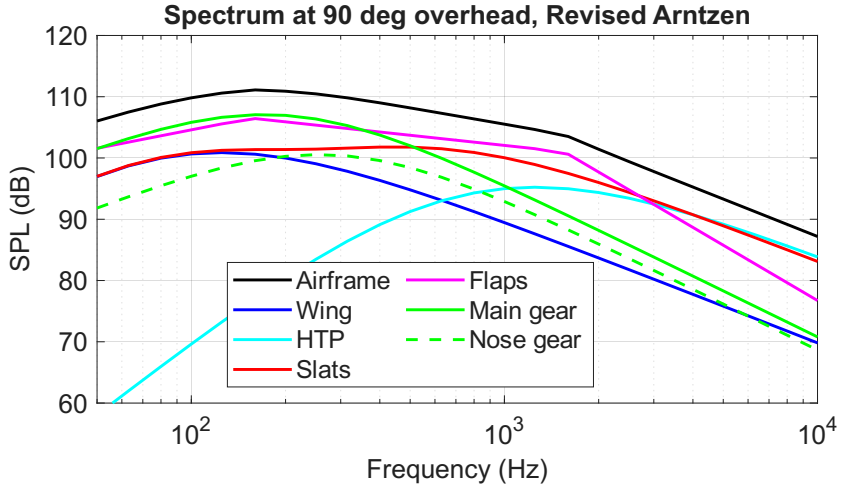

Figure B.10: Spectrum at $\theta = 90°$, $\phi = 0°$ of the airframe noise components during arrival using a revised version of Arntzen's model

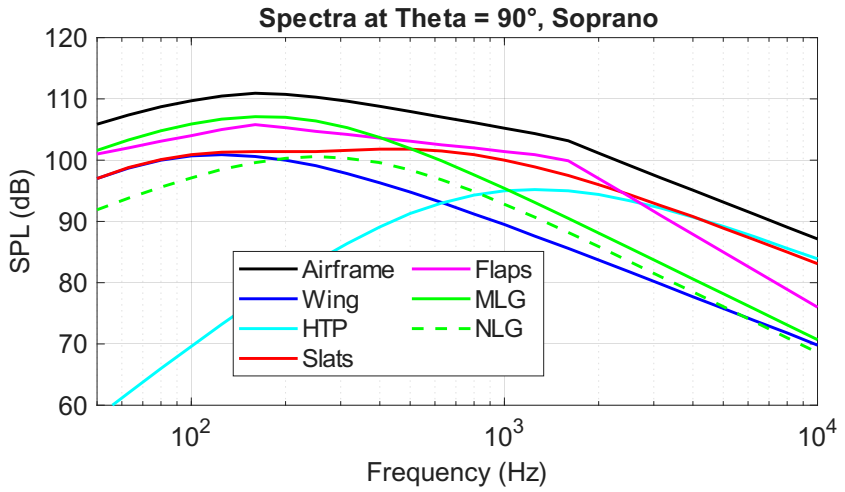

Figure B.11: Spectrum at $\theta = 90°$, $\phi = 0°$ of the airframe noise components during arrival using SOPRANO

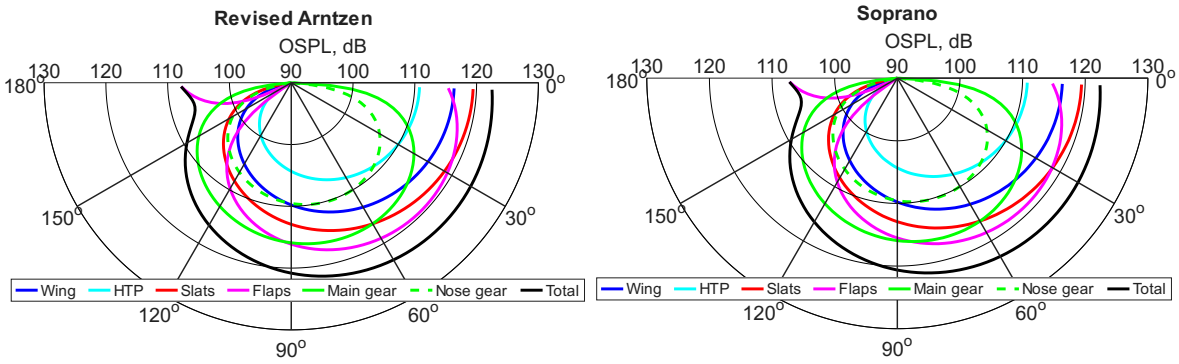

(a) Polar plot of the airframe noise components during arrival using a revised version of Arntzen's model

(b) Polar plot of the airframe noise components during arrival using SOPRANO

Figure B.12: Airframe noise polar plot comparison for approach

C. Noise-Power-Distance Tables Tube-and-Wing Aircraft

C.1. Airbus A320

C.1.1. Departure

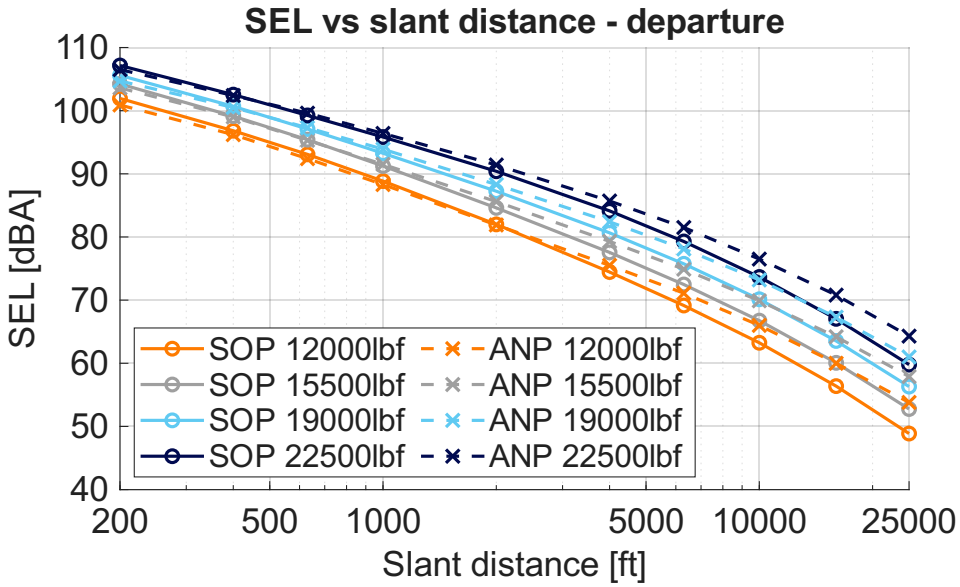

Figure C.1: NPD SEL results for a departing A320

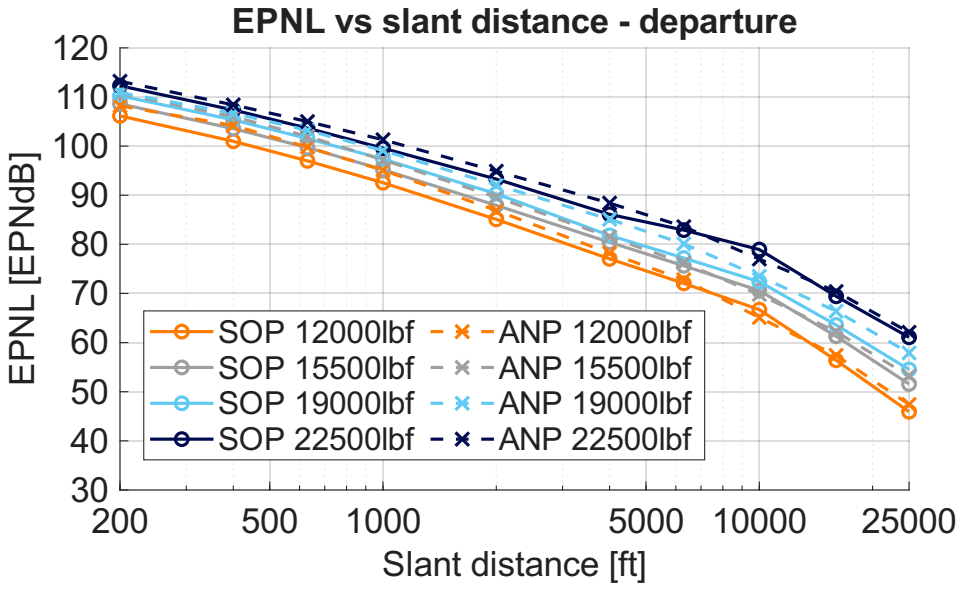

Figure C.2: NPD EPNL results for a departing A320

C.1.2. Approach

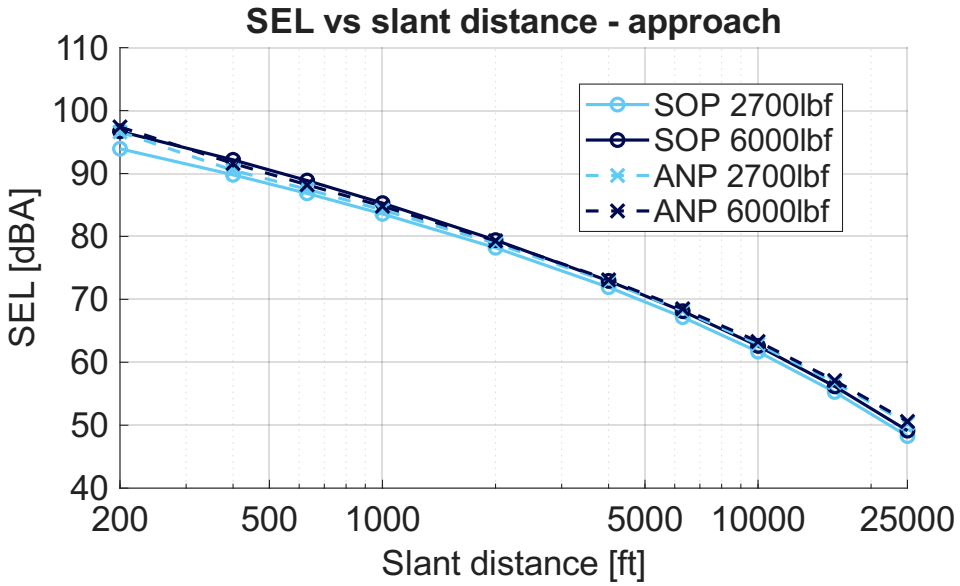

Figure C.3: NPD SEL results for an approaching A320

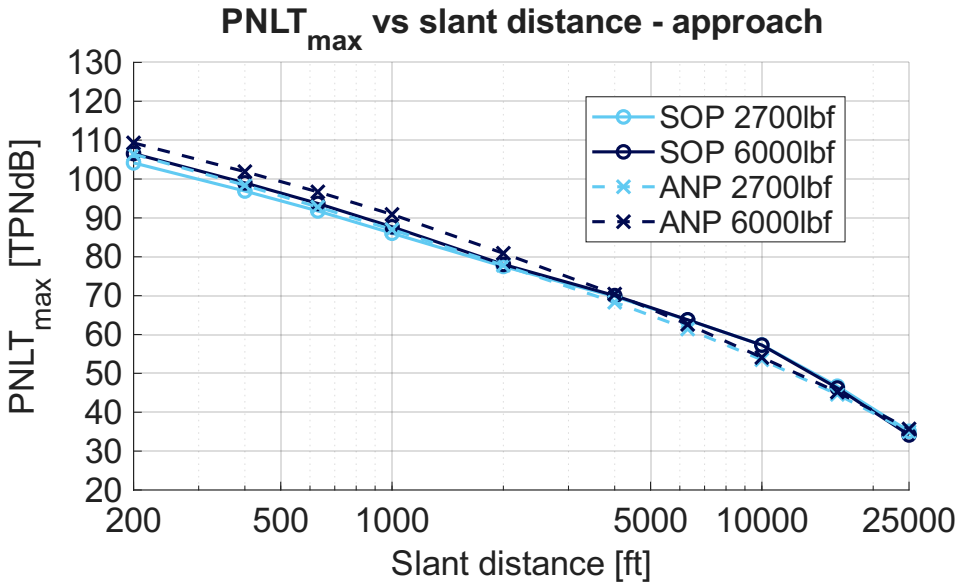

Figure C.4: NPD PNLT$_{max}$ results for an approaching A320

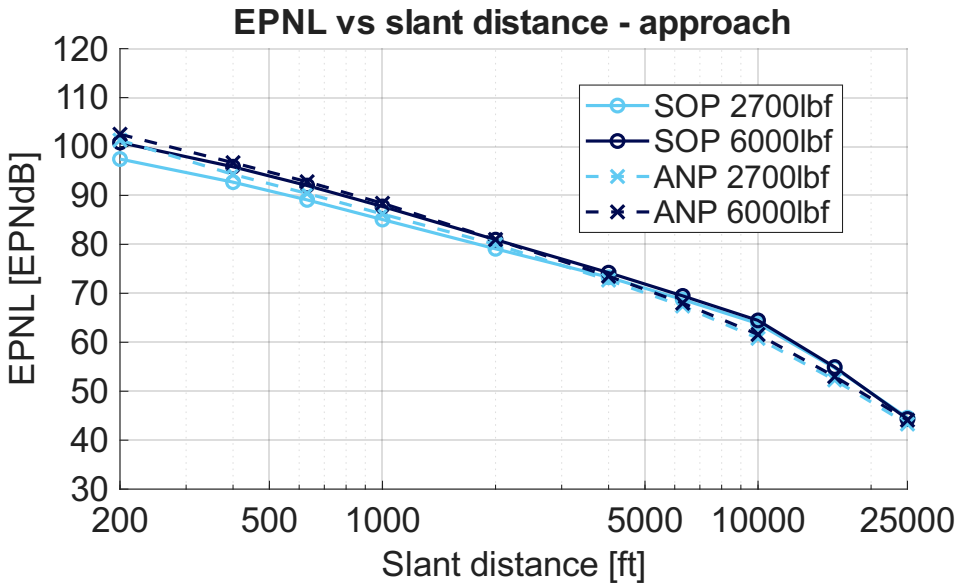

Figure C.5: NPD EPNL results for an approaching A320

C.2. Boeing 777

C.2.1. Departure

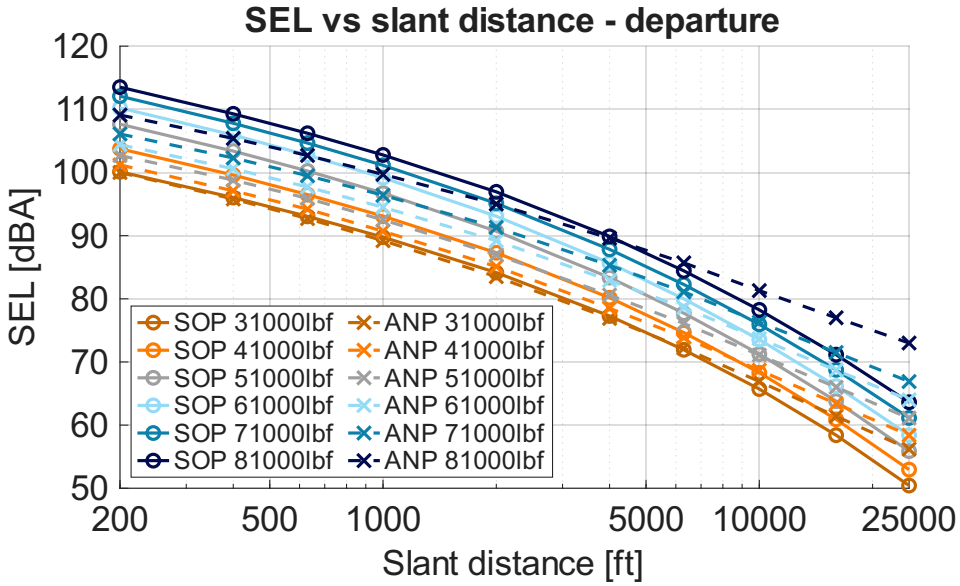

Figure C.6: NPD SEL results for a departing Boeing 777

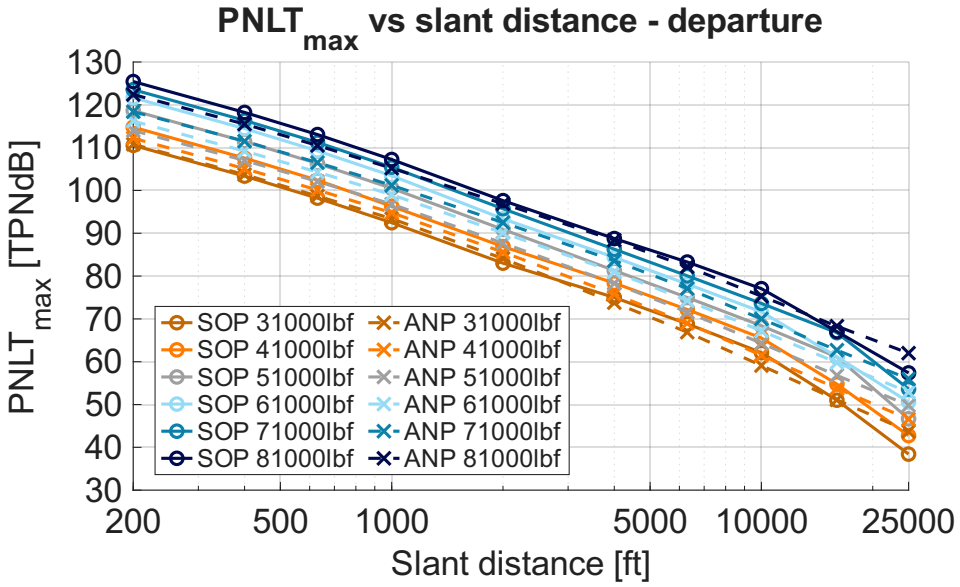

Figure C.7: NPD PNLT_{max} results for a departing Boeing 777

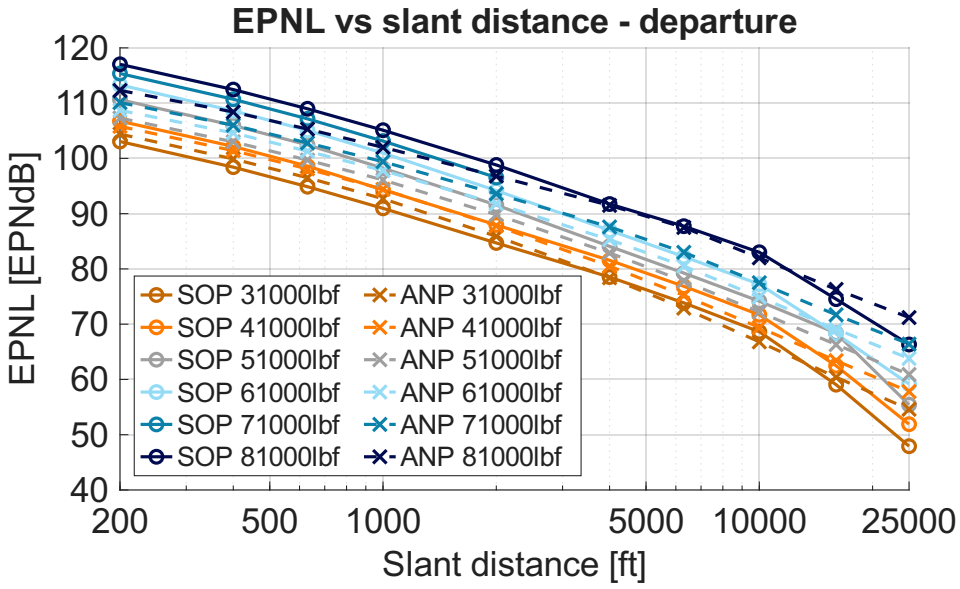

Figure C.8: NPD EPNL results for a departing Boeing 777

C.2.2. Approach

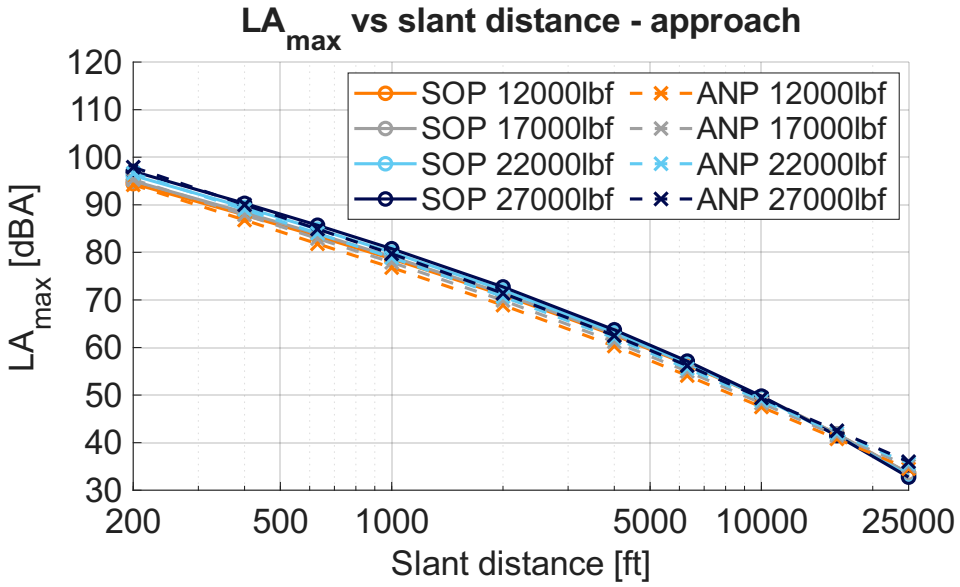

Figure C.9: NPD $L_{A_{max}}$ results for an approaching Boeing 777

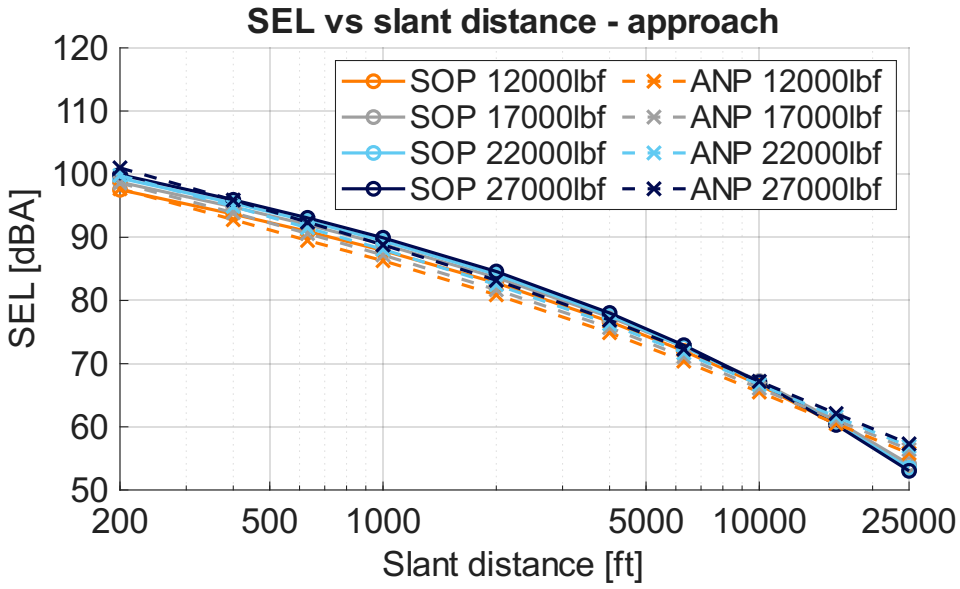

Figure C.10: NPD SEL results for an approaching Boeing 777

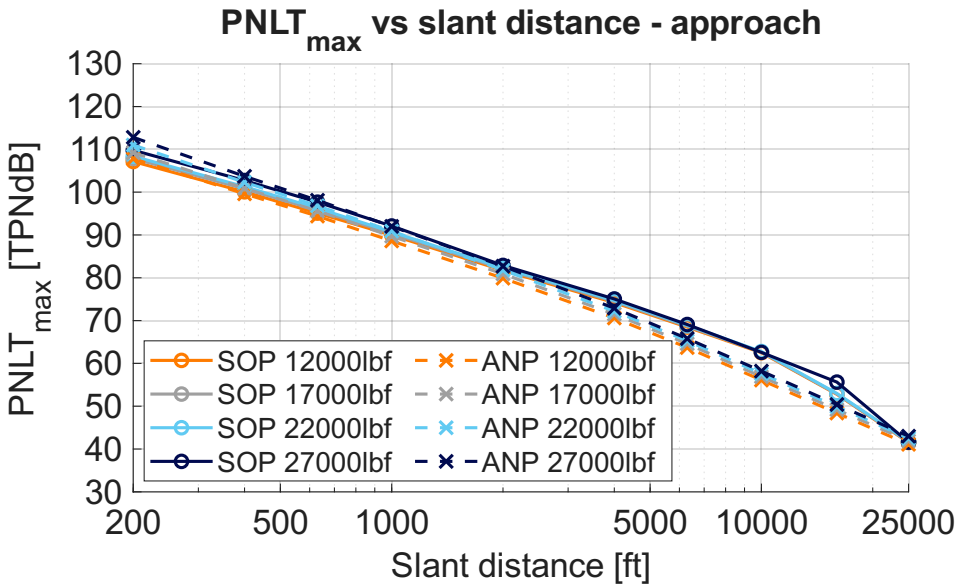

Figure C.11: NPD PNLT$_{max}$ results for an approaching Boeing 777

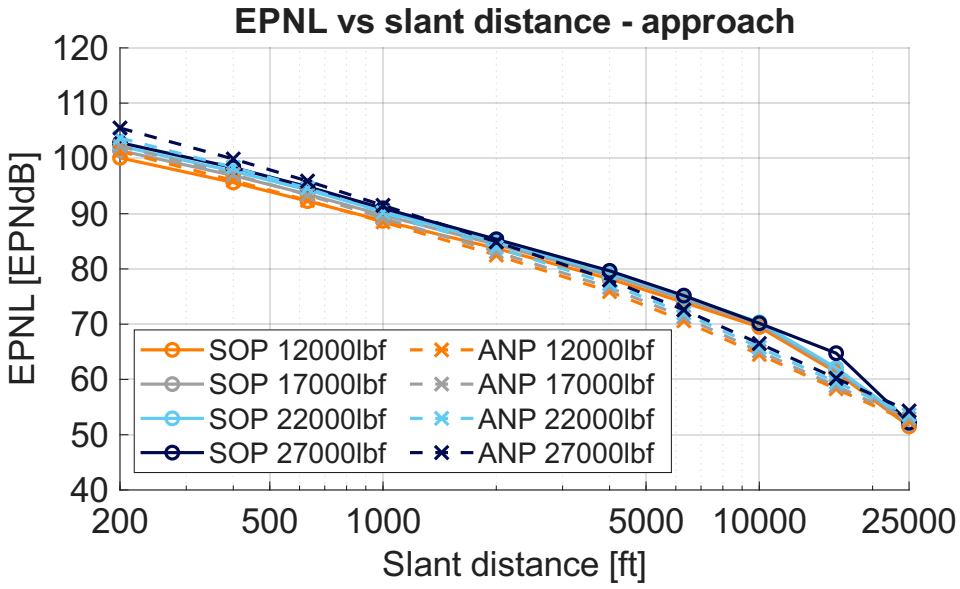

Figure C.12: NPD EPNL results for an approaching Boeing 777

C.3. Airbus A330

C.3.1. Departure

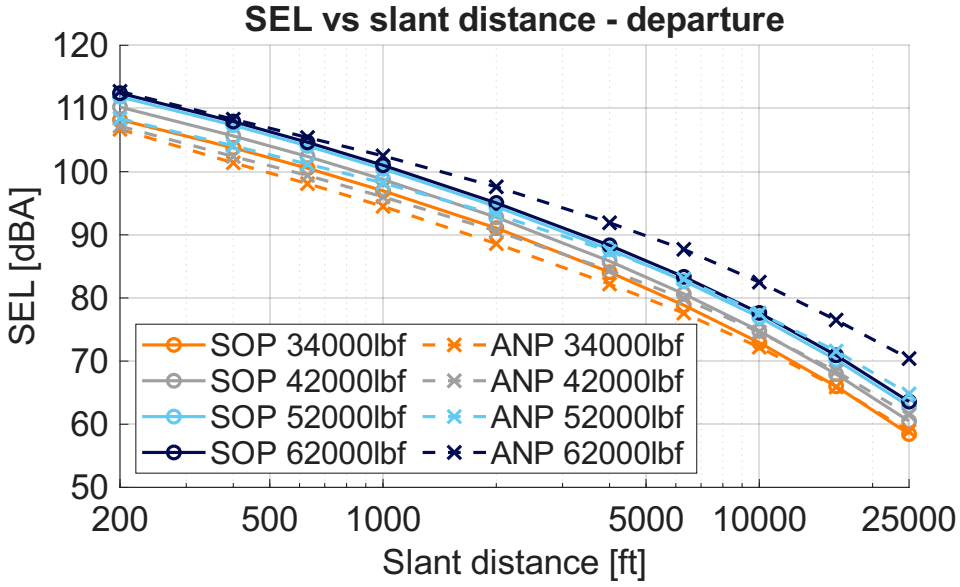

Figure C.13: NPD SEL results for a departing Airbus A330

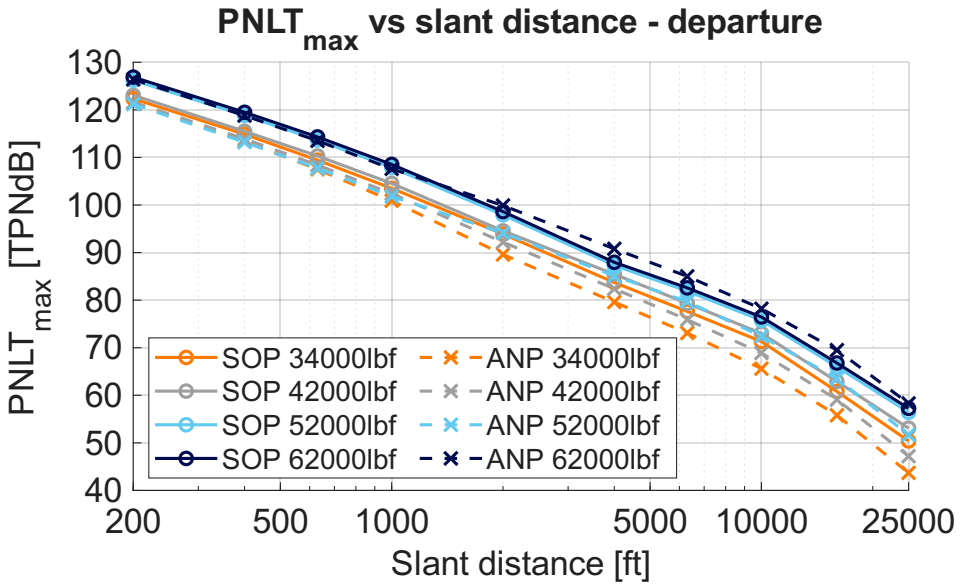

Figure C.14: NPD PNLT$_{max}$ results for a departing Airbus A330

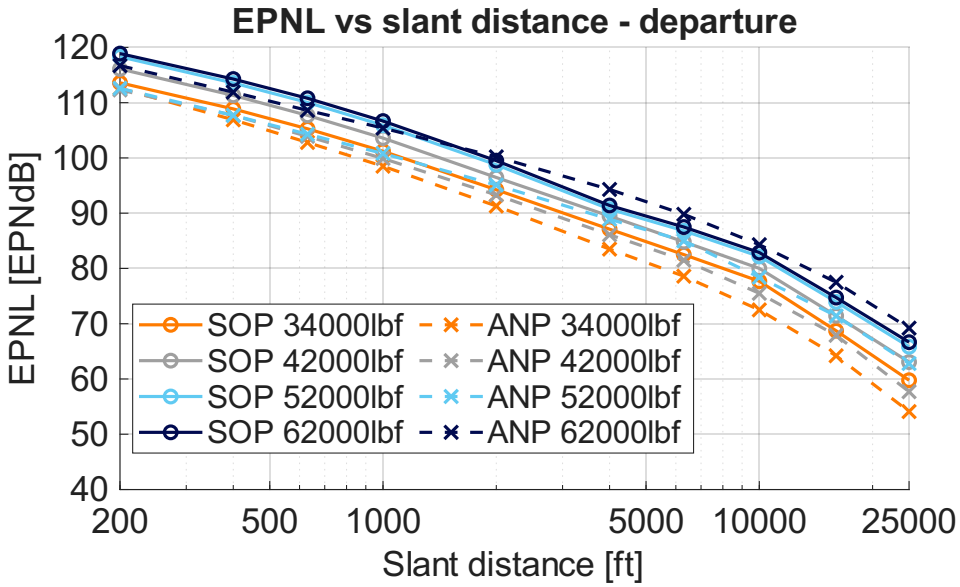

Figure C.15: NPD EPNL results for a departing Airbus A330

C.3.2. Approach

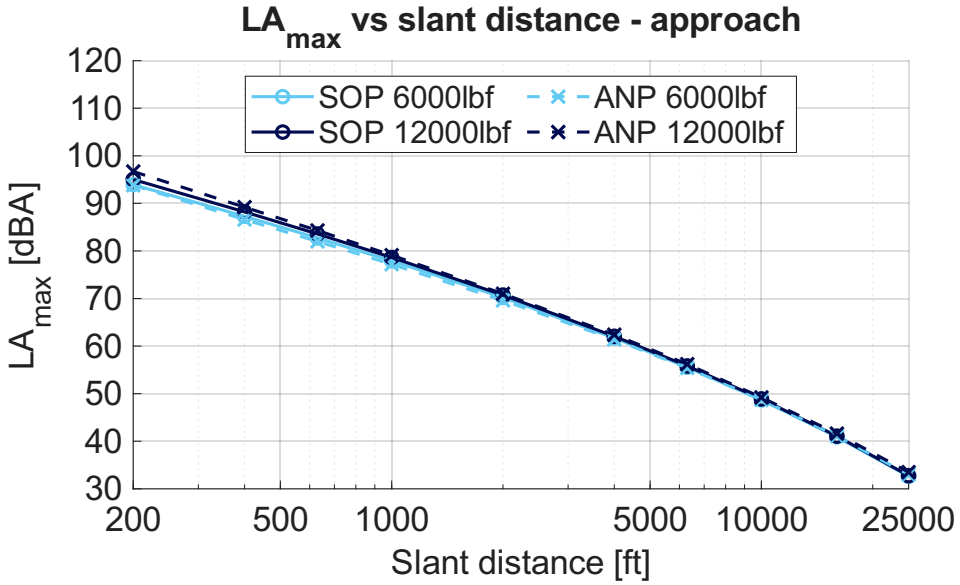

Figure C.16: NPD $L_{A_{max}}$ results for an approaching Airbus A330

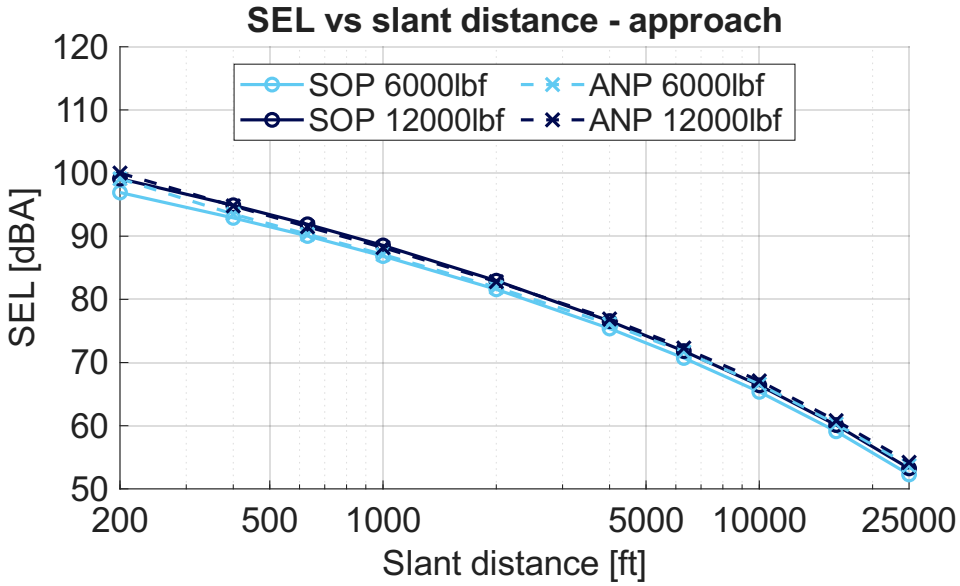

Figure C.17: NPD SEL results for an approaching Airbus A330

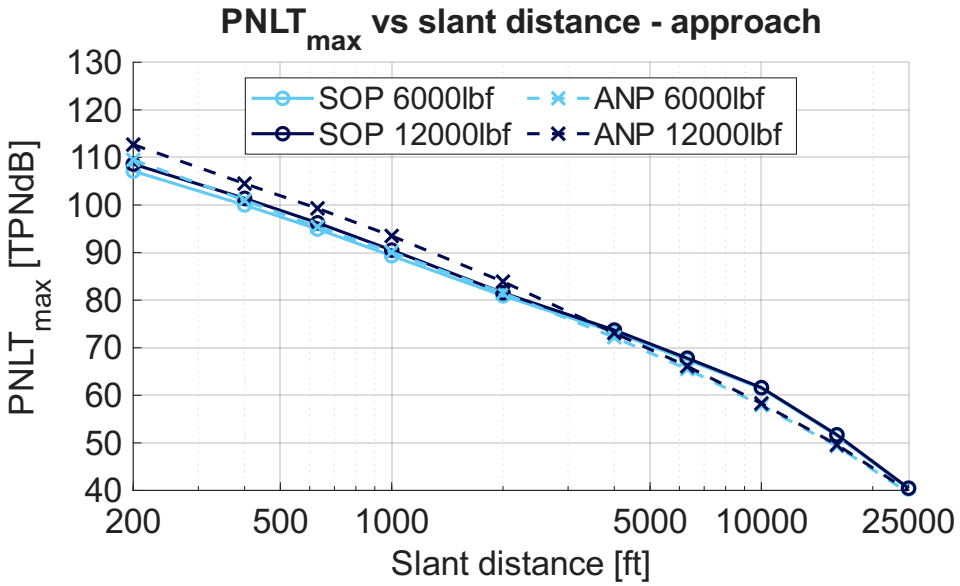

Figure C.18: NPD PNLT$_{max}$ results for an approaching Airbus A330

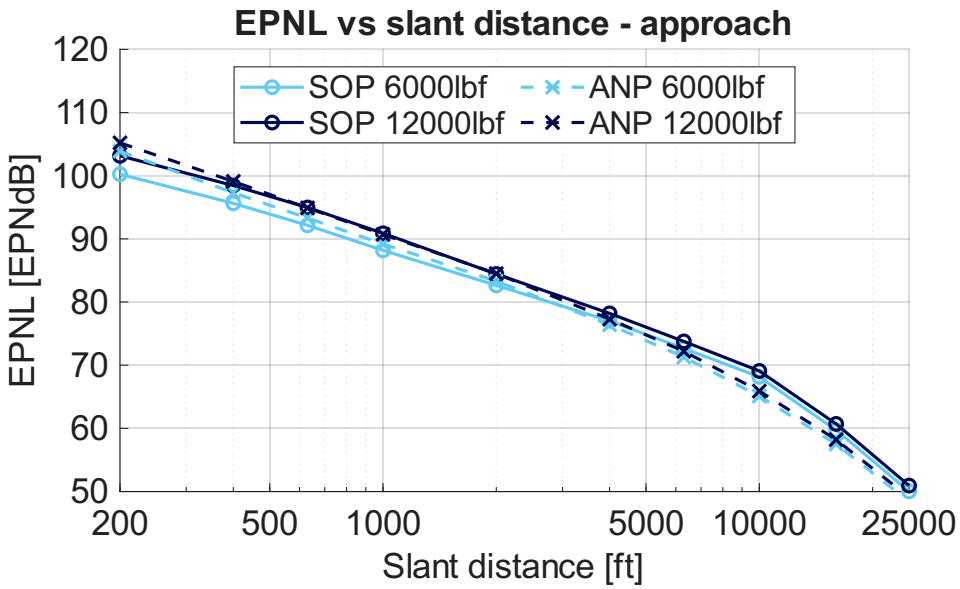

Figure C.19: NPD EPNL results for an approaching Airbus A330

D. Flyovers

D.1. Airbus A320

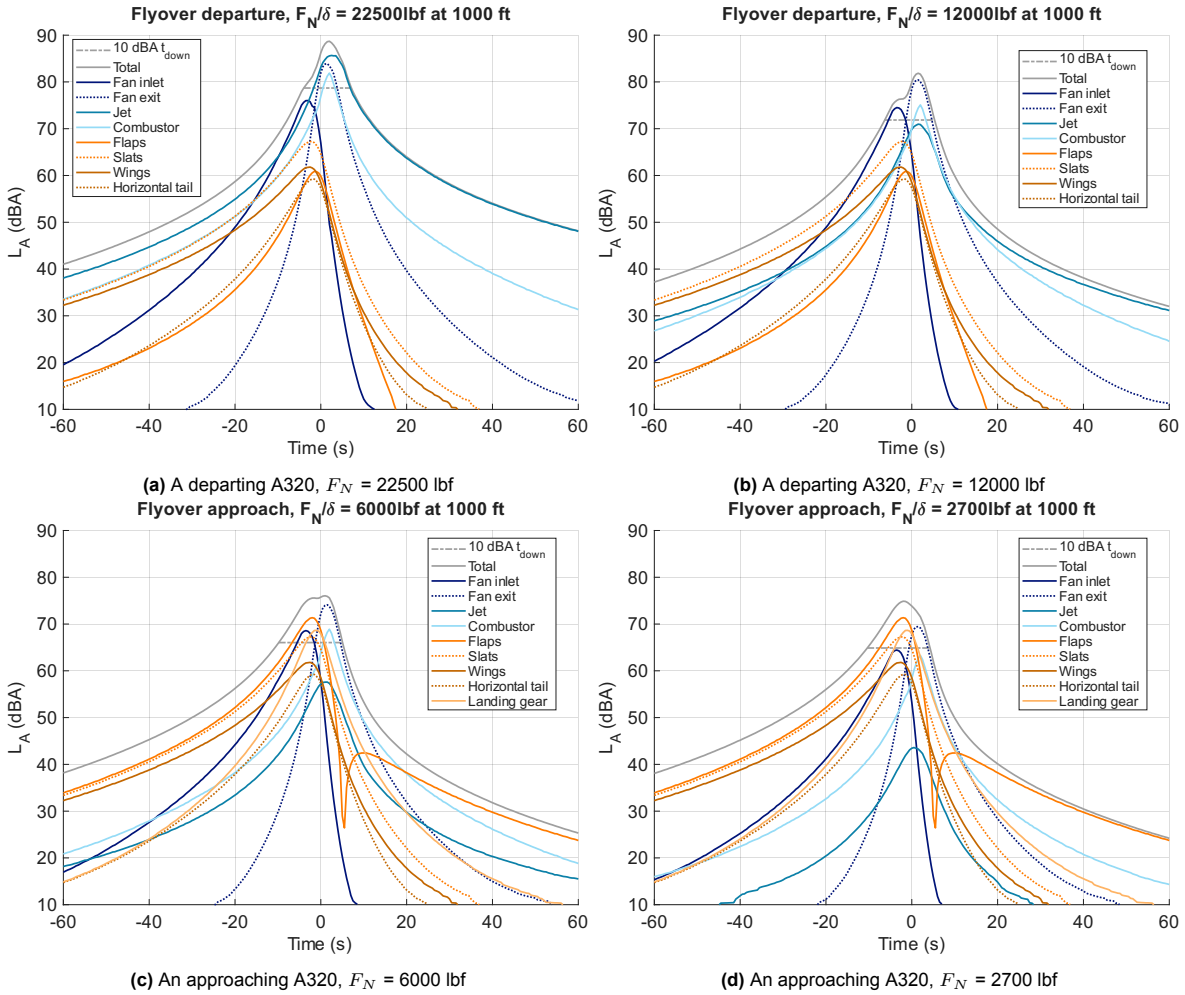

(a) A departing A320, F_N = 22500 lbf

(b) A departing A320, F_N = 12000 lbf

(c) An approaching A320, F_N = 6000 lbf

(d) An approaching A320, F_N = 2700 lbf

Figure D.1: A320 flyovers calculated at 1000 ft altitude with SOPRANO

D.2. Boeing 777

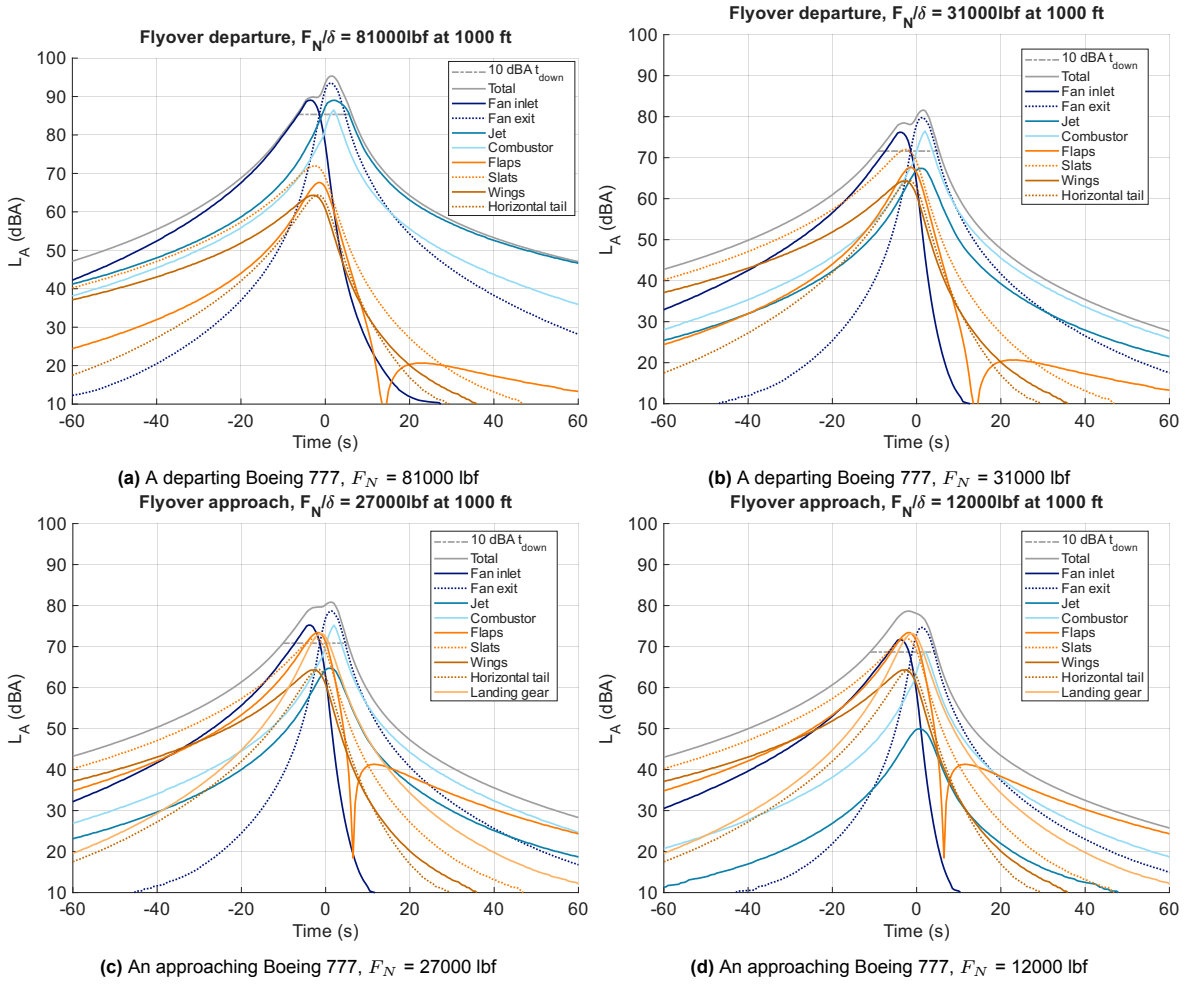

(a) A departing Boeing 777, F_N = 81000 lbf

(b) A departing Boeing 777, F_N = 31000 lbf

(c) An approaching Boeing 777, F_N = 27000 lbf

(d) An approaching Boeing 777, F_N = 12000 lbf

Figure D.2: Boeing 777 flyovers calculated at 1000 ft altitude with SOPRANO

D.3. Airbus A330

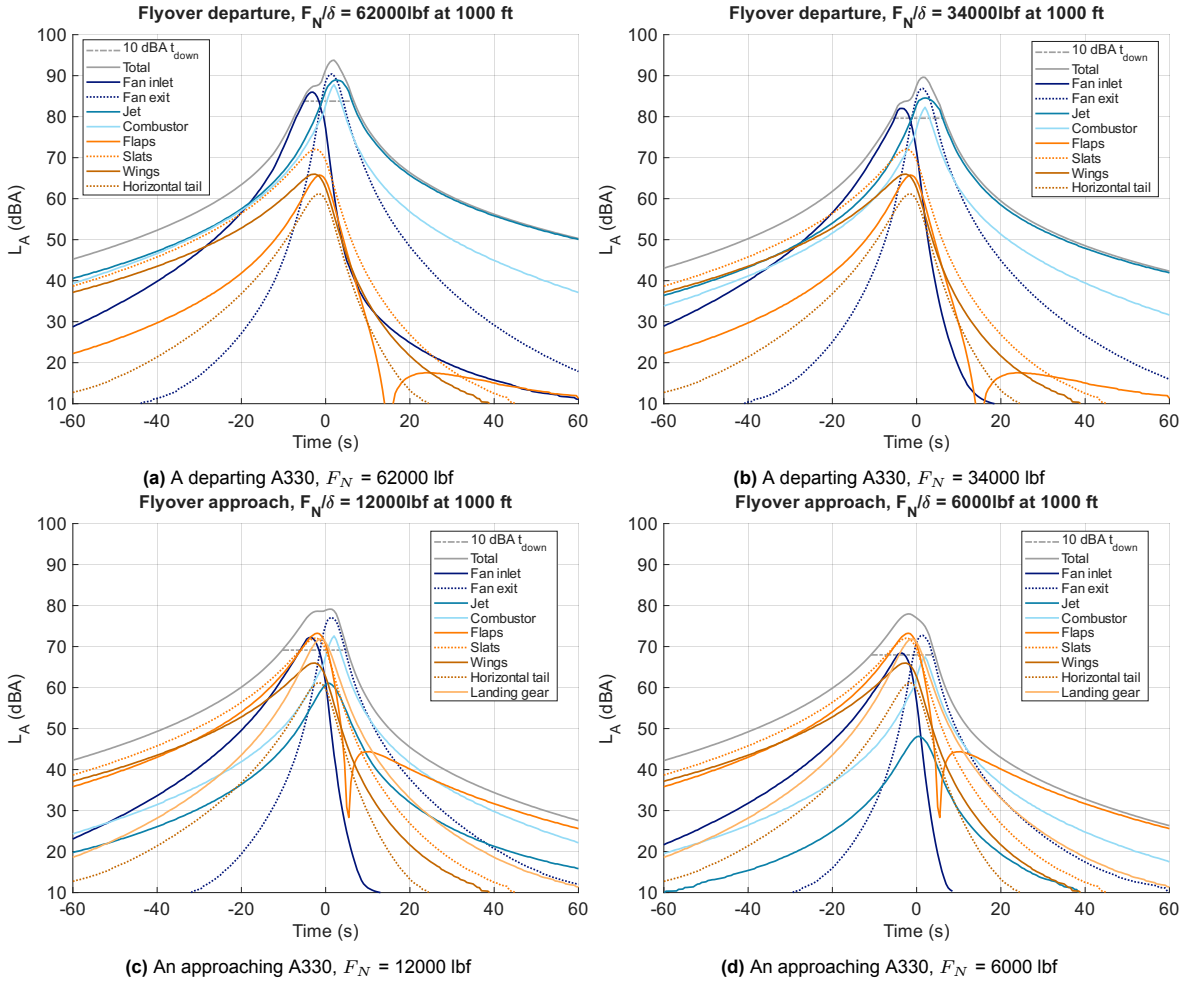

(a) A departing A330, F_N = 62000 lbf

(b) A departing A330, F_N = 34000 lbf

(c) An approaching A330, F_N = 12000 lbf

(d) An approaching A330, F_N = 6000 lbf

Figure D.3: A330 flyovers calculated at 1000 ft altitude with SOPRANO

D.4. REBEL-C

D.4.1. Departure

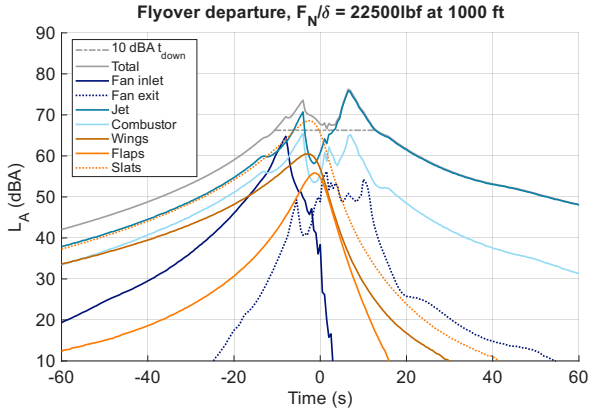

(a) A departing REBEL-C, F_N = 22500 lbf

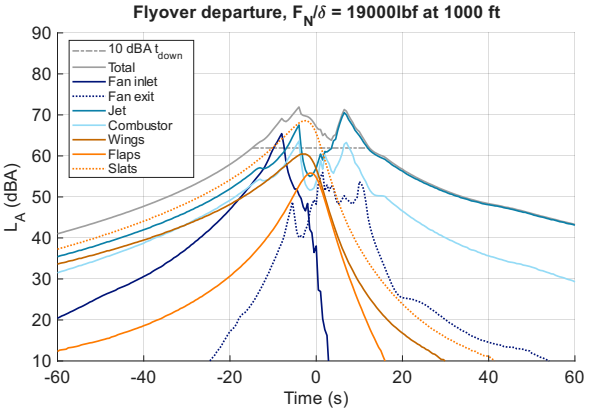

(b) A departing REBEL-C, F_N = 19000 lbf

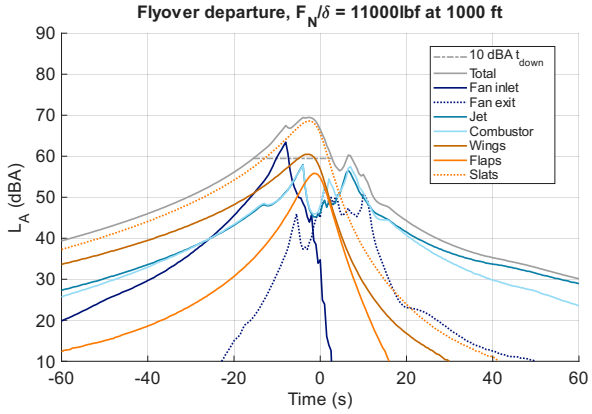

(c) A departing REBEL-C, F_N = 11000 lbf

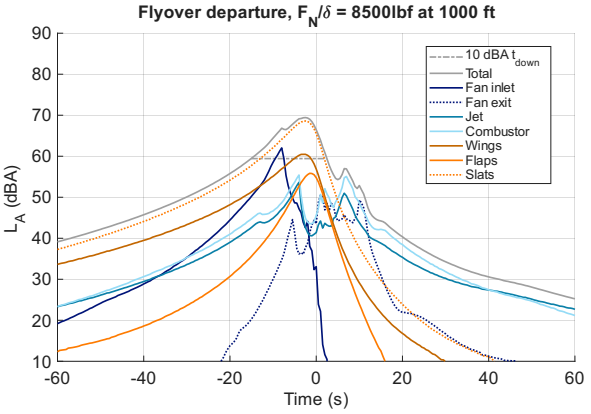

(d) A departing REBEL-C, F_N = 8500 lbf

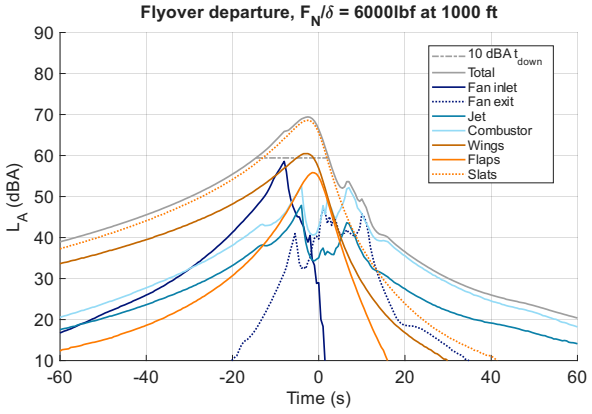

(e) A departing REBEL-C, F_N = 6000 lbf

Figure D.4: Departing REBEL-C flyovers calculated at 1000 ft altitude with SOPRANO

D.4.2. Approach

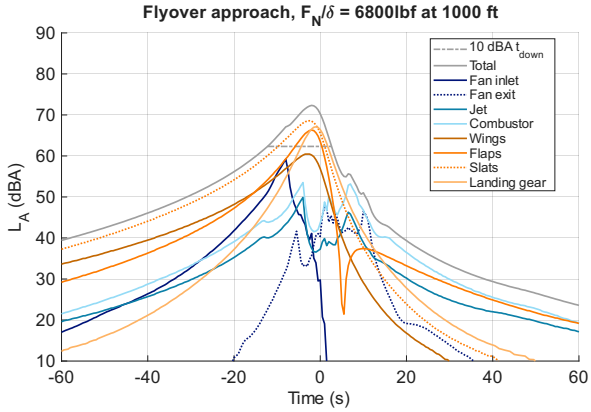

(a) An approaching REBEL-C, F_N = 6800 lbf

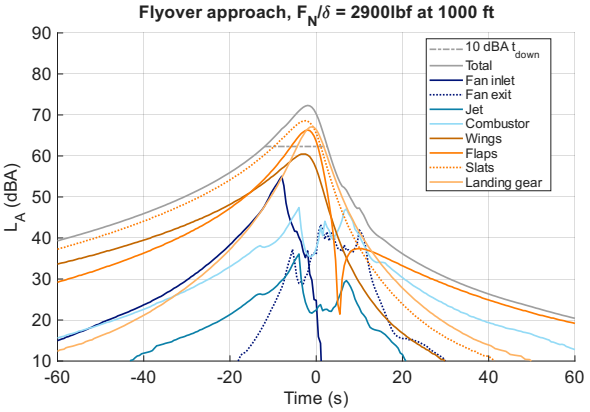

(b) An approaching REBEL-C, F_N = 2900 lbf

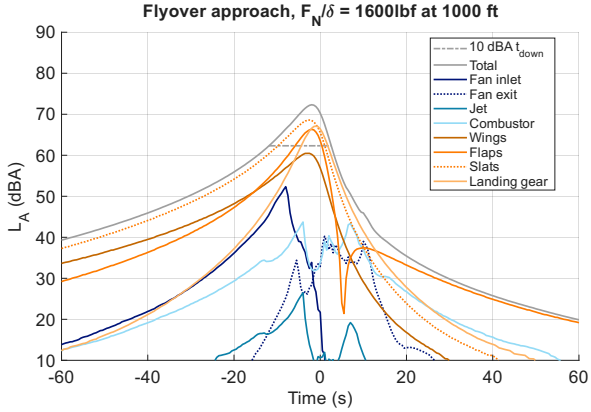

(c) An approaching REBEL-C, F_N = 1600 lbf

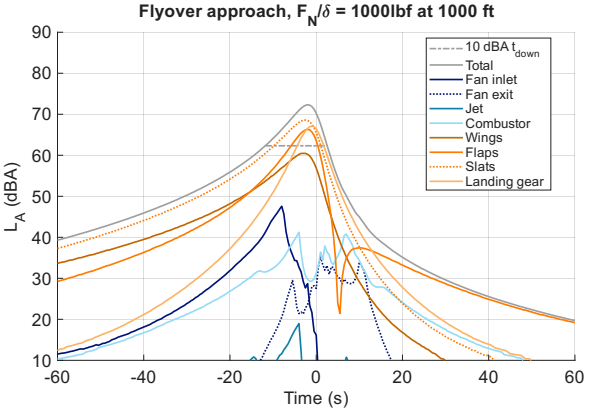

(d) An approaching REBEL-C, F_N = 1000 lbf

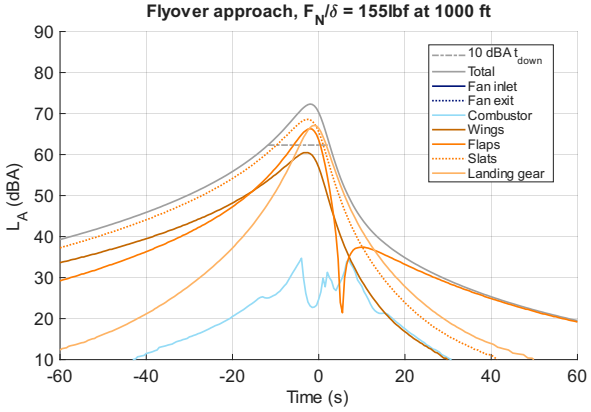

(e) An approaching REBEL-C, F_N = 155 lbf

Figure D.5: Approaching REBEL-C flyovers calculated at 1000 ft altitude with SOPRANO

D.4.3. Sensitivity Analysis

Flap sizing

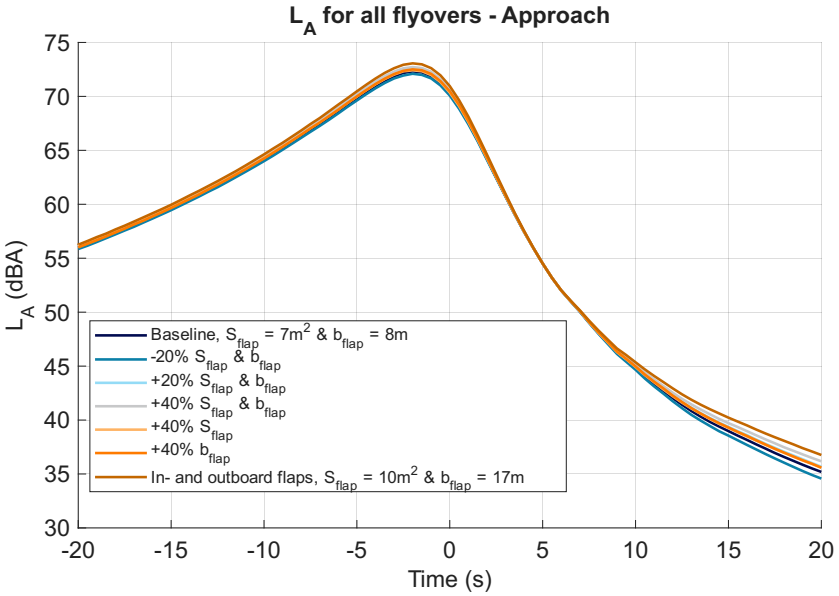

Figure D.6: Flyover results for variation in flap surface area and span for F_N/δ = 1000 lbf

Flap deflection angle

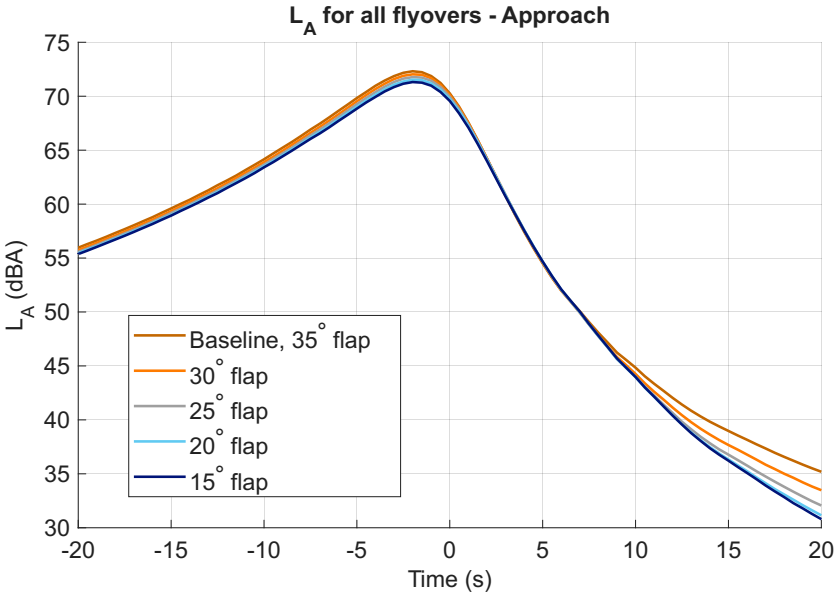

Figure D.7: Flyover results for variation on flap deflection angle for F_N/δ = 1000 lbf

Landing gear sizing

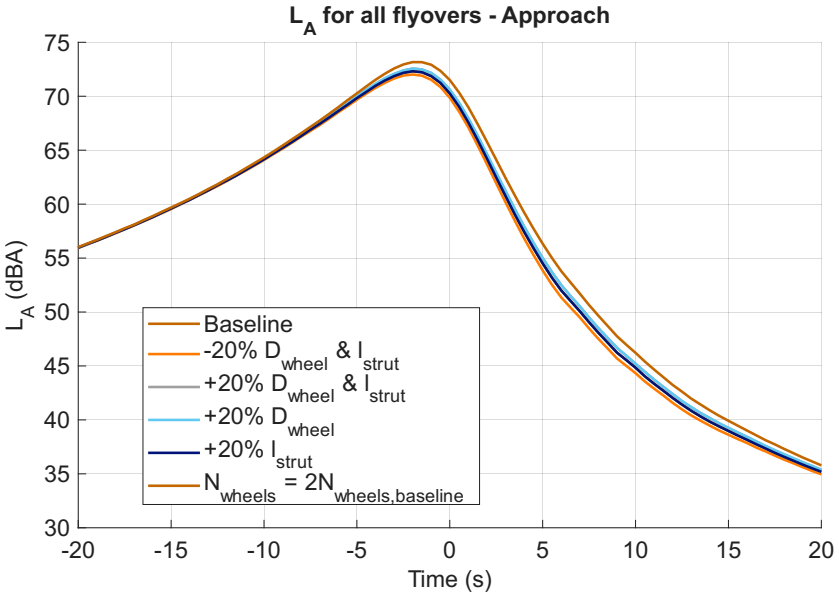

Figure D.8: Flyover results for variation in landing gear size for F_N/δ = 1000 lbf

Slat type

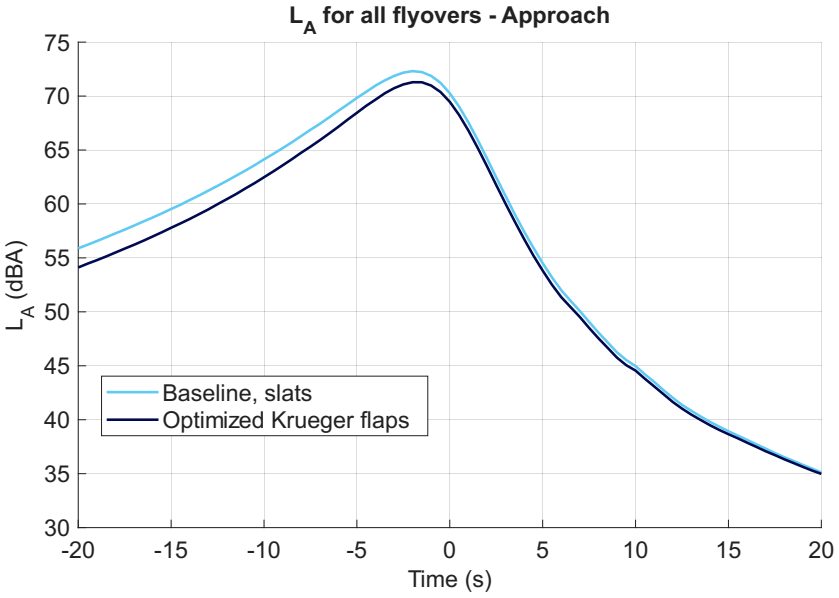

Figure D.9: Flyover results using an optimized Krueger flap instead of a slat for F_N/δ = 1000 lbf

Noise shielding

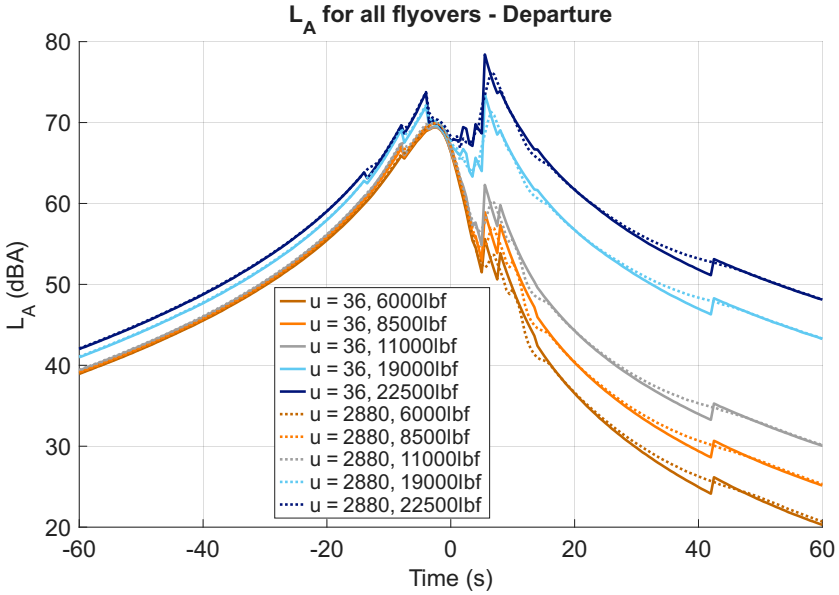

Figure D.10: OASPL of a flyover at 1000 ft for a coarse shielding grid with 10° steps between each polar angle and a fine shielding grid with 0.0625° steps

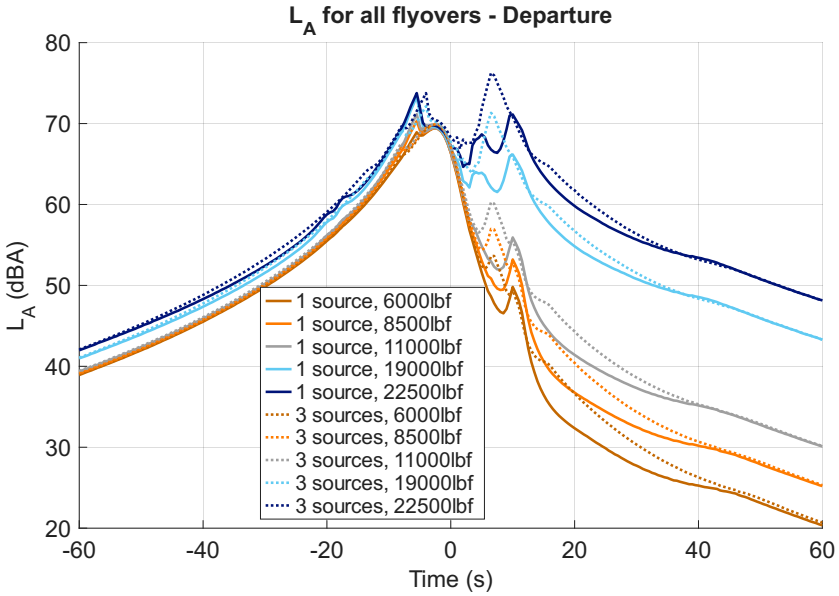

Figure D.11: OASPL of a flyover at 1000 ft using only one source location (fan exit) to compute all the shielding and using all three

E. Noise-Power-Distance Tables REBEL-C

E.1. Departure

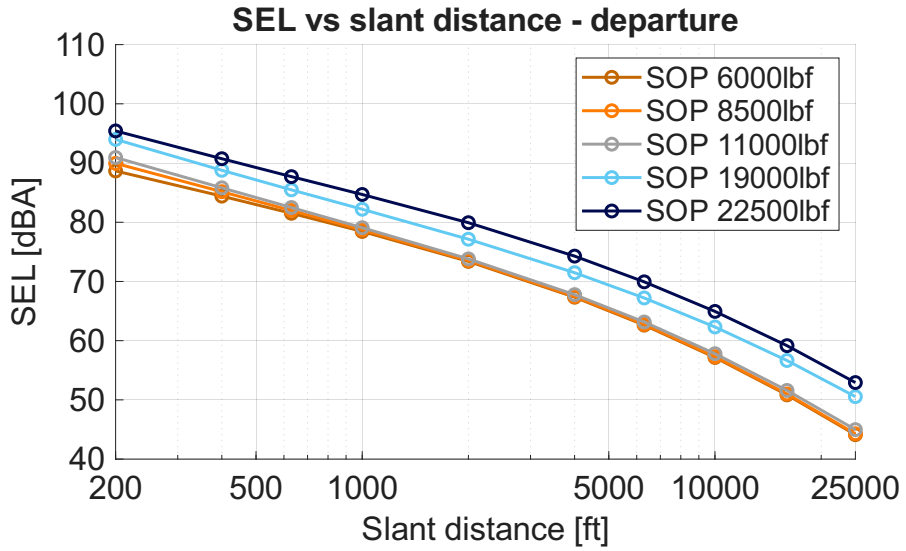

Figure E.1: SEL for the BWB during departure

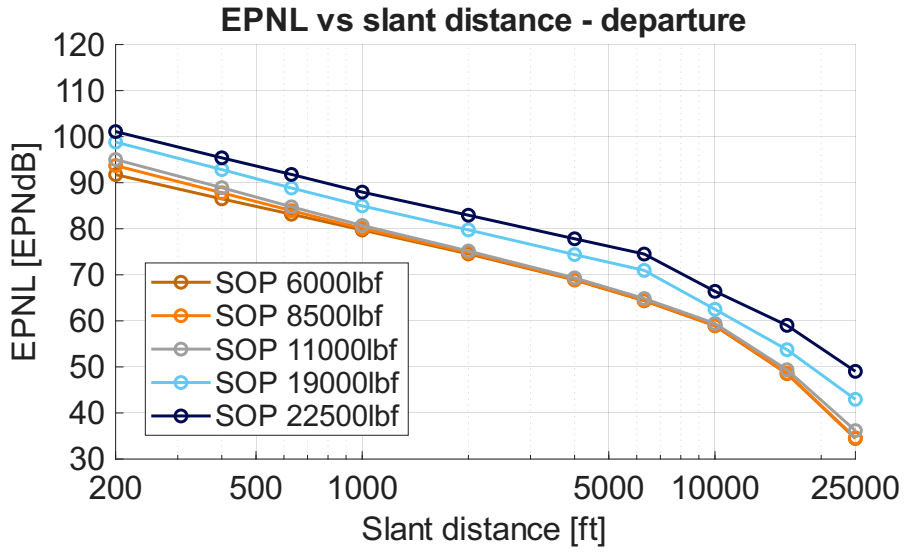

Figure E.2: EPNL for the BWB during departure

Table E.1: NPD table for the REBEL-C during departure

F_N/δ [lbf]	Noise metric	200 ft	400 ft	630 ft	1000 ft	2000 ft	4000 ft	6300 ft	10,000 ft	16,000 ft	25,000 ft
6000	$L_{A_{max}}$ [dBA]	85.0	78.5	74.1	69.4	61.9	53.5	47.3	40.3	32.4	24.3
6000	SEL [dBA]	88.7	84.4	81.5	78.4	73.4	67.3	62.6	57.2	50.8	44.1
6000	$PNLT_{max}$ [TPNdB]	97.1	90.2	85.4	80.4	72.1	64.8	58.8	51.8	39.9	24.4
6000	EPNL [EPNdB]	91.8	86.5	83.2	79.7	74.6	68.9	64.4	58.9	48.5	34.5
8500	$L_{A_{max}}$ [dBA]	85.0	78.5	74.1	69.4	61.9	53.5	47.3	40.3	32.5	24.3
8500	SEL [dBA]	89.9	85.2	82.0	78.7	73.5	67.5	62.8	57.3	51.0	44.3
8500	$PNLT_{max}$ [TPNdB]	97.2	90.3	85.5	80.4	73.2	64.8	58.9	51.9	40.0	24.5
8500	EPNL [EPNdB]	93.7	87.8	83.9	80.1	74.8	69.0	64.5	59.0	48.6	34.6
11000	$L_{A_{max}}$ [dBA]	84.9	78.4	74.0	69.3	61.9	53.5	47.4	40.6	32.9	24.8
11000	SEL [dBA]	90.9	85.8	82.5	79.1	73.8	67.8	63.2	57.8	51.6	45.0
11000	$PNLT_{max}$ [TPNdB]	97.1	90.2	85.4	80.4	73.2	64.9	58.9	52.0	40.4	25.8
11000	EPNL [EPNdB]	95.0	88.9	84.8	80.7	75.2	69.3	64.9	59.4	49.4	36.2
19000	$L_{A_{max}}$ [dBA]	86.7	80.2	75.9	71.3	64.1	56.2	50.4	44.0	36.8	29.3
19000	SEL [dBA]	94.0	88.8	85.5	82.2	77.1	71.5	67.2	62.3	56.6	50.5
19000	$PNLT_{max}$ [TPNdB]	101.6	94.8	91.1	86.3	78.5	70.8	65.9	56.0	45.7	33.4
19000	EPNL [EPNdB]	98.8	92.9	88.9	85.0	79.8	74.4	71.0	62.5	53.7	43.0
22500	$L_{A_{max}}$ [dBA]	91.5	85.1	80.8	76.2	69.0	61.0	55.2	48.7	41.4	33.7
22500	SEL [dBA]	95.4	90.7	87.7	84.7	79.9	74.3	69.9	64.9	59.2	52.9
22500	$PNLT_{max}$ [TPNdB]	105.9	99.2	94.7	91.0	82.8	76.1	71.3	61.7	52.8	41.3
22500	EPNL [EPNdB]	101.1	95.4	91.8	88.0	82.9	77.8	74.5	66.4	59.0	49.0

E.2. Approach

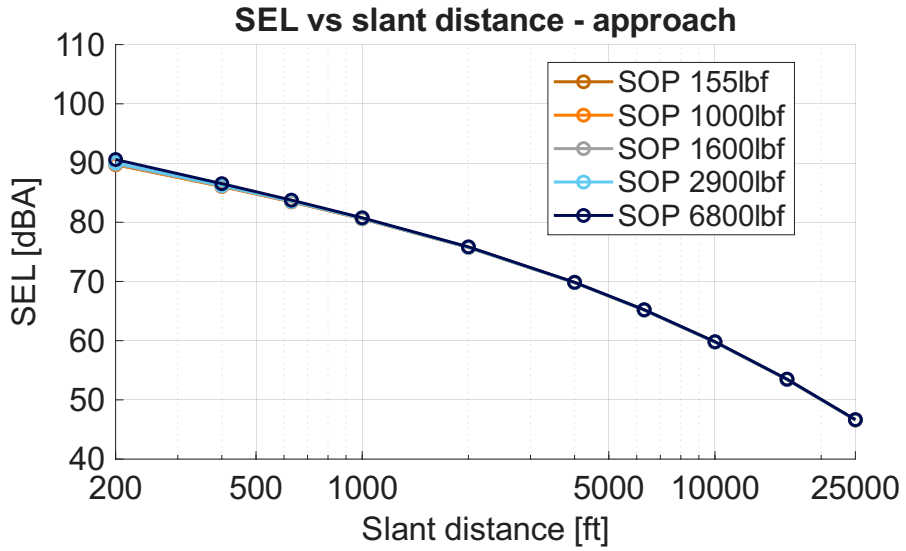

Figure E.3: SEL for the BWB during approach

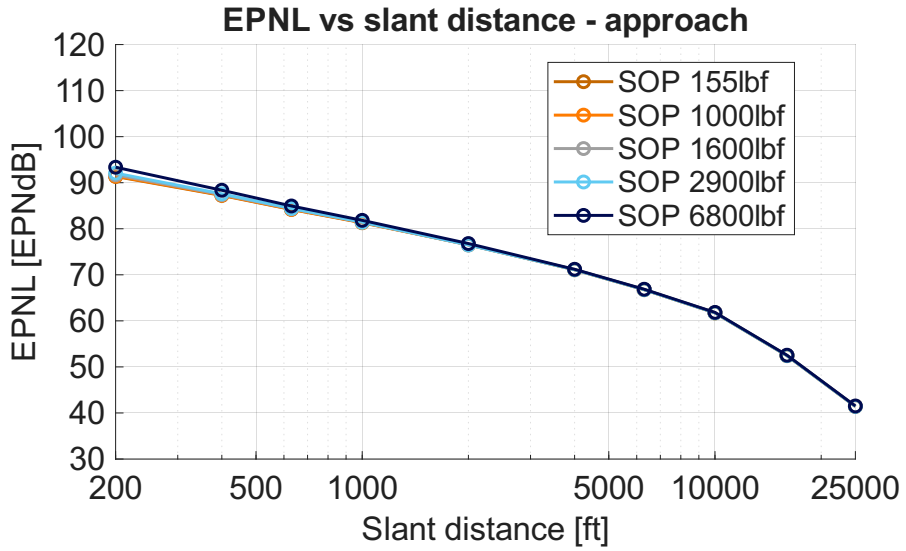

Figure E.4: EPNL for the BWB during approach

Table E.2: NPD table for the REBEL-C during approach

F_N/δ [lbf]	Noise metric	200 ft	400 ft	630 ft	1000 ft	2000 ft	4000 ft	6300 ft	10,000 ft	16,000 ft	25,000 ft
155	$L_{A_{max}}$ [dBA]	87.8	81.3	76.9	72.3	64.8	56.5	50.3	43.4	35.6	27.3
155	SEL [dBA]	89.7	86.0	83.4	80.6	75.7	69.8	65.2	59.8	53.4	46.6
155	$PNLT_{max}$ [TPNdB]	99.5	92.7	87.6	83.1	75.0	67.6	61.8	55.3	44.4	32.0
155	EPNL [EPNdB]	91.4	87.2	84.2	81.3	76.5	71.1	66.8	61.7	52.5	41.4
1000	$L_{A_{max}}$ [dBA]	87.8	81.3	76.9	72.3	64.8	56.5	50.3	43.4	35.6	27.3
1000	SEL [dBA]	89.8	86.1	83.5	80.6	75.7	69.8	65.2	59.8	53.4	46.6
1000	$PNLT_{max}$ [TPNdB]	99.5	92.7	87.6	83.1	75.0	67.6	61.8	55.3	44.4	32.0
1000	EPNL [EPNdB]	91.5	87.3	84.2	81.4	76.5	71.1	66.8	61.8	52.5	41.4
1600	$L_{A_{max}}$ [dBA]	87.8	81.3	76.9	72.3	64.8	56.5	50.3	43.4	35.6	27.3
1600	SEL [dBA]	89.8	86.1	83.5	80.6	75.8	69.8	65.2	59.8	53.5	46.6
1600	$PNLT_{max}$ [TPNdB]	99.5	92.7	87.6	83.1	75.0	67.6	61.8	55.3	44.4	32.0
1600	EPNL [EPNdB]	91.7	87.4	84.4	81.5	76.5	71.1	66.8	61.8	52.5	41.4
2900	$L_{A_{max}}$ [dBA]	87.8	81.3	76.9	72.3	64.8	56.5	50.3	43.4	35.6	27.3
2900	SEL [dBA]	90.0	86.2	83.5	80.7	75.8	69.8	65.2	59.8	53.5	46.6
2900	$PNLT_{max}$ [TPNdB]	99.5	92.7	87.6	83.1	75.0	67.6	61.8	55.3	44.4	32.0
2900	EPNL [EPNdB]	92.1	87.6	84.4	81.4	76.5	71.1	66.8	61.7	52.4	41.4
6800	$L_{A_{max}}$ [dBA]	87.8	81.3	76.9	72.3	64.8	56.5	50.3	43.4	35.6	27.3
6800	SEL [dBA]	90.6	86.5	83.7	80.8	75.8	69.9	65.2	59.8	53.5	46.7
6800	$PNLT_{max}$ [TPNdB]	99.5	92.7	87.6	83.1	75.0	67.6	61.8	55.3	44.4	32.0
6800	EPNL [EPNdB]	93.4	88.4	84.9	81.8	76.8	71.2	66.9	61.8	52.5	41.5